

Atomic Scale Observation of Chemical and Electronic Properties of Metal Oxide Surfaces

Thèse n. 7052 2016
Présenté le 21 Juin 2016
à la Faculté des Sciences de Base
Laboratoire de Science à l'Échelle Nanométrique
Programme Doctoral en Physique
École Polytechnique Fédérale de Lausanne
pour l'obtention du grade de Docteur ès Sciences
par

Christian Alexander Stephan Dette



acceptée sur proposition du jury:

Prof Minh Quang Tran, président du jury

Prof Klaus Kern, directeur de thèse

Prof Harald Brune, rapporteur

Prof Ernst Meyer, rapporteur

Prof Feliciano Giustino, rapporteur

Lausanne, EPFL, 2016

Be the change that you wish to see in the world.

— Mahatma Gandhi

Acknowledgements

With this part, I would like to thank the many people over the last years that contributed to my work.

First of all, I am very grateful to my thesis advisor **Prof. Klaus Kern** who gave me the opportunity to work in his research group at the Max Planck Institute for Solid State Research in Stuttgart, Germany. Furthermore, I would like to thank him for the scientific support throughout the years that gave me the freedom to shape and realize my own ideas and plans.

I am especially thankful to my group leader and friend **Dr. Soon Jung Jung** who always supported me during this work. I strongly acknowledge her scientific direction and I appreciated our many engaging and fruitful discussions. Thank you for this good time.

I am thankful to **Prof. Minh Quang Tran**, **Prof. Harald Brune**, **Prof. Feliciano Giustino**, and **Prof. Ernst Meyer** for being part of my thesis committee.

I would like to thank the people of the Gate-STM that participated over all these years to the success of our subgroup. Special thanks to **Dr. Sebastian Stepanow** who supervised me in my first year, gave me good scientific input and introduced me to the broad world of science. I am glad to have worked with **Dr. Christopher Kley** who introduced me to the system. I will never forget our late evening suitcase actions to transfer samples from the ESI to our STM together with my flat mate **Dr. Gordon Rinke**. I also want to thank **Paul Punke** and **Dr. Jan Cechal** for the friendly atmosphere at the Gate-STM. On a more recent note, I want to thank **Dr. Sara Barja**, **Shai Mangel**, and **Katharina Polyudov** for their great work. Schalom, Shai!

This work would not have been possible in this way without our great theory collaboration with the group of **Prof. Feliciano Giustino** who I have to mention once more. Together with his students **Dr. Christopher Patrick** and **Miguel Angel Perez-Osorio**, we always had great discussions that pushed the science further.

Acknowledgements

I also want to thank the non-scientific staff that helped me tremendously throughout the years so that I could focus on my research. I want to name **Wolfgang Stiepany**, **Peter Andler**, **Artur Küster**, **Marko Memmler**, the workshop led by **Thomas Frey**, our secretary **Sabine Birtel**, the IT-helpdesk led by **Andre Neubauer**, the security staff especially **Dimi**, and last but not least the canteen staff led by **Kati**.

Over the 4 years, it was crucial to have friends to rely on - personal as well as professional. With this, I want to express my gratitude towards my good friends **Claudius Morchutt**, **Dr. Carola Straßer**, **Dr. Eike Schäfer-Nolte**, **Dr. Ivan Pentegov**, and **Dr. Benjamin Wurster**.

I am blessed to have worked in a great atmosphere. For this I want to give a shoutout to the lunch table crew consisting of **Dr. Christoph Große**, **Diana Hötger**, **Sabine Abb**, **Dr. Rico Gutzler**, **Anna Roslawska**, **Elise Duquesne**, **Ahmed Faleh** and the rest of the amazing people at the Max Planck Institut that inspired, helped and motivated me over the years, namely **Dr. Berthold Jäck**, **Dr. Tobias Herden**, **Dr. Verena Schendel**, **Dr. Matthias Eltschka**, **Lukas Schlipf**, **Matthias Muenks**, **Dr. Stephan Rauschenbach**, **Dr. Markus Ternes**, **Dr. Klaus Kuhnke**, **Dr. Pablo Merino**, **Dr. Maximilian Assig**, **Jacob Senkpiel**, **Stiven Forti**, **Alexander Stöhr**, and **Alexander Kölker**. Thank you all.

One a more personal note, I am immensely grateful to my parents **Dr. Heidrun Dette-Schaudt** and **Dr. Stephan Dette** as well as the rest of **my family** who always supported me. My last words, I want to direct to my partner **Carrie Brubaker**. Thank you for you!

Stuttgart, April 2016

Abstract

To meet the future global energy demand - an estimated additional 10 terawatts (TWs) per year in 2050 - a diversification of energy sources and fuels is needed. Solar energy represents a prominent alternative energy source whose applications range from photocatalytic water-splitting (PWS) to photovoltaics. PWS is used to produce hydrogen, an interesting candidate for future fuels, whereas photovoltaics harvest light to produce electricity. An important material for these solar-based applications is titanium dioxide (TiO_2), thanks to its stability, band alignment and abundance. TiO_2 is either used as a scaffold or to create photogenerated electrons and holes to perform catalytic reactions. However, the large bandgap of TiO_2 yields device efficiencies that are too low to be economically sound. To make TiO_2 -based devices competitive, the electronic and chemical properties of TiO_2 need to be clearly understood.

In this work, using scanning tunneling microscopy (STM) together with spectroscopy techniques (scanning tunneling spectroscopy (STS) and inelastic tunneling spectroscopy (IETS)), we study the electronic and structural properties of pristine TiO_2 anatase (101), the most technologically relevant polymorph of TiO_2 . In particular, STM-IETS was applied for the first time to obtain chemical identification of adsorbed species on the semiconducting TiO_2 surface. For each step, density functional theory (DFT)-based calculations were performed to support our findings.

As a prerequisite to study TiO_2 anatase (101), we investigated the pristine surface using high-resolution STM to determine the individual Ti and O atom positions, which have been ambiguous in the past. Moreover, we showed that the high reactivity of step edges along the [-111] direction stems from oxygen vacancies (VOs). As studied with STS, this non-stoichiometric step edge exhibits a bandgap reduced by 2 eV. Furthermore, a higher amount of adsorbates are present on this step edge, suggesting a higher chemical reactivity. Going one step further, we created a novel surface phase consisting of undercoordinated Ti atoms, increasing the amount of VOs over the whole surface phase. This so-called titanium-terminated surface phase only modifies the surface layer, leaving the rest of the anatase (101) crystal untouched. This new surface phase exerts the same behavior as the step edges, reducing bandgap and enhancing reactivity. On the other hand, by exposing the anatase surface to excess oxygen at elevated temperatures, we reduced the overall surface reactivity. This reduction was

Abstract

achieved by formation of an oxygen network, acting as a passivating layer on top of the TiO₂ anatase (101) surface. The network shows no additional features in the electronic structure and does not influence the characteristically large bandgap of the bulk material. Additionally, the excess oxygen fills vacant positions at the highly-reactive step edges along the [-111] direction, reducing the overall surface reactivity even further. It is important to note that the preparation procedures of both surface phases with enhanced and reduced surface reactivity are cheap and reversible, only modifying standard ultra-high vacuum (UHV) cleaning methods without any additional materials.

Improved characterisation of the interaction between water and the TiO₂ anatase (101) surface represents another important aspect of this work. Although PWS on TiO₂ has been used for over 40 years, fundamental insights of the reaction mechanisms are still missing. In this thesis work, we labeled individual H₂O and OH molecules on the semiconducting surface by detecting their vibrational modes with STM-IETS. Through clear identification of adsorbed species, we demonstrated that water can thermally dissociate on the TiO₂ anatase (101) substrate without an additional light source. Furthermore, for the first time, we could structurally identify formation of a well-ordered water monolayer on TiO₂ anatase (101).

The work presented here opens new paths towards fundamental understanding of surface reactions on metal oxides, especially water on TiO₂ anatase (101), to improve future solar energy conversion devices.

Key words: Scanning Tunneling Microscopy and Spectroscopy, Inelastic Tunneling Spectroscopy, TiO₂, Surface Engineering, Water Dissociation, Catalysis.

Zusammenfassung

Um den zukünftigen weltweiten Energiebedarf - zusätzliche 10 Terawatt pro Jahr in 2050 - zu decken, wird eine Diversifikation der Energiequellen und Treibstoffen benötigt. Solare Energie ist eine interessante alternative Energiequelle, welche in vielen Bereichen benutzt wird: von photokatalytischer Wasserspaltung (PWS) um Wasserstoff, ein möglicher Kandidat für zukünftigen Treibstoff, zu produzieren hinzu Photovoltaik, welche Licht in Elektrizität umwandelt. Ein wichtiges Material für diese solarbasierenden Anwendungen ist aus Gründen der Stabilität, der Bandausrichtung und der Häufigkeit, Titandioxid (TiO_2). TiO_2 wird entweder benutzt um Photonen zu absorbieren, welche Elektronen und Löcher anregen um katalytische Reaktionen durchzuführen, oder als Gerüst. Jedoch haben Bauelemente basierend auf TiO_2 wegen der großen Bandlücke zu niedrige Effizienzen. Um dennoch Bauelemente aus TiO_2 wettbewerbsfähig zu gestalten, müssen die elektronischen und chemischen Eigenschaften von TiO_2 klar verstanden werden.

In dieser Arbeit, durch die Benutzung von Rastertunnelelektronenmikroskopie (STM) im Verbund mit Spektroskopietechniken (elastische und inelastische Tunnelspektroskopie (STS und IETS)) können wir die elektronischen und strukturellen Eigenschaften von reinem TiO_2 Anatas (101), dem wichtigsten technischen Polymorph, erhalten. Insbesondere die Ausführung von STM-IETS ermöglicht zum ersten Mal die chemische Identifikation von adsorbierten Molekülen auf dem TiO_2 Halbleiter. Für jeden Schritt wurden Modelle basierend auf der Dichtefunktionaltheorie (DFT) erstellt, welche unsere Resultate unterstützen.

Als Voraussetzung um TiO_2 Anatas (101) zu studieren, eruierten wir die reine Oberfläche mit Hilfe von hochauflösendem STM um die individuellen Positionen der Titan- und Sauerstoffatome zu bestimmen, was in der Vergangenheit unklar war. Darüberhinaus konnten wir zeigen, dass die hohe Reaktivität der Stufenkanten in der [-111] Richtung von Sauerstofffehlstellen (VOs) stammt. Diese nicht stöchiometrischen Stufenkanten zeigen eine um 2 eV reduzierte Bandlücke und eine größere Häufigkeit an Adsorbaten was auf eine höhere chemische Reaktivität hindeutet. Dies einen Schritt weiter gedacht, erschaffen wir eine neue Oberflächenphase, welche aus unterkoordinierten Titanatomen besteht, die die Anzahl an VOs über die ganze Oberflächenphase spannt. Diese sogenannte titanterminierte Oberflächenphase modifiziert lediglich

Abstract

die Oberfläche während der Rest des Anataskristalls unberührt bleibt. Die neue Phase verhält sich ähnlich zu den Stufenkanten, da sie auch eine reduzierte Bandlücke und erhöhte Reaktivität aufweist. Andererseits durch das Aussetzen des Kristalls an eine gesättigte Sauerstoffatmosphäre bei erhöhter Temperatur konnte auf der Anatasoberfläche eine Passivierungsschicht durch die Entstehung eines Sauerstoffnetzwerkes erschaffen werden. Dieses Netzwerk besitzt keine zusätzlichen Zustände in der elektronische Struktur und besitzt deswegen die gleiche große Bandlücke. Hinzukommend füllen die zusätzlichen Sauerstoffe die Fehlstellen an den hochreaktiven Stufenkanten entlang der [-111] Richtung auf, was wiederum die gesamte Oberflächenreaktivität verringert. Dabei sind die Preparationsmethoden der beiden Oberflächenphasen mit erhöhter und verringerter Reaktivität günstig und reversibel, da nur herkömmliche ultrahochvakuum (UHV) Reinigungsmethoden ohne zusätzliche Materialien benutzt wurden.

Ein weiterer wichtiger Aspekt dieser Arbeit ist das verbesserte Verständnis der Wechselwirkung zwischen Wasser und der TiO_2 (101) Anatasoberfläche. Obwohl PWS auf TiO_2 seit mehr als 40 Jahren benutzt wird, fehlen weiterhin fundamentale Erkenntnisse über den Reaktionsmechanismus. In dieser Arbeit benutzen wir STM-IETS um individuelle H_2O und OH Moleküle auf der Halbleiteroberfläche durch die Feststellung ihrer Vibrationsmoden zu markieren. Durch diese eindeutige Identifizierung der adsorbierten Moleküle können wir zeigen, dass Wasser thermisch auf TiO_2 Anatas (101) ohne den Einfluss von Licht dissoziieren kann. Darüberhinaus konnten wir zum ersten Mal strukturell und chemisch die Formung einer gut geordneten Wassermonolage, welche nur aus H_2O Molekülen besteht, auf der Anatasoberfläche identifizieren. Die Arbeit hier präsentiert neue Wege für ein besseres fundamentales Verständnis von Oberflächenreaktionen auf Metalloxiden, insbesondere für Wasser auf TiO_2 Anatas (101), welche möglicherweise zukünftige auf Solarenergie-basierende Bauelemente verbessern kann.

Stichwörter: Rastertunnelelektronenmikroskopie und -spektroskopie, Inelastische Tunnelspektroskopie, TiO_2 , Oberflächenmodifizierung, Wasserspaltung, Katalyse.

Résumé

Pour répondre à une demande énergétique mondiale – anticipée à atteindre 10 térawatts (TWS) supplémentaires par an en 2050 - une diversification des sources d'énergie et de combustibles est nécessaire. L'énergie solaire représente une importante source d'énergie alternative, dont les applications impliquent la décomposition photocatalytique de l'eau et la photovoltaïque. La décomposition photocatalytique de l'eau est une méthode de production d'hydrogène, un candidat intéressant de futurs combustibles, alors que les appareils photovoltaïques produisent de l'électricité en récoltant la lumière. Une substance de valeur pour ces applications solaires est titanium dioxide (TiO_2), grâce à sa stabilité, à l'alignement de la bande, et à son abondance. TiO_2 est utilisée soit comme échafaudage, soit pour créer des électrons et des trous photogénérés, afin d'effectuer des réactions catalytiques. Cependant, la grande largeur de bande interdite de TiO_2 mène aux efficacités d'appareil trop faibles pour une viabilité économique. Une compréhension optimisée des propriétés électroniques et chimiques de TiO_2 rendra concurrentiels les appareils fabriqués à la base de cette substance. En utilisant un microscope à effet tunnel (STM) ainsi que des techniques de spectroscopie [la spectroscopie à effet tunnel (STS) et la spectroscopie inélastique à effet tunnel (IETS)], nous avons étudié les caractéristiques électroniques et structurales des échantillons de TiO_2 anatase (101) dites « vierges » ; ce polymorphe est considéré le plus pertinent aux applications technologiques. En particulier, et pour la première fois, nous avons utilisé STM-IETS pour l'identification chimique des espèces adsorbées à la surface du semi-conducteur TiO_2 . À chaque étape, les calculs à la base de la théorie de la densité fonctionnelle (DFT) ont été effectués pour confirmer nos conclusions.

Comme condition préalable à l'étude de TiO_2 anatase (101), nous avons étudié sa surface vierge en utilisant STM à haute résolution pour identifier les positions individuelles des atomes de Ti et d'O, qui ont été ambiguës dans le passé. En surcroît, nous avons démontré que la réactivité de l'étape des bords le long de la direction [-111] provient des lacunes d'oxygène. Selon une étude STS, cette étape de bords non-stoichiométrique présente une bande interdite réduite par 2 eV. En outre, plus d'espèces adsorbées sont présentes sur cette étape des bords, ce qui suggère une réactivité chimique plus élevée. Allant plus loin, nous avons créé une nouvelle phase

Abstract

de surface constituée d'atomes de Ti sous-coordonnés, augmentant donc la quantité des lacunes d'oxygène sur toute la phase de surface. Cette phase de surface, terminée par titane, ne modifie que la couche de surface, laissant intact le reste du cristal de l'anatase (101). Cette nouvelle phase de surface exerce le même comportement que les bords de l'étape, réduisant la bande interdite et améliorant la réactivité. D'autre part, aux températures élevées, une exposition de la surface à un excès d'oxygène a réduit la réactivité globale dudit surface. Cette réduction résultait de la formation d'un réseau d'oxygène, agissant en tant que couche de passivation sur le dessus de la surface TiO₂ anatase (101). Le réseau ne présente pas de traits supplémentaires auprès de la structure électronique et n'influence point la grande largeur de bande interdite si caractéristique du matériau en vrac. En outre, l'excès d'oxygène remplit les positions vacantes au niveau des étapes des bords hautement réactives le long de la direction [-111], ce qui réduit encore plus la réactivité de surface. Il est important de noter que la préparation des deux phases de surface – avec une réactivité de surface soit améliorée, soit réduite – est abordable et réversible, ne modifiant que les méthodes de nettoyage standards de l'ultravide (UHV), et ceci sans matériel supplémentaire.

Une caractérisation améliorée de l'interaction de l'eau avec la surface de TiO₂ anatase (101) représente un autre concept clé de ce travail. Malgré l'application – depuis plus de quarante ans – de la décomposition photocatalytique médiée par TiO₂, notre compréhension fondamentale du mécanisme reste incomplète. Au cours de ce travail de thèse, sur la surface semi-conductrice, nous avons caractérisé H₂O et OH en tant que molécules individuelles en détectant leurs modes vibratoires par STM-IETS. Suite à une identification sans ambiguïté de ces espèces adsorbées, nous avons démontré que l'eau peut dissocier thermiquement sur un substrat composé de TiO₂ anatase (101), et ceci sans source de lumière supplémentaire. Pour la première fois, grâce à ses caractéristiques structurels et chimiques, nous avons identifié la formation d'une monocouche d'eau bien ordonnée sur la surface de TiO₂ anatase (101), qui ne se compose que de molécules d'eau (H₂O).

Ce œuvre ouvre de nouveaux chemins vers la compréhension fondamentale des réactions sur la surface des oxydes de métaux, en particulier la réaction de l'eau sur la surface de TiO₂ anatase (101), afin d'améliorer de futurs appareils visant la conversion de l'énergie solaire.

Merci à Carrie Brubaker pour ses contributions à la traduction de cet abstrait.

Mots clés : Microscopie et Spectroscopie à Effet Tunnel, TiO₂, Ingénierie de Surface, Dissociation de l'Eau, Catalyse.

Contents

Acknowledgements	i
Abstract (English/Deutsch/Français)	iii
List of figures	xii
1 Introduction	1
2 Scanning Tunneling Microscopy (STM) and Spectroscopy (STS)	7
2.1 Scanning Tunneling Microscopy	8
2.2 Inelastic Tunneling Spectroscopy	11
2.3 The Gate-STM	14
2.3.1 Precision Laboratory	14
2.3.2 The Instrument	15
2.3.3 Tip and Noble Metal Crystal Preparation	15
2.3.4 Integration of a Laser System	17
3 Titanium Dioxide (TiO₂)	19
3.1 Preparation of Oxygen-Terminated Anatase (101)	22
3.1.1 Characterization of the Anatase (101) surface with STM	23
3.1.2 Oxygen Vacancies	24
4 Engineering the Surface Properties of TiO₂ Anatase (101)	29
4.1 Oxygen Network	30
4.2 Titanium-Terminated Anatase (101)	35
4.2.1 Preparation of a New Surface Phase on TiO ₂ Anatase (101)	35
4.2.2 Theoretical Model of the Titanium-Terminated Surface Phase	39
4.3 Conclusion and Outlook	41
5 Water on TiO₂ Anatase (101)	43
5.1 IETS on CO on Cu(100)	43
5.1.1 Preparation	44
5.1.2 The Compressed Phase	45

Contents

5.2	Identifying Water Molecules and Hydroxyls via IETS	47
5.2.1	Preparation Method	47
5.2.2	H ₂ O and OH + H	48
5.2.3	D ₂ O and OD + D	51
5.2.4	Energy Shift of the Stretch Modes	52
5.2.5	STM Simulations and Dissociation Barriers for Water on TiO ₂ Anatase (101)	54
5.3	Globally Ordered Water Monolayer on TiO ₂ Anatase (101)	57
5.3.1	Preparation of Different Water Monolayers on TiO ₂ Anatase (101)	58
5.3.2	Water Monolayer	60
5.4	Conclusion	70
6	Conclusions and Perspectives	73
6.1	Conclusions	73
6.2	Perspectives	75
6.2.1	Further Understanding of the Water Interaction on TiO ₂	75
6.2.2	Investigating Photoinduced Effects using the Lasersystem	76
6.2.3	Different Metal Oxides, Different Reactions	78
	Bibliography	81
	Curriculum Vitae	95

List of Acronyms

ATR-FTIR attenuated total reflection Fourier transform infrared spectroscopy

CB conduction band

CBM conduction band minimum

CCD charged-coupled device

DFT density functional theory

DSSC dye-sensitized solar cell

DOS density of states

EELS electron energy loss spectroscopy

FT Fourier transform

GSTM Gate-STM

IETS inelastic tunneling spectroscopy

IGP ion getter pump

IRRAS infrared-reflection absorption spectroscopy

IR spectroscopy infrared spectroscopy

LDOS local density of states

LEED low energy electron diffraction

PDOS projected density of states

PES photoelectron spectroscopy

PWS photocatalytic water-splitting

SRM solar radiation management

Contents

STM scanning tunneling microscopy

STS scanning tunneling spectroscopy

TiO₂ titanium dioxide

TPD temperature programmed desorption

UHV ultra-high vacuum

UV ultraviolet

VB valence band

VBM valence band minimum

VO oxygen vacancy

WKB Wentzel-Kramers-Brillouin

XPS X-ray photoelectron spectroscopy

XRD X-ray diffraction

List of Figures

1.1	Principle of Photocatalytic Water-Splitting (PWS) and the Band Alignment of TiO ₂	2
2.1	Working Principle of the Scanning Tunneling Microscope	8
2.2	One-Dimensional Quantum Mechanical Tunnel Junction	9
2.3	Working Principle of STM-IETS	12
2.4	Precision Laboratory of the Max Planck Institute of Solid State Research	14
2.5	The Gate STM	16
2.6	New Sample Garage in the STM	16
2.7	New Flange and Optical Transmission of the New Window	18
3.1	Rutile and Anatase TiO ₂	21
3.2	Anatase TiO ₂ (101)	23
3.3	Step Edges of TiO ₂ Anatase (101)	26
4.1	Network and its Electronic Characterization on TiO ₂ Anatase (101). . .	30
4.2	Network Structure on TiO ₂ Anatase (101).	32
4.3	Functionalized Tip STM Image of the Network on TiO ₂ Anatase (101). .	33
4.4	Growth of a Network Patch on TiO ₂ Anatase (101).	34
4.5	Reversible Phase Transitions of TiO ₂ Anatase (101)	36
4.6	Distiguishing Both Surface Phases	37
4.7	Electronic structure of New Surface Phase	38
4.8	Theoretical Model of the Titanium-Terminated Surface Phase	40
5.1	Adsorption of CO on Cu(100)	44
5.2	The $c(7\sqrt{2} \times \sqrt{2})R45^\circ$ CO Superstructure on Cu(100)	46
5.3	Adsorbation of H ₂ O and OH + H on TiO ₂ Anatase (101).	49
5.4	STM-IETS of H ₂ O and OH+H on TiO ₂ Anatase (101)	50
5.5	ATR-FTIR of H ₂ O and OH+H on TiO ₂ Anatase (101)	51
5.6	STM-IETS of D ₂ O and OD+D	52
5.7	Energy Shift of the Stretch Modes of Water on TiO ₂ Anatase (101). . . .	53
5.8	DFT Atomistic Model of one of the Water Complexes on TiO ₂ Anatase(101). 54	

List of Figures

5.9	DFT-Based STM Simulated Images of Water on TiO ₂ Anatase(101). . . .	56
5.10	Dissociation Barriers for Water on TiO ₂ Anatase (101).	57
5.11	TPD and Temperature Dependent XPS Spectra of Water on TiO ₂ Anatase (101).	59
5.12	Ice Formation on TiO ₂ Anatase (101).	60
5.13	Formation of a Water Monolayer on TiO ₂ Anatase (101) Using Water Deposition.	61
5.14	Formation of a Water Monolayer on TiO ₂ Anatase (101) Using the STM Chamber.	62
5.15	Influence of High Electric Fields to the Water Monolayer.	63
5.16	Influence of Tip Pulses to the Water Monolayer.	64
5.17	Different Molecular Water Adsorptions on TiO ₂ Anatase (101).	66
5.18	Different Molecular Water Adsorptions on TiO ₂ Anatase (101) using a Functionalized Tip.	67
5.19	Determining the Structure of the Water Monolayer on TiO ₂ Anatase (101).	68
5.20	STM-IETS on the Water Monolayer on TiO ₂ Anatase (101).	69
5.21	Proposed Models of the Water Monolayer on TiO ₂ Anatase (101).	70
6.1	STM Image of Ice Clusters on the TiO ₂ Anatase (101) Surface.	75
6.2	Different Water Splitting Reactions Investigated by STM	78

1 Introduction

The increase in the global energy demand drives researchers to find new or more efficient energy sources and fuels every day. This is due to the fact that conventional energy sources like fossil fuels, which so far met this demand, will soon become increasingly expensive due to their limited availability. Looking back over the last century it becomes clear that the economic growth in the world was largely attributed to the low energy prices. In order to sustain the economic growth and lifestyle we will need to supply an additional 10 terawatts (TW) until 2050 [1] in an environmental clean and economical cheap way. Supplying this additional energy solely by combustion of fossil fuels would require a yearly storage of additional 25 billion metric tons of CO₂ (140 times the volume of lake Geneva!) to avoid further environmental impact. Already the emission of anthropogenic greenhouse gases from combustion of fossil fuels resulted in an increase of the global average surface temperature by 0.85 °C in the last 130 years causing melting of glaciers, rising sea levels and extreme weather events [2]. Using nuclear power as an alternative energy source would require to build a new 1 GW nuclear fission plant every day until 2050. Hence, this extra supply of energy can only be matched including sustainable energy sources. Of all sustainable energy sources, the sun with its 120.000 TW shining onto the earth surface sticks out to be the most promising one. However, the solar energy has to be converted either into electric energy (photovoltaics [3, 4]) or fuels (photocatalysis [5]) to be used in our society.

In conventional silicon-based photovoltaics sunlight is absorbed in the semiconductor generating electrons and holes. Due to an internal electric field (p-n-junction) the charge carriers are separated and can be used as an electric source. The challenges with silicon-based photovoltaics are the need of high quality Si leading to higher production and environmental costs as well as the relative low performances under diffuse (cloudy) light conditions. These aspects have been tackled by the invention of dye-sensitized solar cells in 1991 [4] in which dye molecules are adsorbed on top of a

Chapter 1. Introduction

titanium dioxide (TiO_2) scaffold in combination with an electrolyte. The sunlight is absorbed by the dye molecule and the excited electron is immediately injected into the conduction band (CB) of the TiO_2 . The electron performs a load and subsequently, the dye is regenerated by the electrolyte. In these cells the interaction of the molecules and the underlying TiO_2 substrate are central for the overall performance of the cells. This area of research has recently seen a lot of attention due to the finding of methylammonium lead halides perovskites substituting the dye molecule [6, 7, 8]. These new cells reach an efficiency of over 20% [9] making this technique industrial relevant with first commercially available modules being potentially released in 2017 [10]. Being the leading semiconductor catalyst, TiO_2 also plays an important role in solar energy conversion to fuels, such as hydrogen. Hydrogen presents an interesting alternative source of fuel since burning it with oxygen is emission free. To avoid the production of greenhouse gases photocatalytic water-splitting (PWS) is a promising candidate. In PWS cells, which were introduced more than 40 years ago, water molecules are adsorbed on a catalytic semiconductor [5] (Figure 1.1a). The absorbed sunlight is used to create electrons and holes in the semiconductor which subsequently split water into its components creating molecular hydrogen and oxygen. TiO_2 has proven to be the leading semiconducting catalyst for this reaction, due to its high abundance, stability and band alignment, but device efficiencies are too low to be economically sound. This results in high hydrogen production costs using TiO_2 -based devices of around $\$10 \text{ kg}^{-1} \text{ H}_2$ which are 10 times higher than for hydrogen production using steam refinement [11]. Hence, over 95% of the hydrogen production derives from steam refinement processes extracting hydrogen from fossil methane but releasing greenhouse gases during the process. Due to the low efficiencies of these devices more studies have to be directed towards PWS, such as understanding the role of photogenerated charge carriers in the TiO_2 substrate, to make hydrogen a clean and sound alternative to fossil fuels.

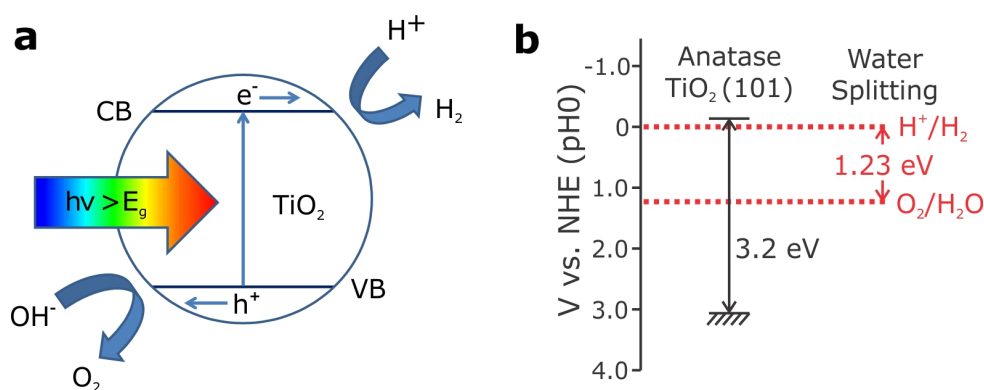


Figure 1.1: Principle of photocatalytic water-splitting (PWS, **a**) and the band alignment of TiO_2 (**b**).

As stated, in both solar conversion types - photovoltaics and -catalysis - the TiO_2 substrate has a strong influence on the device efficiency. Advancements require a better fundamental understanding of TiO_2 with its surface properties and interaction with different molecules. As an example, an examination of figure 1.1b underlines that for water splitting operations the TiO_2 anatase (101) band alignment requires further optimization. While the CB is well aligned with the hydrogen reduction, the holes created in the valence band (VB) after light absorption have a strong overpotential to perform the oxygen evolution reaction. Reducing the bandgap by shifting the VB closer to the Fermilevel is desired and a strong field of research.

In general, natural TiO_2 occurs in its thermodynamical most stable form rutile but to have a higher surface to volume ratio TiO_2 is usually used in devices as small nanoparticles which coalesce in the anatase (101) termination [12]. Due to the transition of anatase into rutile at elevated temperatures, crystals of sufficient size and quality to perform fundamental research have been scarce [13] and give an explanation of the missing understanding of the anatase surface.

In this thesis, we use scanning tunneling microscopy (STM) to investigate the fundamental properties of a natural grown TiO_2 anatase (101) crystal. The STM, which was invented by G. Binnig and H. Rohrer in 1982 allows the routinely imaging of individual atoms and molecules [14, 15, 16]. Furthermore, the STM also provides information about the electronic structure and can even give chemical resolution on the molecular scale. We will present the working principle of the STM in chapter 2.

One important attribute of the TiO_2 anatase (101) surface is its chemical reactivity. The reasons for this are manifold ranging from surface passivation to enhanced adsorption of molecules. To improve the adsorption of molecules and catalytic reactions, the chemical reactivity of TiO_2 anatase surface needs to be increased. This plays an important role in photocatalysis where a stronger adsorption and catalytic response directly leads to an increase in efficiency of the device. A prominent source for increasing the chemical reactivity for metal oxides are oxygen vacancies (VOs). The VOs change the oxidation of neighboring surface Ti atoms from Ti^{4+} to Ti^{3+} resulting in a filling up of the Ti3d bands. This additional reservoir of electrons can be used to enhance chemical reactivity. However, VOs have the tendency in TiO_2 anatase (101) to migrate from the surface to subsurface layers leaving the surface stoichiometric and non reactive. We will present in section 3.1.2 that these VOs are also apparent at the [-111] step edge explaining the high reactivity which results in more molecule being adsorbed on this step edge than elsewhere. By controlling the amount of step edges (e.g. creating vicinal surfaces), it is possible to increase the amount of catalytic active centers (VOs) on the TiO_2 anatase (101) surface and thus, increase the chemical reactivity. However, this method is limited by the fact that in nanoparticles atoms at step edges account for approximately 15% of the total amount of surface atoms

Chapter 1. Introduction

for a particle of 3 nm in diameter [17]. Using our findings and a modification of the standard UHV preparation method we successfully create in section 4.2 a new surface phase, the so-called titanium terminated surface phase, which extends the amount of VOs over the whole phase. Another important aspect of the filling up of the Ti3d bands caused by VOs is the reduction of the bandgap by filling up states in the VB adjusting it closer to the oxygen evolution potential. Hence, we can combine the two most desired attributes in photocatalysis, better band alignment and higher chemical reactivity, in a surface phase which only modifies the very surface leaving the bulk properties untouched.

On the other hand, surface passivation, the overall reduction of chemical reactivity of a surface, plays an important role in engineering and physical chemistry and is used to prevent surfaces from corrosion. Usually this is done with metal surfaces by growing a thin oxide layer on top. In the case of optical sensors based on thin film TiO₂ which are already on market, passivation could be used to maintain the optical properties of the film under ambient or even aqueous conditions. In section 4.1, we will present the growth of an oxygen network on top of the TiO₂ anatase surface significantly reducing chemical reactivity which is investigated by STM and spectroscopy techniques. We achieve this network growth by standard UHV preparation methods exposing the crystal to excessive oxygen. The findings open new ways to reduce reactivity of the TiO₂ anatase (101) surface.

To further enhance PWS a detailed understanding of the interaction between single water molecules and the TiO₂ anatase (101) substrate is crucial. A certain level of understanding has been achieved in the past using averaging techniques like X-ray photoelectron spectroscopy (XPS) or infrared spectroscopy (IR spectroscopy). These studies could show temperature dependences of water desorption and adsorption, the influence of oxygen vacancies on the dissociation process, and so on [18, 19, 20, 21]. However, the photo dissociation of a single water molecule on TiO₂ anatase (101) cannot be investigated by these techniques. This results in a lack of understanding of the water splitting process. For this, a direct imaging technique with chemical identification on the atomic scale is needed but has been unprecedented for molecules on semiconductors. Indeed, the chemical identification of the individual molecules is critical due to the variety of adsorbate species on the anatase surface. We will present in chapter 5 how the unique combination of the direct imaging technique STM with inelastic tunneling spectroscopy (IETS) can be used to chemically identify molecular and dissociated water on TiO₂ anatase (101). The idea behind this technique, which has been pioneered experimentally by W.Ho in the late 1990s [22, 23, 24], is the detection of molecular vibrations which can be used as fingerprints to identify different molecules. We will first use STM-IETS on the well studied CO on Cu(100) system to optimize our settings. Following, we will present how STM-IETS can be used to

identify the water bending and stretching modes of individual water molecules on the TiO₂ anatase surface. This opens a new path towards investigating light-induced water splitting on the molecular scale, since now it is possible to identify the reaction products, which first steps will be discussed in chapter 6.

Since water is ubiquitous in ambient atmosphere the water monolayer interaction with the TiO₂ surface has far reaching consequences in photoelectrochemical cells [25] and PWS. Hence, a lot of research has been dedicated to identify the adsorption state and structure of the water monolayer on the different TiO₂ polymorphs. However, on anatase (101), it is not yet clear if a water monolayer adsorbs molecularly or dissociated [26, 21, 20, 19]. We will present in section 5.3.2 our findings of a globally ordered water monolayer consisting purely out of molecular H₂O on the anatase (101) surface. The structure of the monolayer is investigated by STM in combination with IETS and DFT calculations. The results obtained in this section will be a step closer to understanding the water monolayer adsorption on anatase (101).

In summary, this thesis will introduce the technical background for the tools used throughout the thesis in chapter 2. After a general introduction of TiO₂ anatase (101) and the importance of VOs for the atomic structure of the terrace as well as step edges in chapter 3, we will discuss the engineering of surface properties of the anatase crystal in detail in chapter 4. The water adsorption on TiO₂ anatase (101) is subject in chapter 5. The thesis will conclude and give an outlook in chapter 6.

2 Scanning Tunneling Microscopy (STM) and Spectroscopy (STS)

The invention of the scanning tunneling microscopy (STM) by G. Binnig and H. Rohrer in 1982 revolutionized the field of nanotechnology due to its ability to routinely resolve individual atoms and molecules [14, 15, 16]. This pioneering work was awarded with the Nobel prize in 1986. Its versatility allowed scientists not only to resolve topographic features but also to manipulate single atoms and create unprecedented nanostructures, gain insights into electronic and magnetic properties, distinguish individual molecules due to their chemical fingerprint, and many more.

The working principle of the STM is shown in figure 2.1. It is based on the quantum mechanical tunneling effect which allows electrons to tunnel through a potential barrier which energy is higher than that of the electron [27]. If now a small negative bias voltage is applied to the sample, electrons can tunnel from filled states in the tip into empty states of the sample resulting in a small tunneling current in the range of 10^{-9} A. In order to detect these low currents a current amplifier is used. Since the tunneling current is exponentially dependent on the tip-sample distance (see equation 2.4) already small changes in the topography down to 10^{-12} m can be detected.

The STM has two different operation modes. In constant current, a feedback controller maintains the current by regulating the tip-sample distance through a piezoelectric transducer that is attached to the tip. The tip then scans over the surface and changes in the z-position of the tip are simultaneously recorded to produce topographic images. In constant height, the feedback loop is switched off and the tip is kept at a constant height while it scans the surface. Here, the origin for the contrast are the recorded changes in the tunneling current. This mode can only be used on flat surfaces, since strong variations in the surface height may result in tip crashes into the sample. In the following the theoretical background and the experimental system will be presented.

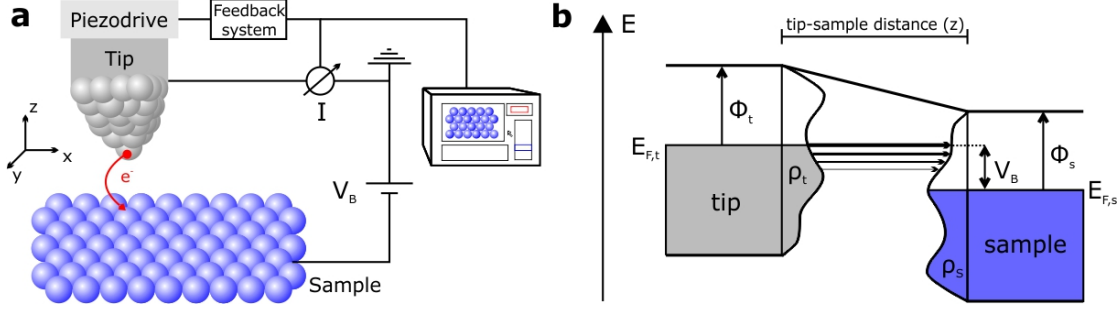


Figure 2.1: Working Principle of the STM. **a**, Schematic drawing of the STM setup with applied bias voltage V_B on the sample. The detected current or tip position can be used to display a topographic image of the sample. **b**, Energy diagram of the tunneling process in the STM. Electrons can tunnel e.g. from occupied tip states to unoccupied sample states when V_B is applied.

2.1 Scanning Tunneling Microscopy

Although the tunneling effect was already observed in 1897 by Robert Williams Wood when he was investigating field emission of electrons [28], it took another 30 years until G. Wentzel, H. A. Kramers and L. N. Brillouin set the base to describe this effect with their famous Wentzel-Kramers-Brillouin (WKB)-approximation [29, 30, 31].

As described before, the tunnel effect allows electrons to penetrate a barrier although the energy E of the electron is smaller than the potential barrier height U . Due to the particle-wave dualism the electron can be described as a wavefunction which has to fulfill the Schrödinger equation:

$$\partial_z^2 \psi(z) - \kappa^2(z) \psi(z) = 0 \quad (2.1)$$

with $\kappa(z) = \sqrt{\frac{2m}{\hbar^2}(U(z) - E)}$. Here, $\hbar = \frac{h}{2\pi}$ is the Planck constant, E and m the energy and mass of the electron and $U(z)$ is the potential barrier in z -direction (tip sample direction).

The solution to equation 2.1 can be split into three different regions. In the tip and the sample region, where $E > U$, the solution is:

$$\psi(z) = \psi(0) e^{\pm i k(z) z} \quad (2.2)$$

with $k(z) = \sqrt{\frac{2m}{\hbar^2}(E - U(z))}$. In the classically forbidden region in between tip and sample, i.e. inside the barrier, the solution is:

$$\psi(z) = \psi(0) e^{\pm \kappa z} \quad (2.3)$$

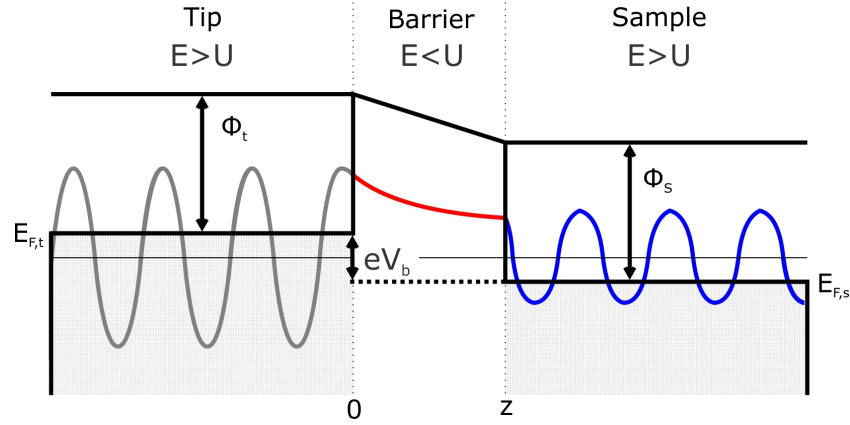


Figure 2.2: Schematic of a one-dimensional quantum mechanical tunnel junction. Due to the wave-particle dualism the tunneling electrons can be described as wavefunctions that need to fulfill the Schrödinger equation in the different areas.

This wavefunction describes an electron tunnelling through the barrier in the positive and negative z -direction. Due to the exponential, the wavefunction decays in the barrier but the probability density to find an electron, which is the absolute square of the wavefunction $|\psi(0)|^2 e^{-2\kappa z}$, is non-zero and thus, the electron can tunnel through. As depicted in figure 2.2 the workfunction Φ is the minimum amount of energy required to excite an electron from a metal substrate to the vacuum level. In the following we assume that the workfunctions of the tip and the sample are equal and that the potential U is equal to the vacuum level which results in $U(z) - E = \Phi = \Phi_T = \frac{1}{2}(\Phi_T + \Phi_S)$. If we now apply a small bias voltage ($E \ll \Phi$) to the tip, electrons close to the Fermi level have the possibility to tunnel into empty states of the sample. This results in a current which can be described using the transmission probability T , which links the incoming and outgoing current:

$$I \propto T = \frac{I(z)}{I(0)} = e^{-2\kappa z} \quad (2.4)$$

The analytical description of the transmission probability was first presented by J. Bardeen in 1961 [32]. In his approach Bardeen investigated a planar tunnel junction with two metal electrodes separated by a vacuum barrier. The electrodes were hereby far away from each other so that the electron wavefunctions of each of the electrodes can freely decay into the vacuum. The individual solutions are

$$\psi = \psi_{u,v} e^{-iE_{u,v}t/\hbar} \quad (2.5)$$

Bringing both electrodes together the solution of the combined Schrödinger equation

Chapter 2. Scanning Tunneling Microscopy (STM) and Spectroscopy (STS)

is

$$\psi = \psi_u e^{-iE_u t/\hbar} + \sum_{v=1}^{\infty} c_v(t) \psi_v e^{-iE_v t/\hbar} \quad (2.6)$$

and has a probability to transfer a state from one electrode into the other. In the elastic tunneling regime the energy of the tunnelling electron in its initial and final state is equal $E_u = E_v$. The inelastic case ($E_u \neq E_v$) will be discussed later in section 2.2. With the approximation that two sets of wavefunctions are orthogonal $\int \psi_u^* \psi_v d^3\vec{r} \approx 0$ we insert the solution into the Schrödinger equation and define the transmission matrix element to be

$$M_{uv} = \int \psi_u U_2 \psi_v^* d^3\vec{r} \quad (2.7)$$

with U_2 being the potential of electrode 2. The tunneling current can now be described as

$$I = \frac{2\pi e^2}{\hbar} |M_{uv}|^2 \rho_2(E_F) \rho_1(E_F) \quad (2.8)$$

Rewriting the transmission matrix element by evaluating a surface integral of the two free electron wavefunctions at the surface of the separation, it follows

$$M_{uv} = \frac{\hbar}{2\pi} \int \left(\psi_u \frac{\partial \psi_v^*}{\partial z} - \psi_v^* \frac{\partial \psi_u}{\partial z} \right) dx dy \quad (2.9)$$

Interestingly, the potential barrier doesn't play a role in the tunneling matrix element. Introducing this matrix element into 2.8 and approximating the Fermi distribution function to be a step function at low temperatures, it yields for the current at low bias voltages:

$$I = \frac{4\pi e}{\hbar} \int_0^{eV_B} \rho_2(E_F - eV_B + \epsilon) \rho_1(E_F + \epsilon) |M_{uv}|^2 d\epsilon \quad (2.10)$$

Assuming that the magnitude of the matrix element doesn't change in the range of the bias voltage that is considered, the tunnel current is a convolution of the density of states (DOS) of both planar metals.

In the case of STM electrons don't tunnel anymore between two planar metal junctions, since a tip is scanning the surface. In order to circumvent this challenge J. Tersoff and D.R. Hamann proposed their still widely applied Tersoff-Hamann model [33]. In this model the tip is a locally spherical potential well with a radius R , a center position \vec{r}_0 , and the nearest distance to the surface d . The matrix element from 2.9 can be evaluated for a s-wave tip to

$$M_{uv} = \frac{\hbar^2}{2m} 4\pi \kappa^{-1} \Omega_2^{-1/2} \kappa R e^{\kappa R} \psi_v(\vec{r}_0) \quad \rightarrow \quad M \propto \psi(\vec{r}_0) \quad (2.11)$$

with Ω_2 as the tip volume. If the DOS of the tip (ρ_2) is constant in the probed energy

range, we can take it out of the integral in 2.10 and it yields for the current

$$I \propto \rho_2 |\psi(\vec{r}_0)|^2 \int_0^{eV_B} \rho_1(E_F + \epsilon) d\epsilon = \rho_2 \int_0^{eV_B} \rho_1(E_F + \epsilon, \vec{r}_0) d\epsilon \quad (2.12)$$

This equation shows that the tunneling current is proportional to the integral of the sample local density of states (LDOS) at an energy eV_B at the center position \vec{r}_0 of the tip. The derivation of equation 2.12 with respect to the voltage leads to

$$\frac{dI}{dV} \propto \rho_1(E_F + \epsilon, \vec{r}_0) \quad (2.13)$$

This equation is essential to the STM since it allows to get directly the DOS of the investigated system. Commonly, to have a better signal-to-noise ratio, a lock-in technique is used to modulate the bias voltage with a small ac-voltage in the order of a few mV at a certain frequency (≈ 500 Hz) and then to detect the differential conductance at the selected frequency. With this technique it is possible to resolve individual molecular orbitals, gain information about relative changes in the bandgap, probe surface states, and many more.

2.2 Inelastic Tunneling Spectroscopy

By introducing molecules ($\text{CH}_3(\text{CH}_2)\text{COOH}$ and CH_3COOH) into a metal-metal oxide-metal (Al- Al_2O_3 -Pb) tunnel junction, R.C. Jaklevic and J. Lambe found peaks in the second derivative of the tunneling current which were not present without the molecules [34]. By substituting the hydrogen of these molecules with its isotope deuterium, the energies of the features redshifts, which is known as the isotope effect. Hence, these features could be linked to the vibrational states of the introduced molecules. The frequency of the vibration can be described approximately with

$$f_{\text{H,D}} = \frac{\sqrt{k}}{2\pi} \sqrt{\frac{m_{\text{H,D}} + m_{\text{C}}}{m_{\text{H,D}} m_{\text{C}}}} \quad (2.14)$$

Since the chemical bonds of the molecules should be the same in the normal and the deuterated version the spring constant k is also the same in both cases. Due to the increased mass of the deuterium ($m_{\text{D}} \approx 2 \cdot m_{\text{H}}$) the frequency shifts to approximately 3/4 of the frequency of the undeuterated molecule ($f_{\text{D}} \approx 3/4 \cdot f_{\text{H}}$) [35]. In their research, Jaklevic and Lambe saw a shift from 360 mV to 275 mV which qualitatively agrees to this theory. The vibrational states are interesting since they allow direct chemical identification of the molecules which is used in Raman spectroscopy, electron energy loss spectroscopy (EELS) and IR spectroscopy. The advantage of this technique compared

Chapter 2. Scanning Tunneling Microscopy (STM) and Spectroscopy (STS)

to EELS or IR spectroscopy is that only as few as 10^9 molecules are needed to give a reasonable spectrum and the ability to detect certain weak or even forbidden optical transitions [36, 37].

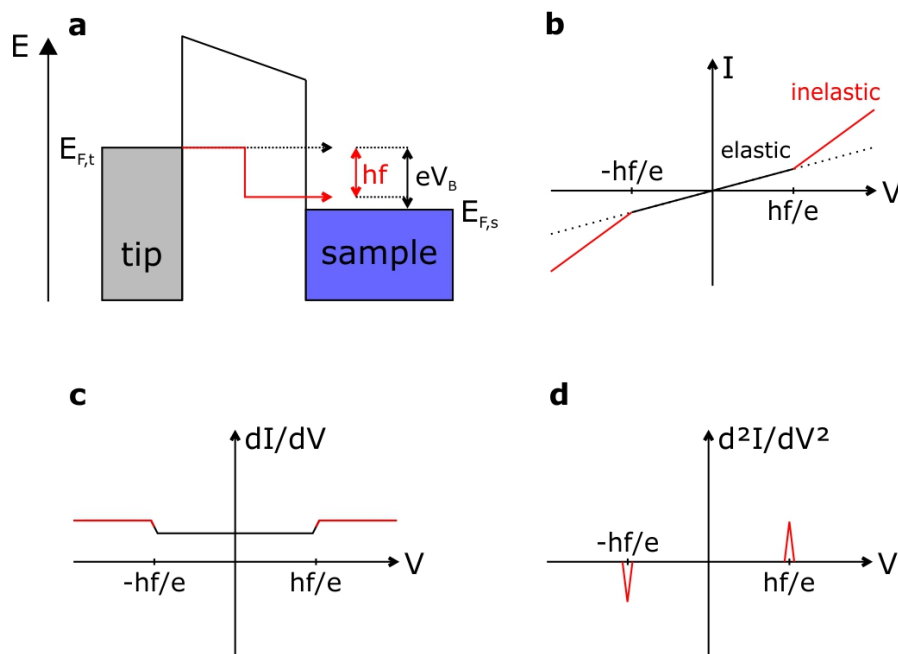


Figure 2.3: Working Principle of STM-IETS **a**, Energy level diagram showing if the applied bias exceeds the vibrational energy a new inelastic tunneling channel is opened. This leads to an increase in the conductance at the bias voltage corresponding to the vibrational energy, which can be seen as an increase of the slope in the I-V- (**b**), a step in the dI/dV -V- (**c**) and a peak in the d^2I/dV^2 -V-curve (**d**).

The adaptation of the inelastic tunneling spectroscopy (IETS) to the STM for the chemical identification of single molecules was first predicted theoretically in the late 1980s [38, 39, 40]. These studies not only present a fundamental theoretical model but also predict the inelastic tunneling contribution to be in the order of 0.1-1% of the total current. This led to the pioneering experimental work in the group of W. Ho in the late 1990s [22, 23, 24] which showed for the first time that it was possible to obtain molecular vibrations of singly adsorbed molecules on metal surfaces and thus, chemical identify and distinguish different molecular species. Additionally, it also allowed the imaging of molecular structure and chemical bonding [41]. In general, long data acquisition times are used to get a reasonable signal-to-noise ratio (10-100 minutes per spectrum). This was only possible due to the advances in mechanical stability and the use of cryogenic temperatures due to the low IETS signal and already small conductance changes would smear out the signal. There are two techniques to obtain the second derivative of the current by either directly recording the second harmonic of the lock-in frequency or by mathematical derivation of the differential

conductance. The latter we will use in the following. The schematic of the working principle of STM-IETS is depicted in fig. 2.3. Electrons can tunnel inelastically from occupied states in the tip to unoccupied states in the sample if the applied bias voltage is equal or above the energy needed to excite a molecular vibration (a, red). This excitation can occur by two different mechanisms: 1. Dipole excitation in which the field produced by the tunneling electron and the transition dipole moment of the vibrational mode interact or by 2. Resonant excitation in which the tunneling electron is shortly trapped in an unoccupied or partially occupied molecular orbital [42, 43]. In the metal-molecule-metal tunnel junction, the inelastic tunneling can occur independent of sign of the applied voltage. This opens another channel for the electrons to tunnel which enhances the conductance and can be seen as an increase in the slope in the I-V-curve (b), a step in the dI/dV -V-curve (c) or as peaks in the d^2I/dV^2 -V-curve (d). The symmetry around the Fermi level for this system allows to differentiate molecular vibrations from other tunneling contributions.

In general, the well-studied selection rule for the detection of vibration modes in IR spectroscopy and Raman spectroscopy are different and hence, both techniques are complementary [37]. Also in STM-IETS selection rules apply but are not as rigorous as in the other techniques, where some transitions are forbidden. Lorente et al. presented a combined theoretical and experimental study identifying symmetry related selection rules [44]. Investigating the symmetry of the projected density of states (PDOS) at E_F and of the vibrational mode lead to the conclusion that in order to keep the matrix element $\langle \psi_a | \delta v | \psi_\lambda \rangle$, which creates the inelastic tunneling signal, nonzero, both have to have the same symmetry (e.g. symmetric PDOS around E_F and symmetric vibrational mode).

The conventional use of noble metals as substrates in STM-IETS stems from the smooth and substantial DOS in the energy region around E_F , which is desirable to be able to distinguish vibrational from other peaks. This is also the reason why this technique has not yet been studied extensively for molecules on semiconducting substrates. In order to have substantial DOS around E_F the semiconducting substrate has to be highly doped to provide states close to the Fermi level resulting in a shift of one of the bands. However, measuring the peaks in the bandgap is technically challenging and thus, the symmetry around E_F of the molecular vibration no longer holds making it harder to differentiate between vibrational and electronic peaks.

2.3 The Gate-STM

2.3.1 Precision Laboratory

All the STM measurements in this thesis were performed on the homebuilt Gate-STM (GSTM). During this work, the GSTM was moved from the sixth floor into the new precision laboratory of the Max Planck Institute for Solid State Research in Stuttgart, Germany. This new building presents state of the art vibration isolation. To achieve this level, vibration measurements were first performed on the campus to determine the best area to build the building. Additional to the heavy fundament of the measurement hall which is separated from the office and machining buildings, the experimental setups are placed into electromagnetic and acoustic shielded boxes on reinforced concrete blocks of a weight around 150 t (see figure 2.4a). These blocks are further separated from the main fundament via air dampers. Taken all together the vibrational level could be significantly reduced from the sixth floor (black curve in figure 2.4b) to the precision laboratory (red curve) making this building a unique place for high precision measurements, which was crucial to the performance of tunneling spectroscopy used throughout this thesis. With this environment and assuming a change of one order in magnitude for the tunneling current if the tip-sample distance changes by 1 Å (see equation 2.4), we have a general stability of our STM of less than 0.8 pm.

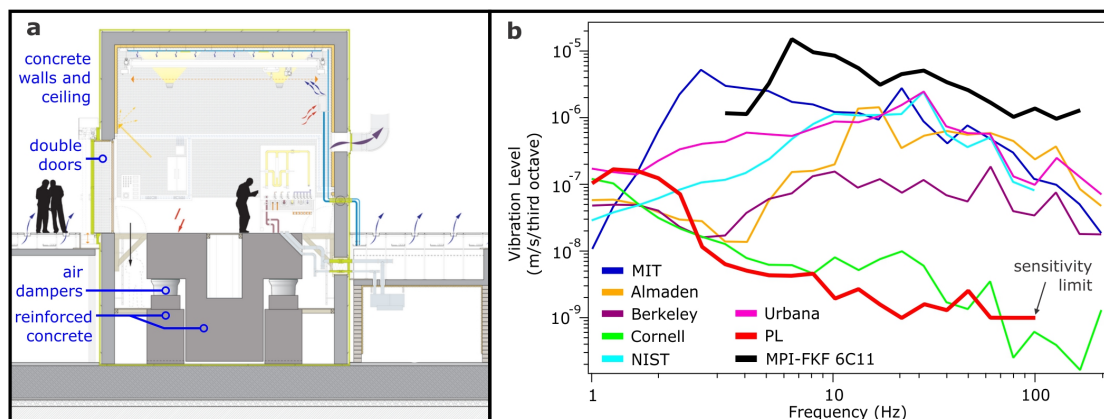


Figure 2.4: Precision Laboratory of the Max Planck Institute of Solid State Research. **a**, Example of one of the electric and mechanical isolated boxes in which the STMs are placed. **b**, Vibration level measurements of the precision laboratory (red) in comparison to the 6th floor (black) and other laboratories.

2.3.2 The Instrument

The GSTM, which can be seen in figure 2.5, is working under UHV condition which requires the use of two chambers, a preparation (yellow) and a STM (red) chamber separated by a plate valve. The transfer of samples or tips between those chambers occurs using a linear transfer manipulator. This manipulator is also equipped with a tube through which it can be cooled either using pressurized air or liquid gases. This allows the preparation of samples at low temperatures down to 100 K. Before measuring the samples with the STM, samples and tips were prepared in the preparation chamber after being introduced via a load lock from ambient condition. Therefore, the system is equipped with an Argon ion sputter gun, gas leak valves and an annealing stage to heat up samples to several hundred °C. Moreover, it is possible to deposit molecules or metals using attached evaporators or the water leak valve. The detailed preparation procedures for the noble metals and tips as well as for the TiO₂ anatase (101) crystals are described in section 2.3.3 and 3.1, respectively. To realize a good vacuum within the chambers with a base pressure of 1×10^{-10} mbar, the system is equipped with a membrane pump, three turbomolecular pumps and two ion getter pumps (IGPs). During operation all pumps except the IGPs were switched off to reduce the vibrational noise level. In the STM chamber, the STM is cooled down to 5 K by a liquid helium bath cryostat which results in an even lower base pressure of $< 1 \times 10^{-11}$ mbar since it acts similar to a cryogenic pump. To ensure a low liquid helium consumption an additional liquid nitrogen shield surrounds the cryostat. Further information about the realization of the GSTM can be found in Ref. [45].

The STM head and helium bath cryostat are vibrationally decoupled from the liquid nitrogen shield and the rest of the system by an upper air damping stage. The lower damping stage used before the movement of the system to the precision laboratory initially decoupled the whole system from the ground but was not anymore needed in the new building due to the good vibration isolation of the concrete ground.

2.3.3 Tip and Noble Metal Crystal Preparation

Having a well-shaped and sharp metallic tip is a strong necessity while doing STM. For all the measurements performed in this work, we used electrochemical etched Pt_{0.8}-Ir_{0.2} tips (Keysight Technologies, N9801A). We found these tips to be the most stable while working on the metal oxide TiO₂, since other tips like tungsten were oxidized rapidly and thus, not usable anymore. The tips are placed inside a tip exchange stage and introduced into the preparation chamber via the load lock. Subsequently the tips are heated up using the filament of the sample annealing stage to remove residues from the etching process (6 A, 15 mins). After the tip exchange, the new tip is prepared

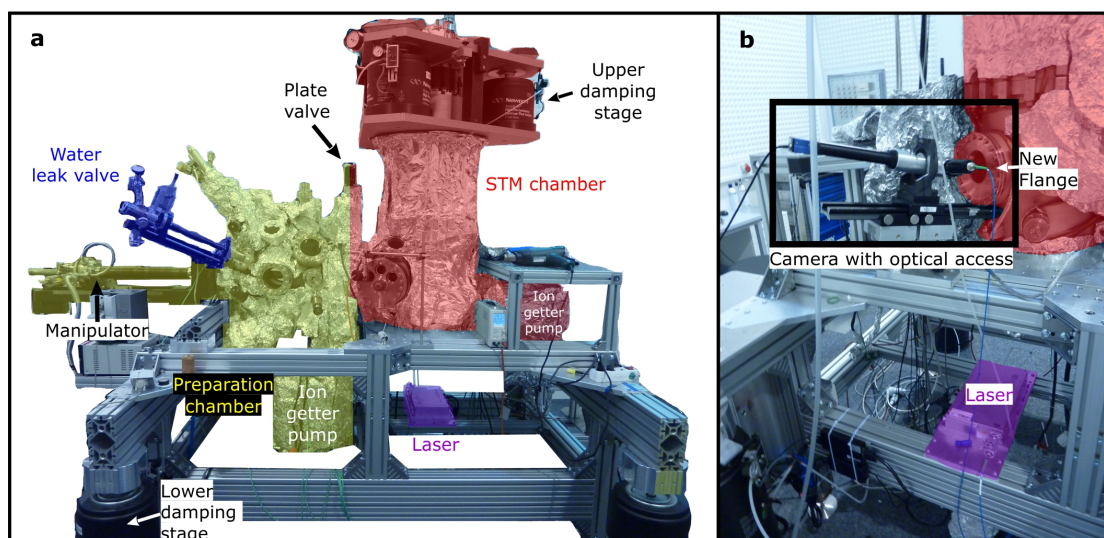


Figure 2.5: The Gate STM. **a**, The GSTM consists of two chambers, a preparation (yellow) and a STM chamber (red) which are separated by a plate valve. The STM unit is decoupled via an upper damping stage. Additionally, the system is equipped with a water leak valve (blue) and a Laser system (purple,**b**).

by a combination of field emission (600 V , $25\ \mu\text{A}$) on a noble metal surface, using high voltage pulses ($7\text{-}10\text{ V}$, $20\text{-}200\text{ ms}$) and tip dips ($1\text{-}10\text{ nm}$). To characterize the quality of the prepared tip, topographic and spectroscopic features (surface state at -0.5 V [46] and image potential states [47]) of Au(111) are used. Since the tip preparation is done on the noble metal crystals, we constantly had to switch between our samples which resulted in contaminations of the samples since they were warming up when taken out of the STM. To circumvent this, we designed a sample garage shown in figure 2.6 in the 5 K cryostat of the STM to be able to switch between the TiO_2 and noble metal samples without warming up the individual crystals.

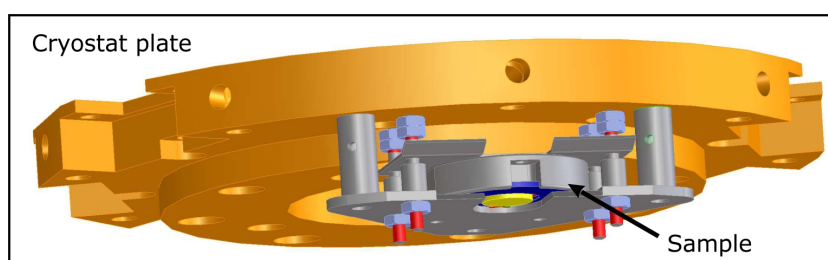


Figure 2.6: Design of the new sample garage in the STM.

The noble metal crystals (Cu(100) and Au(111), MaTeCK GmbH) employed in this thesis are hat-shaped and 7 mm in diameter. The crystals were aligned with an accuracy of $< 0.1^\circ$ and mechanically polished. The preparation of the crystals in the preparation

chamber consists of repeated cycles of annealing (800 K, 10-15 minutes) and Ar⁺ ion sputtering (1 kV ion energy, 60 ° grazing incidence, 10 minutes). This resulted in flat and clean surfaces with terrace sizes of up to 100 nm which are separated by monoatomic steps.

2.3.4 Integration of a Laser System

To investigate the light response of water on TiO₂ anatase (101) system, which is further discussed in the outlook chapter 6, a Laser system (Omicron LightHUB) was purchased. As a first requirement to be able to shine in light into the tip-sample junction the window in our UHV STM chamber had to be exchanged, since it was not ultraviolet (UV) transparent. We chose fused silica (Pfeiffer Vacuum) due to its high transmission in the UV and good stability at a wider temperature range (Fig. 2.7b). Moreover, it was necessary to align the beam direction with the built-in window. For this we changed the flange holding the window resulting in a lower reflection since the laser beam hits the window perpendicular (Fig. 2.7a).

We chose this particular Laser system because it allows us the exchange and modification of the laser sources in an easy way. We carefully chose the wavelengths to be at 355 and 405 nm, which can be changed in a fast manner during operation. The wavelengths were chosen calculating the energy of the photons comparing to the bandgap of TiO₂ anatase (101). Since the bandgap of anatase is 3.2 eV, we wanted to obtain a laser source with high energy photons that can promote electrons from the VB to the CB. Hence, we chose 355 nm (3.5 eV) for one of the laser sources. On the other hand as a reference but also since we create a bandgap reduced phase in section 4.2, we wanted to have a second laser source which is just below the energy of the bandgap (405 nm, 3.06 eV). With this we are able to excite electrons from the VB to the CB in the bandgap reduced phase but not in the normal oxygen-terminated one. More details about these measurements are given in the outlook chapter 6.

After attaching the laser to our frame, we guide the light through an optical fiber into our camera system outside of the vacuum chamber. Since the fiber is fed in on the side of the chamber system which can be seen in figure 2.5b (blue cable), we introduced a beam splitter at this position. This allows us to simultaneously use the laser with our charged-coupled device (CCD) camera (EHD Imaging GmbH, Zoom 125 system, UK1156M CCD camera [45]). The use of our camera system to feed in light into the chamber has the advantage that we can position the light in x-, y- and z-direction and focus the beam onto the sample.

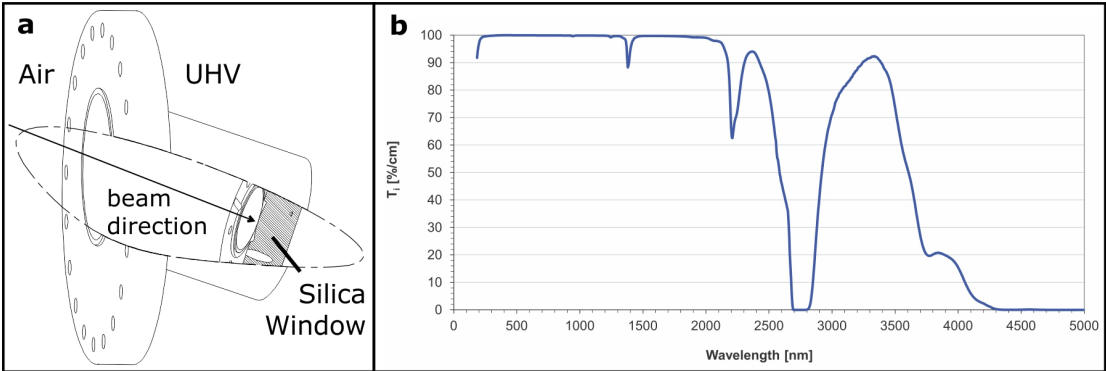


Figure 2.7: New flange and optical transmission of the new window. **a**, Design of a new flange to support the new fused silica window as well as bringing the surface normal of the window in line with the beam direction to reduce potential reflections. **b**, Optical transmission spectrum of fused silica. In the wavelength range of interest around 355 and 405 nm the transmission is >95%.

3 Titanium Dioxide (TiO₂)*

TiO₂ is the natural oxide of titanium and has widespread applications in industry due to its non-toxicity, high abundance and wide-bandgap which results in a yearly production of around 5 million tonnes [49]. Recent market analysis even predicts that the global TiO₂ market will experience a further growth leading to a production of up to 7.5 million tonnes in 2019. 80% of the produced TiO₂ is used as pigments in varnishes and paints due to its high refractive index [50]. An additional 8% is produced for the use in cosmetic or food products. The remaining 12% are used in technical applications like pure titanium, catalysis, conductors or chemical intermediates. TiO₂ is produced using mainly the mineral ilmenite (FeTiO₃) or directly using rutile TiO₂ ores.

Due to the high relevance in industry TiO₂ belongs to the most studied metal oxides. A main driving force for surface studies is the fundamental understanding to improve catalytic reactions on metal oxides. TiO₂ has thereby served as a model system for heterogeneous catalysts using metal clusters. Although first studies by Haruta et al. on Au clusters on TiO₂ and other metal oxides investigating the oxidation of CO to CO₂ were already done in the late 1980's [51, 52, 53, 54, 55, 56, 57, 58] there is still a strong and active research trying to enhance catalytic reactions [59, 60].

Another strong field of surface research is the performance of TiO₂ under light. In photocatalysis TiO₂ received a lot of attention due to the pioneering work of Fujishima and Honda in 1972 who found that TiO₂ can photocatalytically split water without using an external bias [5]. This part of research will be further discussed in chapter 5. A lot of work has also been dedicated to the photo-assisted degradation of organic molecules for self-cleaning purposes. In these devices, TiO₂ creates electron-hole pairs when enlightened with UV photons leading to a formation of radicals when reacting with adsorbants like water. These radicals can then interact with the pollutants degrading and thus, cleaning the surface or surrounding. This research has found a

*Parts of this chapter are based on publication #4 [48] of the CV publication list.

number of applications ranging from cleaning of wastewaters [61] over disinfection of surfaces [62, 63] to self-cleaning coatings of windshields and windows [64, 65].

Modern photovoltaic applications like dye-sensitized solar cells (DSSCs) [4] or the highly emerging perovskite solar cells [6, 7, 8] use mesoporous TiO₂ as support material due to its band alignment, stability and high charge carrier mobility. As explained in the introduction in DSSCs, dye molecules are adsorbed on TiO₂ harvesting incoming photons and exciting electrons in higher energy orbitals. These hot carriers are injected into the CB of TiO₂ and the dye molecule is subsequently regenerated by a redox electrolyte. In perovskite solar cells the dye molecules are replaced by perovskites (ABX₃, *e.g.* CH₃NH₃PbI₃) resulting in record efficiencies of over 20% [9] making this technique industrial relevant with first commercially available modules being potentially released in 2017 [10].

For all application areas, the fundamental understanding of the TiO₂ anatase (101) structure is of detrimental importance. Especially the influence of VOs and step edges for the catalytic activity of the anatase surface is a field of strong interest [13, 66, 67]. These studies could show that VOs are catalytic active centers, which will be described more in detail in section 3.1.2. Still, the origin of higher chemical reactivity of the [-111] step edge on anatase (101) remained unclear. In the following chapter, we will present after the introduction of the surface structures of the different TiO₂ polymorphs (anatase and rutile), a new step edge model of the high reactive edge on anatase (101) explaining the origin of the higher chemical reactivity to come from embedded VOs.

Anatase vs Rutile

TiO₂ has three natural occurring crystal structures rutile, anatase and brookite, whereas rutile is the thermodynamical most stable and studied structure. Since brookite is technologically irrelevant, we will focus on the rutile and anatase crystal structures. Both crystal structures consist of distorted octahedral building blocks in which six oxygen atoms surround one titanium atom (Fig. 3.1). In rutile the octahedra are little distorted and stack with one shared corner alternating by 90°. The unit cell is body-centred tetragonal ($a = b = 4.584 \text{ \AA}$, $c = 2.953 \text{ \AA}$ [13]) with 2 apical Ti-O bonding lengths of 1.98 Å and 4 equatorial Ti-O bonding lengths of 1.95 Å. In anatase the distortion of the octahedron is significant and stacking occurs without alternation of the building blocks. This results in a unit cell with 4 titanium and 8 oxygen atoms with unit cell parameters of $a = b = 3.782 \text{ \AA}$ and $c = 9.502 \text{ \AA}$ and slightly different Ti-O bonding lengths (apical: 1.97 Å, equatorial: 1.94 Å). In both configuration the oxygens are threefold coordinated to titanium atoms in the bulk.

Although being metastable, anatase is even more technologically relevant than rutile,

since TiO₂ crystals with a size below 11 nm coalesce into the anatase termination [12]. This is due to the fact that the thermodynamically most stable surface termination of anatase - the (101) surface (Figure 3.1 f) - has even a lower surface energy than the lowest surface energy termination for rutile - the (110) surface (Figure 3.1 c). The rutile (110) surface consists of five- and sixfold coordinated titanium atoms which are connected via two- and threefold coordinated oxygen atoms which is similar to the anatase (101) surface.

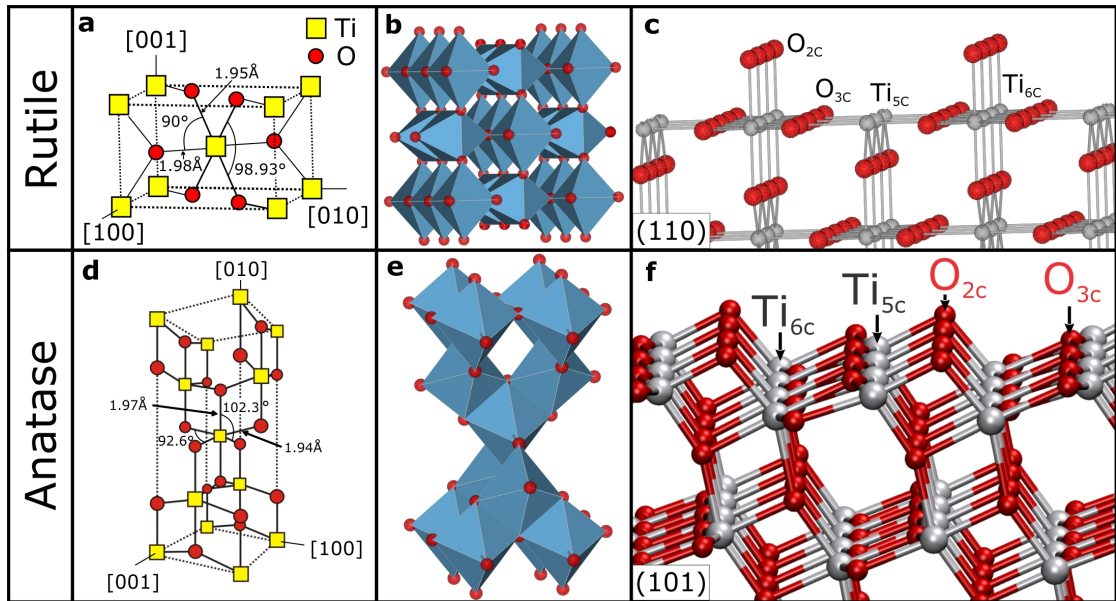


Figure 3.1: Rutile and Anatase. **a,d**, Unit cell of TiO₂ rutile and anatase. **b,e**, Stacking of the octahedral building blocks in the different terminations. **c,f**, Balls-and-stick model for rutile (110) and anatase (101).

Being the metastable polymorph, anatase transforms to rutile at high temperatures giving rise to challenges preparing atomically clean and flat crystals of sufficient size and quality which are needed to study anatase with surface techniques like STM [13]. The transition temperature in air starts around 600 °C [68] but ranges from 400-1200 °C have been reported depending on material properties, atmosphere and particle sizes [69, 70]. The transition is reconstructive which means that breaking and reforming of bonds are involved in the process leaving this transition to be irreversible and time-dependent.

The bandgap of both polymorphs is 3.03 and 3.2 eV for rutile and anatase, respectively. Due to the larger bandgap and a longer lifetime of electron-hole pairs, photoexcited charge carriers are separated more efficiently on the anatase termination resulting in its superior photocatalytic performance over rutile [71, 72]. The relative alignment of the bands in rutile and anatase is still controversial but recent results suggest that anatase exhibits a higher work function than rutile [73]. When rutile and anatase is

combined, which is done in the most common photocatalyst P-25, electrons (holes) can be transferred from anatase (rutile) to rutile (anatase) and the powder exceeds the photocatalytic efficiency of powders only consisting of one of the crystal structures resulting in an even better charge carrier separation [73].

3.1 Preparation of Oxygen-Terminated Anatase (101)

As described before, experimental studies on TiO₂ anatase (101) are scarce due to the challenges in the synthesis and surface preparation. To circumvent this, we employed natural grown TiO₂ anatase (101) crystals throughout the studies for this thesis. The color of the crystals can be used as an indication for the amount of doping apparent in the crystal ranging from isolating (transparent) to conductive (metallic opaque) [13]. We used metallic opaque colored crystals throughout this study which can be seen in figure 3.2a. These single crystals are $4 \times 4 \times (1.5-2)$ mm³ in size and were ordered from SurfaceNet GmbH. It was not possible to use crystals with a bigger height of 2.5 mm and more, since the quality of these crystals was usually insufficient. The single crystals were cut along the (101) plane and subsequently polished resulting in a roughness that was smaller than one lattice constant. We performed XPS, X-ray diffraction (XRD), and resistance measurements to characterize the quality of the samples, which was also subject in the previous thesis [45]. XPS was used to determine the amount of impurities which were found to be lower than 1% for Al, Pb, Zn, Nb and Zr. These impurities act as dopants and are needed to make the crystal conductive which is a prerequisite to perform STM measurements. Due to the onset of the conduction band minimum (CBM), we could conclude that the crystals are strongly n-doped. The XRD data revealed that the crystal was cut precisely in the (101) direction and the resistance measurements were performed to exclude that the crystals are isolating.

The TiO₂ single crystal was mounted, cleaned with high-purity ethanol and introduced into the preparation chamber via the load-lock. The crystals were prepared by repeated cycles of vacuum annealing (920 K, 30 min) and Ar⁺ sputtering (1 kV, 10 min, 60° grazing incidence to the surface normal, 2 μA sample current) to achieve atomically flat and clean surfaces. Since vacuum annealing via electron bombardment desorbs oxygen [74] the surface becomes defective and non-stoichiometric. In order to restore the stoichiometry the sample was annealed at elevated temperatures (670 K) in an oxygen environment (1×10^{-6} , 30 min). The preparation is finished with a final post-annealing step at 920 K for 30 minutes in a residual oxygen environment ($2-6 \times 10^{-9}$) and subsequently the crystal is transferred into the 5 K STM. If the crystal was still not in the desired status, the preparation was repeated.

3.1.1 Characterization of the Anatase (101) surface with STM

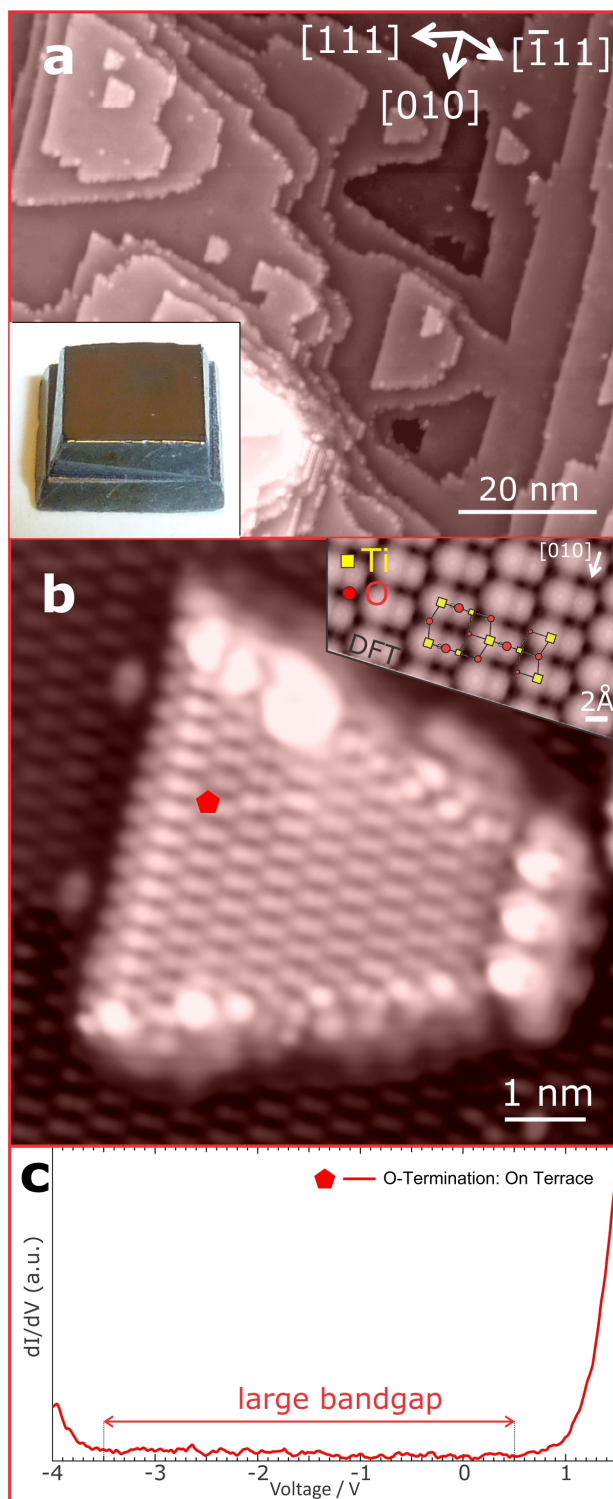


Figure 3.2: Anatase TiO₂ (101). **a**, Empty-states topographic STM image of the TiO₂ (101) crystal. The step edges of the terraces preferentially align along the [010], $[\bar{1}\bar{1}\bar{1}]$, and [111] crystallographic directions. The insert shows the macroscopic TiO₂ crystal with a size of 4 × 4 mm. **b**, High-resolution STM image of an individual island showing rows of dumbbell shape protrusions representing the Ti-O pairs. The insert shows a DFT-based simulated STM image using Tersoff-Hamann with overlaid unit cell in good agreement with the experimental data. **c**, STS on the pristine TiO₂ surface reveals a featureless large bandgap of 4 eV.

In surface science the overall idea for using single crystals is to model the technological relevant pigments with facet sizes of around 20 nm by preparing terraces of similar sizes. This can be seen in figure 3.2a which shows an empty-state STM image of the pristine TiO₂ anatase (101) surface with trapezoidal-shaped terraces separated by monoatomic steps. In general, imaging unoccupied states with the STM lead to better results due to the n-doping of the TiO₂ crystal bringing the CB close to the Fermi level. Imaging the occupied states of anatase (101) holds challenges because the applied voltage needs to be below -3 V which creates instabilities for the tip. The step edges of the terraces preferentially align along the [010], [$\bar{1}11$], and [11 $\bar{1}$] crystallographic directions. The individual white protrusions marked by black arrows in figure 3.2b can be attributed to adsorbates. Since the CB (VB) is mainly governed by cationic Ti 3d (O 2p) states, titanium (oxygen) atoms should be imaged as bright (dark) protrusions in an empty-state STM image. However, the surface oxygen atom stands out of the surface and is thus, closer to the tip which due to the high sensitivity in the tip-sample distance of the STM could also lead to imaging of a bright protrusion. Figure 3.2c shows a high-resolution image of the TiO₂ surface resolving the anatase (101) structure, which can be seen in the overlaid lattice. The dumbbell shaped protrusions which are aligned along the [010] direction resemble the surface Ti_{5c}-O_{2c} pair resolving that both titanium and oxygen are measured with a similar contrast. It was reported that surface O_{2c} should appear brighter than the Ti_{5c} atoms in DFT-simulated and experimental STM images [17]. This was not observed throughout our studies for both experimental and DFT-based simulated STM images [48].

We performed STS on the pristine TiO₂ anatase (101) surface which can be seen in figure 3.2c. The tunneling spectrum reveals a featureless large bandgap of 4 eV that is significantly higher than the value of 3.2 eV reported earlier in this chapter 3. This value is an overestimation due to some of the applied potential in the tip-sample junction is dropped in the sample. This leads to a tip-induced band bending in the surface region of the semiconductor resulting in a shift of the CBM(valence band minimum (VBM)) to more positive (negative) bias voltages in the STS which is common for semiconductors [75, 76, 77, 78].

3.1.2 Oxygen Vacancies

Defects play an important role in modifying physical and chemical properties of metal oxides since defects act as adsorption and catalytic active sites for molecules. The control of the defect concentration is important to increase efficiencies and thus, is well studied [79, 80]. Among all defect sources, oxygen vacancies (VOs) are an important source in metal oxides. VOs have a strong influence on the chemical reactivity [48] and on photocatalytic and -physical properties [81, 82, 83]. In TiO₂ when

3.1. Preparation of Oxygen-Terminated Anatase (101)

a VO is created, an unpaired electron is formed or the VO leaves the neighboring Ti in an undercoordinated state (Ti_{4c}) changing the oxidation from Ti^{4+} to Ti^{3+} and filling up the Ti3d band which results in the formation of bandgap states. This additional reservoir of electrons can be used to enhance chemical reactivity or reducing the bandgap [48]. However, on the anatase (101) surface, isolated VOs are usually not stable and diffuse into subsurface layers away from the catalytically active sites only creating traps for photoexcited charged carriers. Additionally, isolated VOs exhibit repulsive interactions [66, 84, 85]. This limits the ability to modify the surface to enhance chemical reactivity. Hence, the local modification of VO on TiO_2 anatase (101) has been a subject of study in recent years [66, 86]. In these studies STM has been used to apply high electric fields (+5 V tip bias) to pull VOs to the surface and study the cluster behaviour and show the important influence of the vacancies to chemical reactions.

Step Edges

Step edges are representing one of the most common surface defects resulting from the formation of terraces during the growth or preparation process. Similar to VOs, step edges play an important role in improving catalytic performances also acting as catalytically active sites. This is also one of the reasons why TiO_2 anatase is used mostly as nanoparticles since atoms at step edges account for approximately 15% of the total amount of surface atoms for a particle of 3 nm in diameter [17]. Interestingly, TiO_2 has different chemical reactivities depending on the step edge direction which can be seen in figure 3.2a and b, in which step edges along the [010] crystallographic direction have little to none adsorbates, while the other step edge orientation have white protrusions associated with adsorbents. Setvin et al. also presented that step edges along the [-111] direction have a higher electron density using STM [67]. However, the origin of the higher electron density was not clear using the proposed stoichiometric step edge model from Ref. [17].

We investigated this issue by performing STS on the different step edge orientations which can be seen in figure 3.3 [48]. The spectroscopic data taken on the flat terrace (red) and the low reactive [010] direction (black) reveals the same featureless large bandgap of 4 eV (CBM 0.5 V, VBM -3.5 V). When we perform STS on the high reactive [-111] step edge we find a reduction of the bandgap by 2 eV (CBM 0.5 V, VBM -1.5 V) due to the occurrence of a bandgap state around -3 V. In collaboration with the group of Feliciano Giustino from University of Oxford, England, DFT calculations indicated that the additional feature arises from occupied Ti3d states similar to previous studies on undercoordinated Ti_{4c} states (Ti^{3+} states) [87, 88, 89, 90, 91]. When we simulated STM images using the stoichiometric atomistic models from ref. [17] we were able

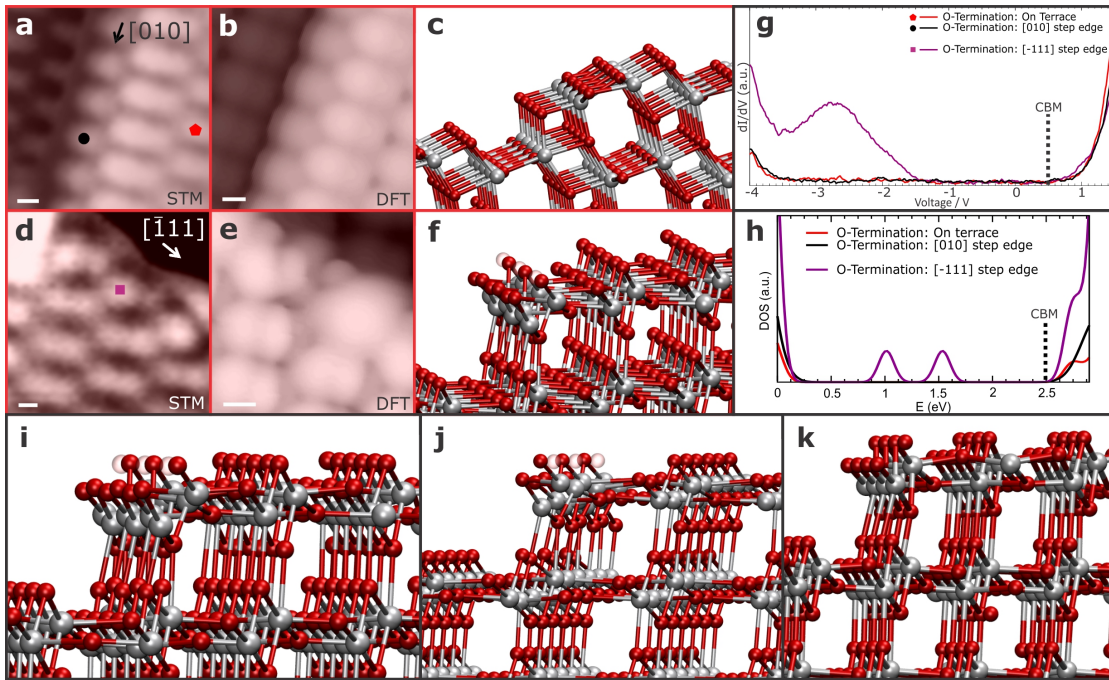


Figure 3.3: Step edges of TiO₂ anatase (101). **a,d**, High resolution STM topograph showing the low reactive [010] and the high reactive [-111] step edge. **b,e**, Corresponding DFT-based simulated STM images on the base of the theoretical models presented in **c** and **f**. Different views on the non-stoichiometric [-111] step edge are presented in **i** and **j** which significantly differ from the stoichiometric step edge model in **k**. **g**, Experimental STS data obtained on the high reactive [-111] step edge reveals a reduced bandgap due to the occurrence of a bandgap state around -2.7 V which could be attributed to Ti³⁺ states. **h**, DFT-based simulated spectroscopy, using the model presented in **f**, can reproduce the bandgap states.

to reproduce the non-reactive [010] step edges but not the high reactive [-111] step edge. Hence, we propose a new non-stoichiometric step model of the [-111] step edge including VOs which can be seen in figure 3.3f. In this model we create one VO every two Ti atoms in the top row leaving the edge Ti atoms undercoordinated. Subsequent DFT-based STM simulated images (Fig. 3.3 e) agree nicely with our experimental data. Additionally, simulating the STS data using DFT with a Hubbard parameter of 3.5 eV, which represents an average of the range of parameters used in previous studies for VOs in TiO₂ [92, 93, 94], reproduces well the occurrence of a bandgap state (Fig. 3.3 h). Moreover, the calculated PDOS does not exhibit any gap states for the stoichiometric [010] step edge. It is important to note that the bandgap in the DFT-based calculation (2.2 eV) considerably underestimates the actual bandgap by 1 eV which is common for semiconductors using DFT-based methods [95]. Furthermore, the bandgap state in the simulation is split into two peaks which has been reported in previous theoretical

3.1. Preparation of Oxygen-Terminated Anatase (101)

studies of VOs in bulk TiO₂ but is not resolved in our experiments [96]. Taken together, we presented a new model for the [-111] step edge of TiO₂ explaining its high reactivity to origin from VOs. Hence, step edges are a way to control the amount of VOs on the surface close to catalytically active sites opening new ways to improve TiO₂-based catalysis.

4 Engineering the Surface Properties of TiO₂ Anatase (101)*

After the introduction of the TiO₂ anatase (101) structure in chapter 3 titanium dioxide (TiO₂) anatase, we will focus in this chapter on engineering the surface properties of anatase (101). As described before, TiO₂ anatase (101) plays an important role in various applications such as catalysis. Hence, considerable effort has been dedicated to engineer the surface properties of TiO₂ influencing chemical reactivity or the bandgap. Depending on the application an increase or decrease in the chemical reactivity of the anatase surface is desired. For catalytic applications an increase of the reactivity is wanted, since it directly improves the efficiency of these devices. On the other hand, for sensors the chemical reactivity needs to be at a minimum to improve longterm stability. In order to implement the surface modifications into production, the procedures have to be reversible and economically cheap. This chapter will present modifications of the TiO₂ anatase (101) surface either reducing or increasing the chemical reactivity by solely changing duration and temperatures of the normal UHV surface cleaning procedure without additional material. Since in both cases the modification only applies to the surface layer, the bulk properties of TiO₂ remain untouched. The tuning of the surface reactivity showcases the potential of the TiO₂ anatase surface possibly stimulating future research in this area.

The first part of this chapter will report on a new oxygen superstructure produced on the TiO₂ anatase (101) surface creating a low-reactive network also reducing the overall roughness of the surface. The second part will present a new surface phase on TiO₂ anatase (101), the so-called Titanium-terminated surface phase, with a higher chemical reactivity and reduced bandgap.

*Parts of this chapter are based on publication #1 [97] and #4 [48] of the CV publication list.

4.1 Oxygen Network

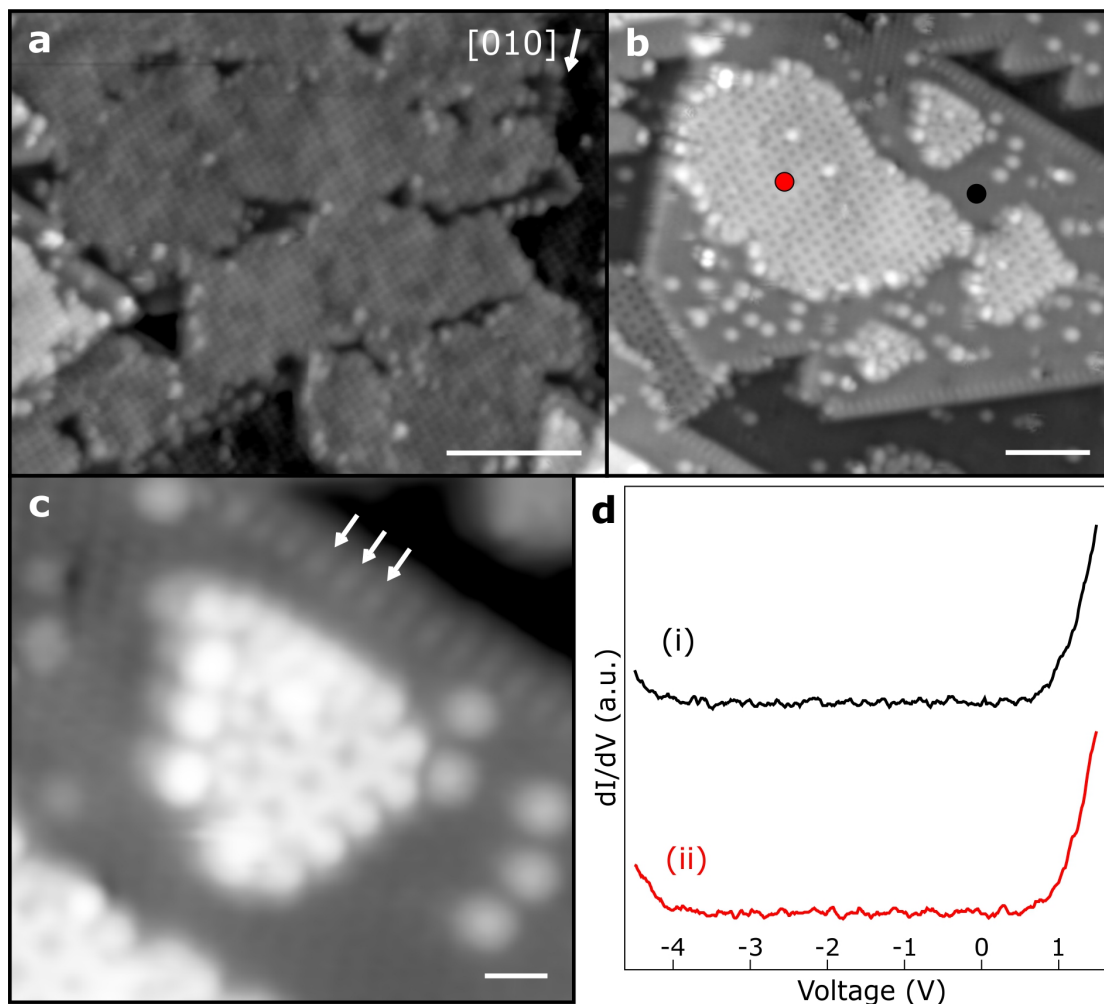


Figure 4.1: Network and its electronic characterization on TiO₂ anatase (101). **a**, STM image of a network formed on top of the TiO₂ anatase surface. **b**, STM topograph showing different network patches on top of a pristine TiO₂ island. The amount of adsorbates on the pristine terrace is substantially higher than on the networks suggesting lower reactivity of the network. **c**, High-resolution STM image displaying an individual small island with nearby adsorbates and the decoration of the step edges. **d**, STS on top of the network (red) and the pristine surface (black) reveals the same featureless large bandgap with no gap states. (scalebars: **a** = 10 nm; **b** = 5 nm; **c** = 1 nm)

Passivation of surfaces plays an important role in engineering material properties, meaning the reduction of chemical reactivity. A common technique is the passivation of metals using small metal oxides to prevent surface corrosion and maintain the bulk properties. In the case of optical sensors based on thin film TiO₂, which are already

available on market (sglux GmbH), the surface properties have to be stable over time and not transform or react with the surrounding. This raises the interest of passivation layers on the TiO₂ surface.

In general, to obtain a clean anatase (101) crystal when newly introduced, the preparation procedure presented in section 3.1 would be repeated multiple times. However, taking a closer look on the surface after only a few preparation cycles at initially slightly higher temperatures (700 instead of 650 °C for the first annealing steps), we find a new mesh-like network which is shown in figure 4.1a. A high-resolution STM topograph of several network patches on the anatase (101) surface is shown in figure 4.1b. We find that the surface of the network patches is substantially cleaner than the surrounding anatase surface hinting that the network is chemically less reactive. Another indication for passivating the TiO₂ anatase (101) surface is that the high reactive [-111] step edges appear to have fewer adsorbates than before (white arrows) when preparing a clean anatase (101) surface (cf. figure 4.1c with section 3.1.2). This step edge shows a stripe-like contrast suggesting decoration of the step edge by the adsorbates. Considering that the step edges along the [-111] direction of the pristine surface are covered with VOs, we believe that molecules which adsorb during preparation fill out the vacancies on the step edges. Performing STS on the network (red) shown in 4.1d reveals the same featureless large bandgap equal to tunneling spectra performed on clean TiO₂ anatase (101) (black). Since there are no gap states appearing, we can conclude together with the topographic images that this network is chemically less reactive than the anatase surface.

The coverage of the networks range on different positions on the crystal from a few percent of a monolayer to nearly a full monolayer coverage. It is interesting to note that the growth of the networks occurs on the terraces and not the step edges which we attribute to the covering of the high reactive VOs. When the coverage is further increased to be close to a monolayer the network can even grow over the step edges of the underlying anatase substrate. This smooths out the surface removing the usual trapezoidal shaped islands of the TiO₂ anatase (101) surface which can be seen in figure 4.1a.

In order to determine the structure of this network we performed a Fourier transform (FT) of the STM image which can be seen in figure 4.2a. The FT reveals that the networks have a rhombic unit cell of $7.4 \times 7.4 \text{ \AA}^2$ and a small angle of $\alpha = 83.5^\circ$. The long diagonal is oriented along the [010] crystallographic direction of the anatase TiO₂ (101) surface. Taking an atomically resolved STM image on a network patch next to a pristine surface area (Fig. 4.2b) allows us to overlay the anatase lattice on the substrate to determine the adsorption sites of the network. A schematic of this process is shown in figure 4.2c. We find that the intersections of the network patch are located on top of hollow sites in the anatase surface. Furthermore, each individual site of the rhombus

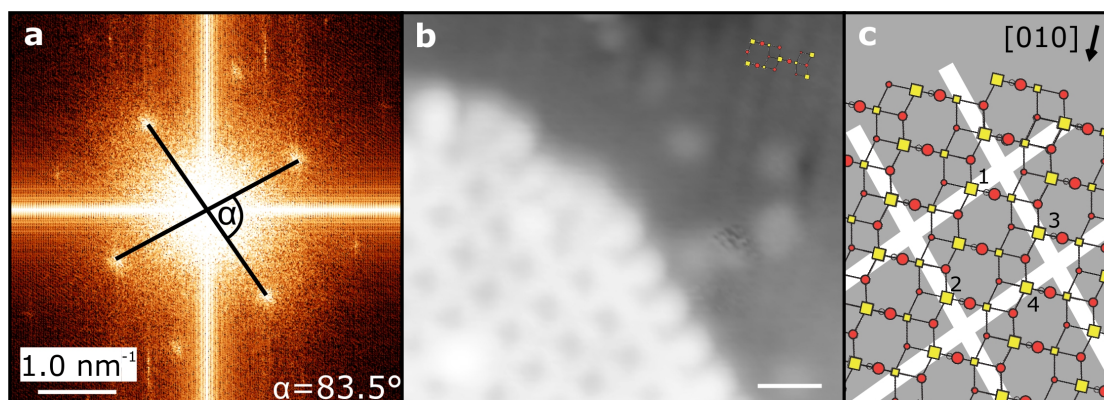


Figure 4.2: Network structure on TiO₂ anatase (101). **a**, FT of the image in figure 4.1a revealing a rhombic structure with a unit cell of $7.4 \times 7.4 \text{ \AA}^2$. **b**, High-resolution STM image allows the identification of the network position with respect to the underlying anatase lattice. **c**, Schematic representation of the network on top of the anatase surface. The intersection fall into the hollow sites of the anatase lattice while the individual sites of the rhombus contain one surface Ti_{5c} (Marked 1-4). (scalebar: **b** = 1 nm)

contains exactly one surface Ti_{5c} atom, which are labeled with 1-4.

We functionalized our tip by picking up one of the adsorbates which can be seen in figure 4.3. In figure 4.3a the unfunctionalized tip displays the DOS of the network homogeneously with no change in electronic contrast. The functionalized tip, however, reveals an electronic substructure which can be seen with enhanced contrast in the insert of b (white border). It becomes prominent that indeed not the intersections are the positions of the molecules but the individual sites of the rhombus. Furthermore, the electronic structure has a little asymmetry which can be explained by the difference in the local surrounding of the molecules and the anatase lattice.

The insert in figure 4.3a shows an enhanced contrast of the black bordered area (white border) displaying a grain boundary in the network. The different network patches are shifted by the distance of two neighboring hollow site in the TiO₂ anatase (101) lattice. Since both lattices are connected, this might be a representation of error correction in the networks. When we recorded voltage dependent STM images, the different scans reveal that no additional states occur in the network or the grain boundary revealing that the two networks behave chemically the same.

The isolated patch in figure 4.4 suggests that the network consists out of the adsorbates present on the anatase surface since the edges of the network patch are decorated with adsorbates that have the same feature size and appearance (blue arrows). The adsorbate free edges also have bigger feature size than the inner network features (yellow arrows). We predict that the networks grow by attaching the surrounding adsorbate (green circles) in a first step and the subsequently incorporating them into

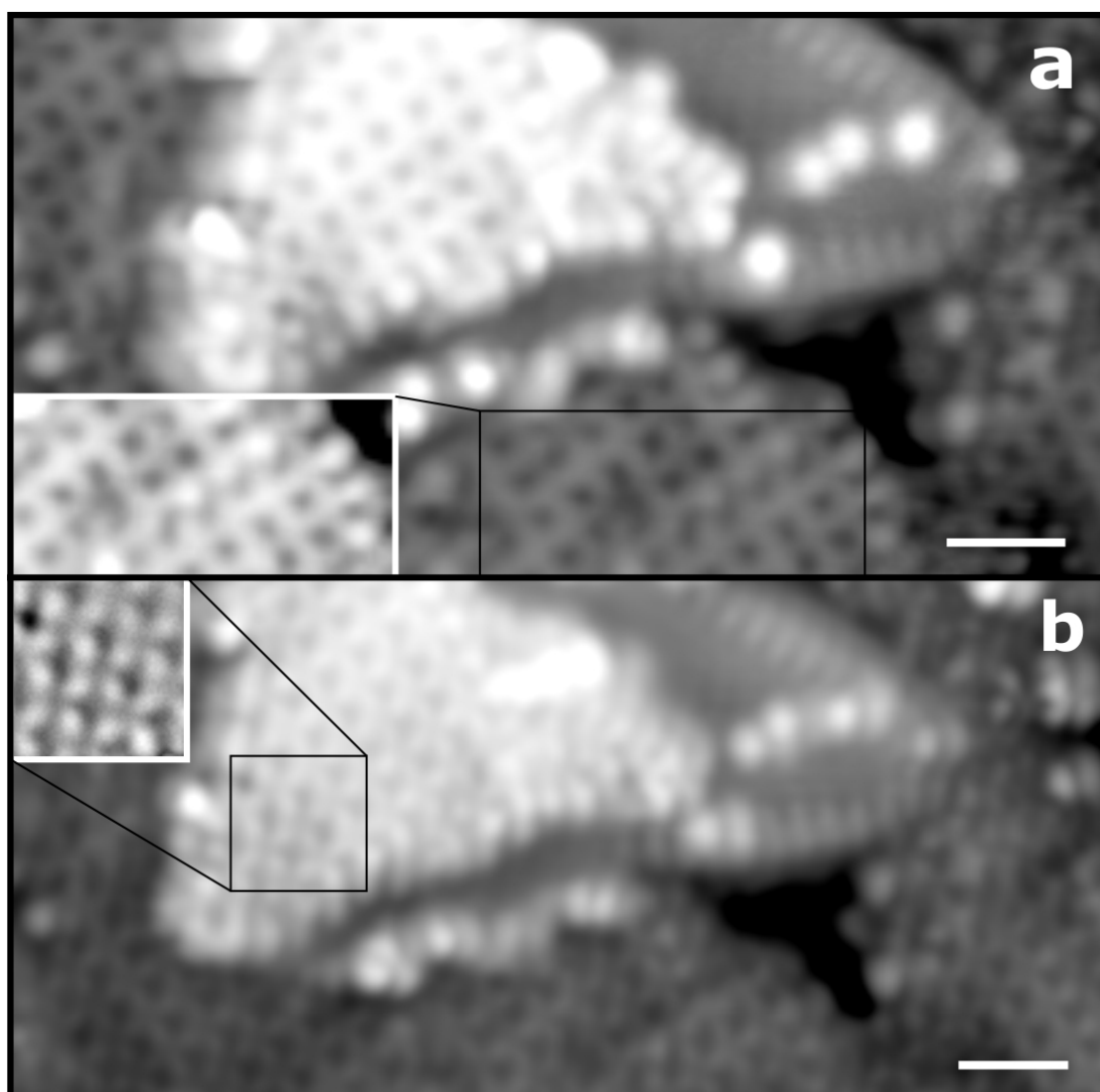


Figure 4.3: Functionalized tip STM image of the network on TiO₂ anatase (101). STM topograph without (**a**) and with functionalized tip (**b**). The functionalization results in an enhanced electronic resolution revealing the substructure of the network (insert in **b**). The molecules are located in between the intersections. The insert in **a** displays a grain boundary. (scalebars: **a,b** = 2 nm)

the network geometry. The second step introduces a change in the orientation of the adsorbates resulting in a change of the DOS which finally ends in the network formation.

Taken together and looking at our preparation, we propose the adsorbates forming this network to be molecular oxygen, which we dosed in our preparation method. In general, molecular oxygen appears as bright features on the anatase surface and can either adsorb in a (sub-)surface VO or on a surface Ti_{5c} in the vicinity of subsurface

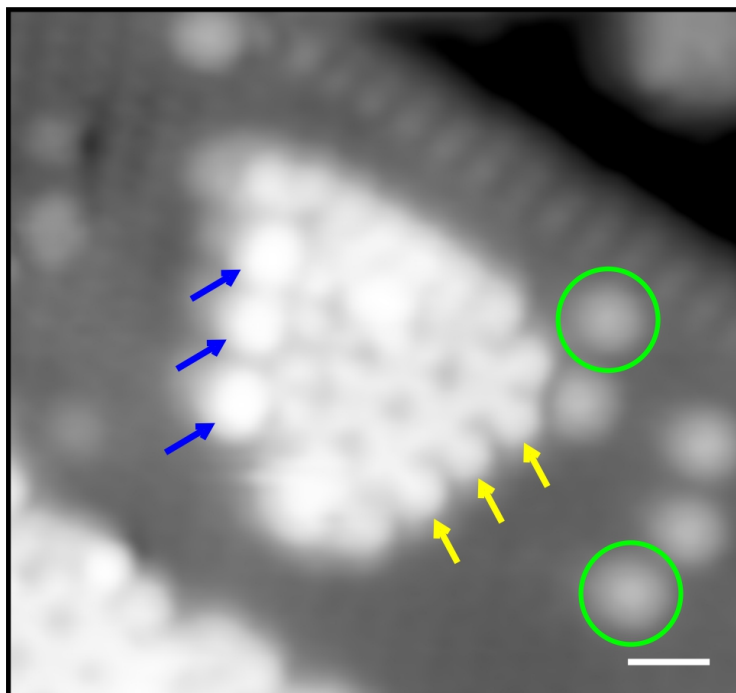


Figure 4.4: Growth of a Network Patch on TiO₂ Anatase (101). High-resolution STM topograph reveals the growth of the network to be a two-step process. After attachment of nearby adsorbates (green circles) onto the edges of the network (blue arrows) the adsorbates get incorporated. The adsorbate free edges also have bigger feature size than the inner network features (yellow arrows).

extrinsic donor atoms along the [010] direction [98]. Since the networks clearly grow on top of the pristine anatase surface and not in the surface plane, the first option can be neglected. Considering the use of a natural grown TiO₂ anatase crystal the occurrence of extrinsic donors migrating to the subsurface is very likely. Moreover, we showed that the network components are adsorbed on the sites of a rhombus. As described earlier, the sites contain exactly one surface Ti_{5c} atom onto which the molecular oxygen could bind. If the amount of oxygen is increased, it then becomes energetically more favorable for the oxygen molecule to rotate its orientation away from the [010] crystallographic direction to form a network.

To confirm those assumption, we will proceed with XPS measurements of the network to determine the network components to be oxygen excluding the growth of an overlayer by metal impurities which are present in the TiO₂ anatase crystal and can migrate to the surface. Furthermore in collaboration with the theory group of Felician Giustino, we will calculate the energetics behind the formation of the network as well as the covering of molecular oxygen of the high reactive step edges.

4.2 Titanium-Terminated Anatase (101)

A main drawback of TiO₂ anatase (101) based photodevices is its large bandgap of more than 3 eV allowing only UV-photons to be absorbed and form electron-hole pairs that can further be separated to generate electricity or participate in a chemical reaction. This limits the overall efficiency of devices to maximal 4% of the total incident solar energy. In order to make the use of TiO₂ economically sound in photocatalysis a lot of effort has been dedicated to reduce the bandgap to the visible using strategies based on ion implantation, doping, composite semiconductors, and metal loading [99, 100, 101, 102, 103, 58, 104]. However, in general these modifications induce defects that act as recombination centers lowering the overall efficiency and substitutional heteroatoms have a limited solubility [13]. A different approach is the modification of the surface structure to introduce bandgap states which showed success on the less technologically relevant rutile (001) surface reducing it by 0.4 eV [105] and on the (011) [106] surface by 0.9 eV.

As already discussed in section 3.1.2 VOs are a source for enhanced chemical reactivity being preferential adsorption (desorption) sites on the anatase surface but have the tendency to diffuse into subsurface layers. However, we found that VOs can be found on steps in order to bring them to stabilize them on the surface, which gives one explanation to the better photocatalytic properties for nanocrystals. Still the amount of edge VOs are relatively low compared to the overall amount of surface atoms considering that only every second oxygen on the high reactive step edges is removed. Hence, it would be desirable to modify the anatase surface in a way to increase the amount of surface VOs and thus, reducing the bandgap and increasing the reactivity but keeping the overall bulk properties of the crystal. The latter is of critical importance since only the surface region (few nanometers in depth) generates photoexcited charge carriers [71] and reduction of the bulk crystal leads to recombination centers reducing the overall efficiency.

In the following we will present a modification of the TiO₂ anatase (101) surface layer which combines both desired attributes, a higher chemical reactivity and a bandgap reduction to the visible.

4.2.1 Preparation of a New Surface Phase on TiO₂ Anatase (101)

The preparation procedure of the clean anatase (101) crystal leading to the oxygen termination was already presented in section 3.1. We tweaked our UHV preparation procedure to first anneal the crystal to 920 K for 20 min in a maximum residual pressure of 2.0×10^{-9} mbar. Subsequently, we let the crystal cool down to below

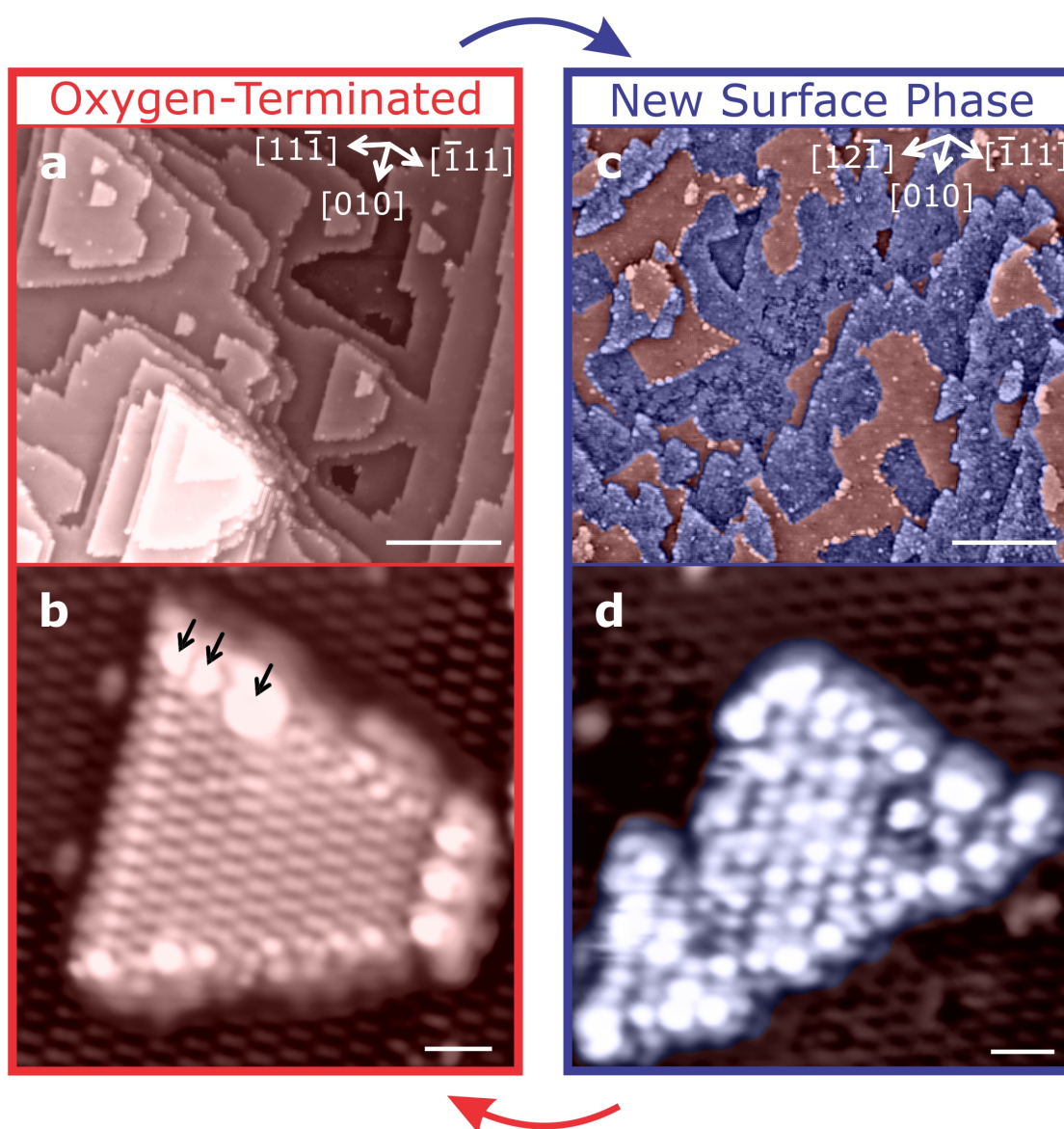


Figure 4.5: Reversible phase transitions of TiO₂ anatase (101). **a,b**, STM images ($V_s = 2.0$ V, $I = 0.1$ nA, $T = 5$ K) showing the pristine oxygen-terminated TiO₂ anatase (101) surface. **c**, STM image after modifying the preparation procedure of the crystal resulting in the creation of a new surface phase (blue overlay) coexisting with the oxygen-terminated phase (red overlay). **d**, High-resolution STM image of an isolated terrace of the new surface phase reveals different preferential orientations for the step edges and a different DOS contrast compared to the oxygen termination. Furthermore, annealing the sample in oxygen atmosphere returns the surface from the mixed state into a pure oxygen terminated surface making this process fully reversible. (scalebars: **a,c** = 20 nm, **b,d** = 1 nm)

4.2. Titanium-Terminated Anatase (101)

330 K and continued our preparation by Ar-ion sputtering at a pressure of about 6×10^{-6} mbar for 10 minutes resulting in a sample current of $1.1 \mu\text{A}$. We performed the sputtering with a grazing incident angle of 20° to the surface plane. The annealing and sputtering was repeated one more time. Following, the crystal was heated up to 920 K for 10 minutes under UHV conditions. Afterwards the chamber was backfilled with molecular oxygen with a pressure of 8×10^{-7} mbar for 30 minutes followed by an annealing in vacuum at a residual oxygen pressure ranging from 3.5×10^{-9} - 6×10^{-9} mbar. The sample temperature remained at 920 K for the whole procedure. When the last annealing step was finished, the crystal was cooled down slowly (0.2 K/s) to room temperature and transferred into the 5 K STM.

This preparation procedure lead to a modification of the surface from the pristine oxygen-terminated TiO_2 anatase (101) surface (figure 4.5a) to a new surface phase (figure 4.5c). We overlaid the new surface phase with blue color to discriminate it more easily from the oxygen termination, since both phases coexist. The transition to the new phase could be reversed by annealing the sample in UHV for 10 minutes, in oxygen atmosphere (8×10^{-7} mbar) for 30 minutes and in residual oxygen (3.5×10^{-9} mbar) for 20 minutes. This fully reversible procedure allows us to study the physical and chemical properties of the new partially covered surface layer.

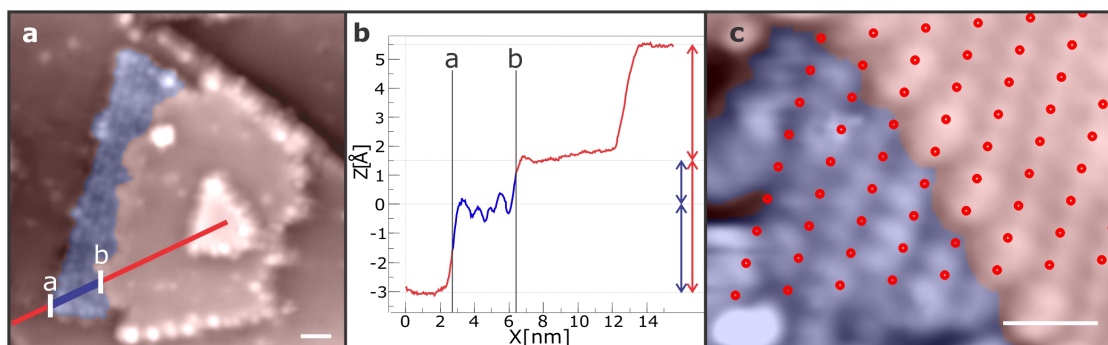


Figure 4.6: Distinguishing both surface phases. **a**, STM topograph showing an adjacent patch of the new surface phase on an oxygen-terminated island. **b**, STM linescan performed over 4 different steps along the line in **a**. The new surface phase is an intermediate step with a step height of 3.0 \AA to the lower and 1.5 \AA to the higher O-terminated terrace. **c**, Overlaid red dotted lines reveal an offset between the protrusions while going from the oxygen termination to the new surface phase. (scalebars: **a** = 2 nm, **b** = 1 nm)

In contrast to the oxygen-terminated surface, this new surface phase shows a different electronic contrast and reveals a high density of adsorbates. In addition, high-resolution STM topographs in figure 4.5b and d reveal that the step edges of an island of the new phase coalesce in different directions than in the oxygen-terminated phase. The $[11-1]$ direction is substituted by a new preferred crystallographic direc-

tion, namely the [12-1] direction, in the new surface phase indicating a local change of the bonding environment. This can also be seen in the different shape of the bright protrusions on the islands. While the oxygen termination shows the known dumbbell shaped protrusions originating from the Ti-O pair, the features on the new surface phase island are more round-shaped.

Additional methods to distinguish both phases are presented in figure 4.6. In figure 4.6a, a linescan over multiple oxygen-terminated islands with an adjacent patch (blue) of the new surface phase is performed. Analyzing the linescan in figure 4.6b reveals that the new surface phase patch is placed in between the steps with a height different of 3 Å to the lower and 1.5 Å to the upper terrace. Figure 4.6c also depicts a patch of the new surface phase adjacent to an oxygen-terminated island. The overlaid red dotted lines show that there is a shift between the points of highest DOS between both phases.

Bandgap Reduction

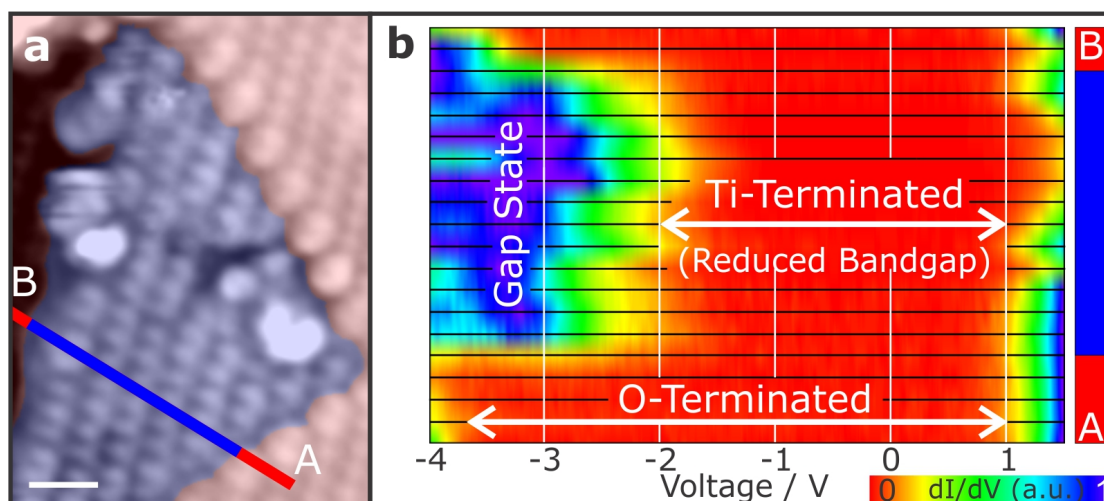


Figure 4.7: Electronic structure of new surface phase. **a**, Atomic resolution STM image of a new surface phase patch embedded into an oxygen-terminated island. **b**, Top view of a waterfall plot presenting 20 tunneling spectra obtained along the line from A to B in **a**. Red areas resemble points of negligible conductance indicating the bandgap. Spectra taken on the oxygen termination show a featureless large bandgap while spectra obtained on the new surface phase present a gap state at around -3 V which significantly reduces the bandgap by 2 eV. (scalebar = 1 nm)

To understand the origin and structure of this new surface phase, we performed STS. Figure 4.7a presents a high-resolution STM topograph of a new surface phase patch embedded in an oxygen-terminated island. 20 individual STS spectra were acquired on a line over both phases from A to B. These 20 spectra are presented in a top-viewed

waterfall plot in figure 4.7b. Note that the color indicates the dI/dV signal and thus, is a sign of conductance. Hence, the red area corresponds to little to none conductance and is an indication for the bandgap. The first 4 spectra, starting from A, are recorded on the oxygen-terminated surface and reveal the well-known featureless large bandgap of around 4 eV (CBM 0.5 V, VBM -3.5 V). Following the spectroscopy onto the new surface phase an additional bandgap states appears around -3 eV significantly reducing the bandgap to 2 eV (CBM 0.5 V, VBM -1.5 V). The reduction of this value, even when tip-induced band bending is included, is significantly higher than the ones presented in the previous section 4.2. Returning to the oxygen-terminated surface at B, the gap state disappears again which concludes that this state is not a tip artifact.

4.2.2 Theoretical Model of the Titanium-Terminated Surface Phase

Summarizing our experimental observations:

- We prepared a new surface phase on the oxygen-terminated TiO_2 anatase (101) surface which can be fully reversed by annealing in oxygen atmosphere.
- The new surface phase exhibits a change in the local bonding configuration which manifests in a change of preferential step edge orientations and the change in DOS.
- The bandgap of the new surface phase is significantly reduced due to the appearance of a gap state around -3 V which is very similar to the state occurring at the high reactive step edge on the oxygen-terminated surface due to the decoration of VOs.

Following these results we propose a structural model for this new surface phase which is terminated by titanium atoms and can be seen in figure 4.8b. In contrast to the conventional oxygen-terminated model in a, the titanium-terminated surface phase lacks the outermost oxygen row resulting in a complete coverage of undercoordinated Ti_{4c} . The structure furthermore undergoes a relaxation, in which the O_{3c} atoms relax outwards by 0.3 Å. As described before on the oxygen-terminated surface, the Ti and O atoms are depicted with similar intensity in STM. Since the outermost oxygen is removed on the Ti-terminated surface, the bright features in the STM images become more round and can now be attributed mostly to the Ti atoms, which can be seen in DFT-based STM simulations in figure 4.8c. The simulation also explains the shift in the points of highest DOS when crossing from the O-termination to the Ti-Termination

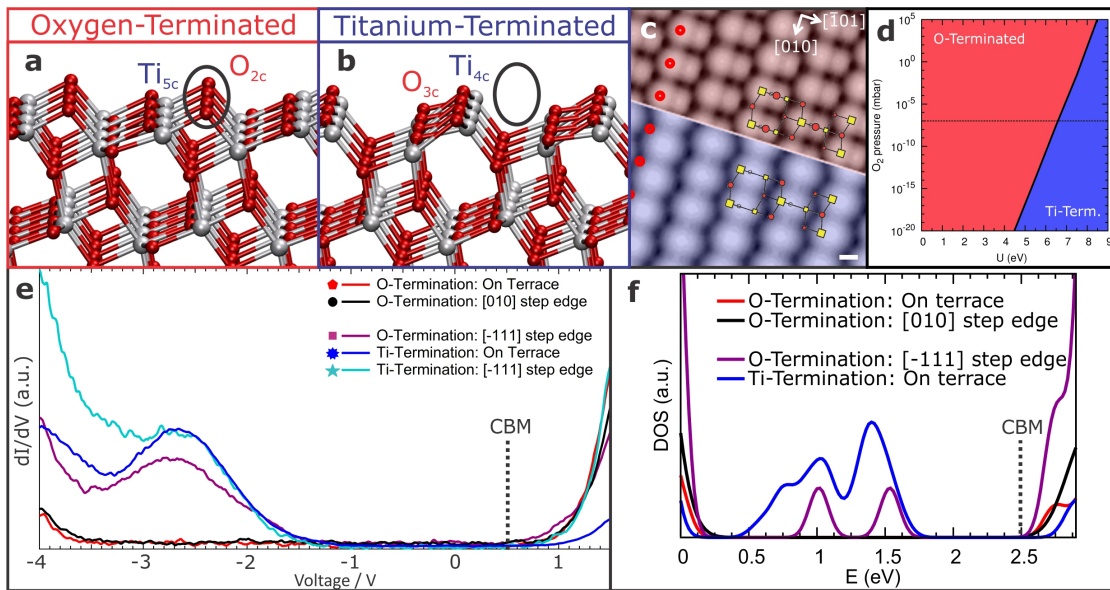


Figure 4.8: Theoretical model of the titanium-terminated surface phase. **a,b**, Theoretical balls-and-sticks model of the oxygen- and the new titanium-terminated surface phase which is created upon removal of the outermost oxygen row resulting in under-coordinated surface Ti atoms. **c**, DFT-based STM simulation of the both phases with an overlaid unit cell. Due to the removal of oxygen the protrusions shift and change from a dumbbell to a more round configuration. **d**, *Ab initio* thermodynamic stability calculation of both phases at 900 K versus the Hubbard parameter U revealing that the Ti-termination can be stable for high values of U . **e**, Experimental STS performed on different positions of the two phases showing strong similarity between the VO decorated [-111] step edge of the oxygen termination and the oxygen depleted titanium termination. **f**, DFT-based simulations of the electronic structure of the different phases showing good agreement with the experimental data in **e**. (scalebar = 0.2 Å)

indicated by the red dotted line.

Figure 4.8e shows the experimental STS data obtained on different areas of the oxygen- and titanium terminated surface. The red and black spectra are taken on the low-reactive terrace and the [010] step edge showing again the large featureless bandgap. The spectra taken independent of position on the Ti-terminated surface (blue and teal) and on the high-reactive [-111] step edge of the O-termination show the same feature since both bandgap states occur from VOs supporting our theoretical model. Using this model to simulate the tunneling spectra shown in figure 4.8f, we find a good agreement to our experimental data.

Since the Ti-terminated surface phase is very reactive, we investigated the relative stability of the two phases using *ab initio* thermodynamic calculations presented in figure 4.8d. The graph represents a phase diagram at 900 K with respect to the oxygen partial pressure and the Hubbard parameter U . For high values of the Hubbard

parameter (U above 6.5 eV) the Ti-terminated surface phase is more stable under the experimental conditions (black dotted line). This value is relatively high but has already been reported in literature [107]. More information about computational details can be found in the method and supplementary information section of ref. [48]. Furthermore we find experimentally that the Ti-terminated phase is stable up to 770 K in vacuum making this phase an interesting candidate for further studies.

4.3 Conclusion and Outlook

In summary, we found that different treatments of the TiO₂ anatase (101) crystal can lead to strong surface modifications changing the reactivity and bandgap. In the first part by exposing the crystal to excessive oxygen at 400 K, we were able to initiate the formation of an oxygen network growing even over step edges reducing the overall roughness of the anatase surface. We found this network to be less chemical reactive than the anatase surface. Moreover, due to the excessive oxygen also the VOs of the high reactive step edges are covered reducing the global reactivity even further. This makes the oxygen network an interesting candidate to passivate the anatase surface from adsorbates maintaining its electronic properties in different conditions. Furthermore, the network could be used due to its porosity for templated adsorption which has been already shown for molecular oxygen networks for adsorption of ammonia on Pt(111) [108].

Changing the preparation method, we could form a new surface phase which is Ti-terminated by removing the outermost oxygen row. This results in undercoordinated surface Ti atoms that increase the chemical reactivity and substantially reduce the bandgap of the surface layer to absorb light in the visible maintaining the bulk properties. This unique combination of the Ti-terminated surface phase opens new possibilities in photovoltaic and -catalytic applications.

5 Water on TiO₂ Anatase (101)*

Water on TiO₂ anatase (101) is of enormous interest to the surface science community due to the broad range of applications ranging from photocatalytic water-splitting (PWS) to self-cleaning coatings. Although numerous applications implicate the interaction of water with TiO₂ anatase, the underlying physical and chemical properties of this interaction remain unclear. In PWS the photo-dissociation of an individual water molecule on TiO₂ anatase (101), the common system in water-splitting devices, has never been observed using a real space imaging technique due to the lack of chemical identification on the single molecular level for this system. Real space imaging is important to disentangle adsorption and the environment of an individual molecule from the actual dissociation process. Not only from a fundamental point of view but also to enhance efficiencies of applications, this presents a very important observation which will have strong implications.

In the following chapter, we will present our solutions to the challenges described before using the unique combination of STM and IETS. In section 5.1, we will introduce this technique chemically identifying CO on Cu(100). Following, section 5.2 we will discuss the observation of molecular fingerprints of water and its components on the TiO₂ anatase (101) surface allowing the individual labeling. The last part of the chapter will present a new structure of an ordered water monolayer on TiO₂ anatase (101) contributing to the discussion of the adsorption of water of TiO₂.

5.1 IETS on CO on Cu(100)

As described in the method section 2.2 the unique combination of scanning tunneling microscopy (STM) and inelastic tunneling spectroscopy (IETS) allows to obtain chemical information on the single molecular level. In order to use this technique for

*Parts of this chapter are based on publication #2 [109] and #3 [110] of the CV publication list.

the characterisation of individual water molecules and hydroxyls on the TiO₂ anatase (101) surface, we first studied the well-known CO on Cu(100) system to calibrate our measurements to have the highest possible resolution.

5.1.1 Preparation

We prepared our Cu(100) crystal by repeated cycles of annealing at 800 K for 10 minutes and Ar⁺ ion sputtering for 10 minutes (2 μ A sputter current) as described in section 2.3.3. This led to a clean metal surface, which we also used to prepare and characterize our tip. Subsequently, the sample was cooled down to 110 K using a liquid nitrogen flow through the manipulator, while we dosed carbon monoxide inside our preparation chamber at a pressure of 10⁻⁷ mbar for 10 seconds (1 Langmuir). To prevent contamination, the IGPs were turned off during the dosing and only the turbomolecular pumps were operating. Afterwards, the sample was introduced into the STM.

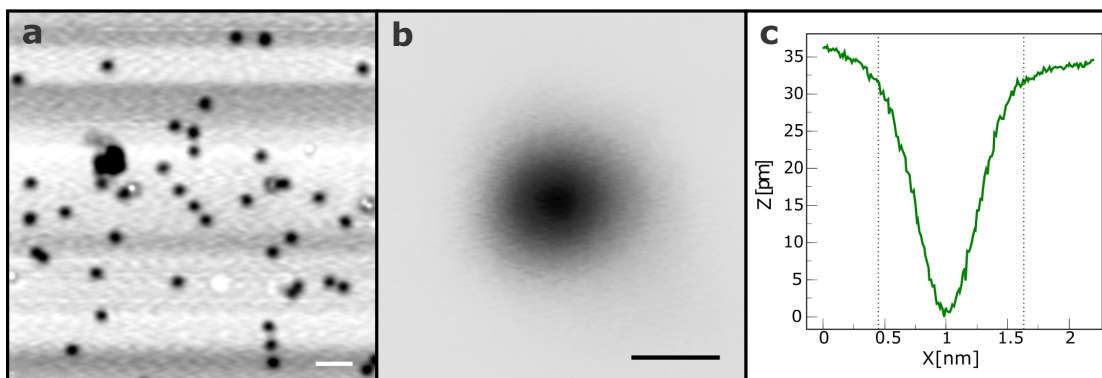


Figure 5.1: Adsorption of CO on Cu(100). **a**, STM topograph of Cu(100) with adsorbed CO molecules (black). **b,c**, High-resolution STM image combined with a linescan over the molecule shows the round feature size of the CO molecule to be around 1.2 nm in diameter and 30 pm in height. (scalebars: **a** = 2 nm, **b** = 1 nm)

This preparation leads to adsorption of CO molecules on the metal surface as presented in figure 5.1a. The constant current image of a single CO molecule in figure 5.1b shows that CO is measured as a dark round protrusion meaning that its DOS is lower than the surrounding DOS of the metal. A linescan over the molecule is displayed in figure 5.1c showing a depth of around 30 pm in good agreement with previous results on other Cu surfaces [111].

CO binds typically with the carbon atom onto metal surfaces resulting in a vertical adsorption. The adsorption can be described using the Blyholder model [112] - a theoretical model extending the known Dewar-Chatt-Duncanson model [113, 114],

which describes metal-ligand interactions using donation and back-donation chemical mechanisms. The CO-metal bond is formed by a charge transfer from the 5σ orbital of the CO into unoccupied metal orbitals and a backdonation from the metal d-band to the empty 2π orbitals of the CO molecule. Depending on the metal substrate CO can bind on atop (terminal), bridging, 3- and 4-fold hollow sites. For d metals the atop site of the metal is the usual adsorption site which is also the case for CO on Cu(100) [115, 116]. The metal-carbon bond is relatively weak and can be easily broken at room temperature which then leads to desorption of CO. Hence, single molecular studies of CO on Cu are generally carried out at low temperatures also explaining the cooling down of the sample during preparation [117].

5.1.2 The Compressed Phase

CO can adsorb in different superstructures on Cu(100) depending on the concentration. If the amount of CO is half a monolayer it forms a $c(2 \times 2)$ structure where the CO is located atop on every second Cu atom [118, 119, 120]. If this amount is exceeded, CO can form a compressed phase, which was first described by Tracy [117]. These structures were later identified as $c(5\sqrt{2} \times \sqrt{2})R45^\circ$ and $c(7\sqrt{2} \times \sqrt{2})R45^\circ$ using low energy electron diffraction (LEED) and EELS [121, 122, 123]. These structures exhibit domains of CO molecules which are separated by ordered arrays of domain walls in which the CO molecules are closely packed, which is shown in figure 5.2b. The difference between the $c(5\sqrt{2} \times \sqrt{2})R45^\circ$ and the $c(7\sqrt{2} \times \sqrt{2})R45^\circ$ lies in the amount of CO molecules per unit cell, which is 3 for the first case and 4 for the latter one [123]. A thorough analysis of the different positions of the individual CO molecules on the Cu surface was done by Thamankar using STM and DFT [124]. In their study it was shown that the structure relaxes by molecular tilting and bending shifting the adsorption of some CO molecules to be non terminal.

We prepared the $c(7\sqrt{2} \times \sqrt{2})R45^\circ$ CO superstructure on Cu(100) using a longer duration and higher pressure while dosing the CO (100 Langmuir: $5 \cdot 10^{-7}$ mbar for 200 seconds). An STM topograph of the structure can be seen in figure 5.2a. As described unit cells of 4 CO molecules with a $c(2 \times 2)$ structure are formed and separated by domain walls (white lines) of closed packed CO. The domains can sometimes be enlarged to double the size which can be seen in figure 5.2b.

For CO on Cu(100), different vibrational modes can be obtained: a C-O stretch mode, a CO-Cu stretch mode, and hindered rotation or translation modes [120]. The energy of these modes have been characterized by infrared-reflection absorption spectroscopy (IRRAS) [125] and also by STM-IETS [111]. To optimize our measurement readout we focused on the hindered rotation mode with an energy of around 36 meV. We obtain the inelastic tunneling signal by recording the differential conductance

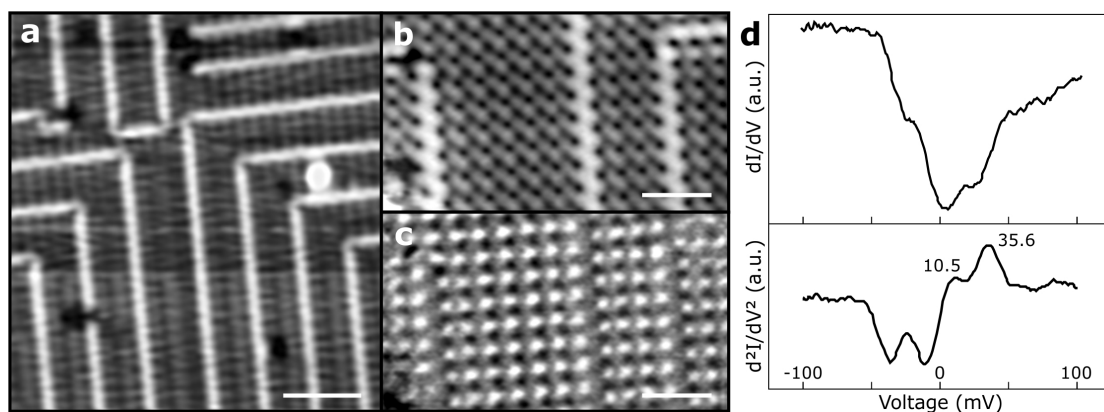


Figure 5.2: The $c(7\sqrt{2} \times \sqrt{2})R45^\circ$ CO superstructure on Cu(100). **a**, STM overview of the superstructure showing different domains of CO molecules separated by domain walls (white lines). Atomic-resolved current (**b**) and d^2I/dV^2 (**c**) maps at the energy of the hindered rotation (35.6 mV) revealing the substructure. The CO molecules at the domain walls relax outwards and thus, do not adsorb on exactly terminal sites of the Cu(100) lattice anymore. **d**, Differential conductance (upper) and the derived spectrum (lower) on CO on Cu(100) showing the hindered rotation mode at 35.6 mV. (scalebars: **a** = 2nm, **b,c**, = 1nm)

and then subsequent mathematical derivation. We carefully chose a modulation voltage of 7 mV for our lock-in system and a measurement time of 15-30 minutes to have reasonable signal to noise levels (integration time 300 ms, 5-10 repetitions). Furthermore, we set the modulation frequency of the lock-in to 420 Hz which was the frequency of minimal noise in our STM noise spectrum.

The differential conductance signal obtained on the compressed phase of CO is shown in the upper part of figure 5.2d. As described in the theory section 2.2 the prominent step-like features in the differential conductance can be attributed to vibrational modes. To enhance visibility we performed the derivation of the differential conductance to end up with a spectrum of the d^2I/dV^2 signal in the lower part of figure 5.2d. Note that in order to reduce the noise introduced during the derivation the d^2I/dV^2 spectrum is Gaussian smoothed 10 times. Due to the derivation the steps occur as peaks and we can determine the peak positions. We found a significant peak at $\pm 35.6 \text{ mV} \pm 2.9 \text{ mV}$, which we identify as the hindered rotation mode of CO. We can use this knowledge to set our bias voltage to 35.6 mV and simultaneously recorded current and the d^2I/dV^2 signal. For this measurement we set the integration time of our lock-in system to 10-30 ms and slow down our scan speed to match every pixel with the integration time resulting in a measurement duration of 30-60 minutes. Using this technique we can clearly see the positions of the CO atoms, since the vibrational mode signal is the highest above the molecule. Hence, the substructure of the phase with its domain walls is revealed (cf. figure 5.2c). It is possible to see the relaxation

of the CO atoms in the domain wall away from each other in good agreement with earlier studies [124]. In the following section we will use this knowledge and settings to apply it to water molecules and hydroxyls on TiO₂ anatase (101).

5.2 Identifying Water Molecules and Hydroxyls via IETS

As already described in the introduction in chapter 1 lots of studies of the dissociation of water on TiO₂ were performed using averaging techniques like photoelectron spectroscopy (PES) or IR spectroscopy. These studies contributed to the overall understanding including that photoexcited charge carriers are separated more efficiently on the anatase termination than on rutile and that oxygen vacancies are formed under ultraviolet light [71, 72]. In particular, the physical and chemical properties of oxygen vacancies and their effect on the surface reaction have been intensively studied [18]. However, the elementary steps of the photo dissociation of a single water molecule on TiO₂ anatase cannot be investigated by these ensemble measurement techniques. This requires a direct imaging technique on the atomic scale, for which STM has been proven to be an ideal tool. However, the key components of water splitting, H₂O and OH, appear too similar in STM to clearly label the individual species. So far, this labeling in STM has been done using topographic data and the behavior of the molecules in different electric fields or temperatures but remained ambiguous due to different tip and sample conditions [126, 98, 127], which even lead to an erratum in Science [128]. A labeling of the different molecules on TiO₂ is crucial to understand the photo-dissociation process and its products. In the following, we use the combination of STM and IETS to label individual water molecules and their components on the semiconductor TiO₂ anatase (101). In general, the use of this detection technique is challenging on semiconductors due to the low DOS at the Fermi level reducing the already small IETS signal even further. However, by using a highly n-doped naturally grown TiO₂ anatase (101) crystal, we create enough states around E_F to detect vibrational peaks of molecular and dissociated water on the anatase surface using IETS. This result is supported by DFT calculations in collaboration with the group of Feliciano Giustino and by investigating the isotope effect for molecular vibrations using deuterated water and hydroxyls.

5.2.1 Preparation Method

To deposit water onto the anatase crystal, we introduced high ohmic distilled water (> 18 MΩ) in a cleaned kovar glass and attached it to our preparation chamber separated

by a valve. We further cleaned the water using repeated freeze pumping cycles to reduce the amount of other adsorbents on the TiO₂ surface. In these cycles, the water was frozen using a small liquid nitrogen dewar. Following, the lines and the test tube connecting to a valve at the chamber were pumped externally by a turbomolecular pump stand. When the pressure reached below 10⁻⁶ mbar, the valve towards the pump stand was closed and the test tube was heated up until the water liquified. This process was repeated at least 3 times.

After the preparation of an oxygen-terminated TiO₂ anatase (101) surface using the method presented in section 3.1, we cooled down the anatase sample to 120 K using a constant liquid nitrogen flow through our manipulator. We backfilled our preparation chamber with H₂O for 10 seconds reaching a pressure of 10⁻⁹ mbar. Afterwards, the sample was introduced to the STM. Since this preparation lead to ice formation, which will be further discussed in section 5.3.1, we subsequently took out the sample from the 5 K STM to let it warm up to room temperature and then reintroduce it into the STM. This removed the physisorbed ice layer and weakly bonded molecules in agreement with temperature programmed desorption (TPD) data which is presented later in this chapter. We ended up with single random molecular adsorption which can be seen in a STM image in figure 5.3a. Using this preparation, we hardly found any aggregates on the terraces or the step edge indicating that the adsorbates are immobile.

5.2.2 H₂O and OH + H

The high-resolution STM image in figure 5.3b shows the individual molecules adsorbed on the anatase (101) surface as dumbbell shaped protrusions of 0.9 nm in size. Due to the atomic resolution, we find that the molecule adsorb on top of a Ti-O dimer row with its center being atop of a surface Ti_{5c} atom. By investigating the individual protrusions we can find slight differences in the contrast. Mainly, we find two species, a symmetric and an asymmetric dumbbell shaped protrusion which is shown in figure 5.3 c and e, respectively. To enhance visibility, we changed the color scale in figure 5.3 d and f. Note that depending on the applied voltage, current, and even temperature (here $V_{\text{bias}} = 1 \text{ V}$, $I = 1 \text{ nA}$, $T = 5 \text{ K}$) the features look different and the two species might not be distinguishable anymore solely by topographic imaging.

To chemically identify the two species, we performed STM-IETS which can be seen in figure 5.4. In order to obtain the IETS data, we record the differential conductance spectrum using the settings presented in section 5.1 (integration time: 300 ms, 7 mV modulation voltage, 5-10 repetitions, measurement time per spectrum 15-30 minutes). Subsequently the spectra were derived, normalized and Gaussian smoothed. The following IETS data will be presented as follows: (i) is the spectrum obtained on the

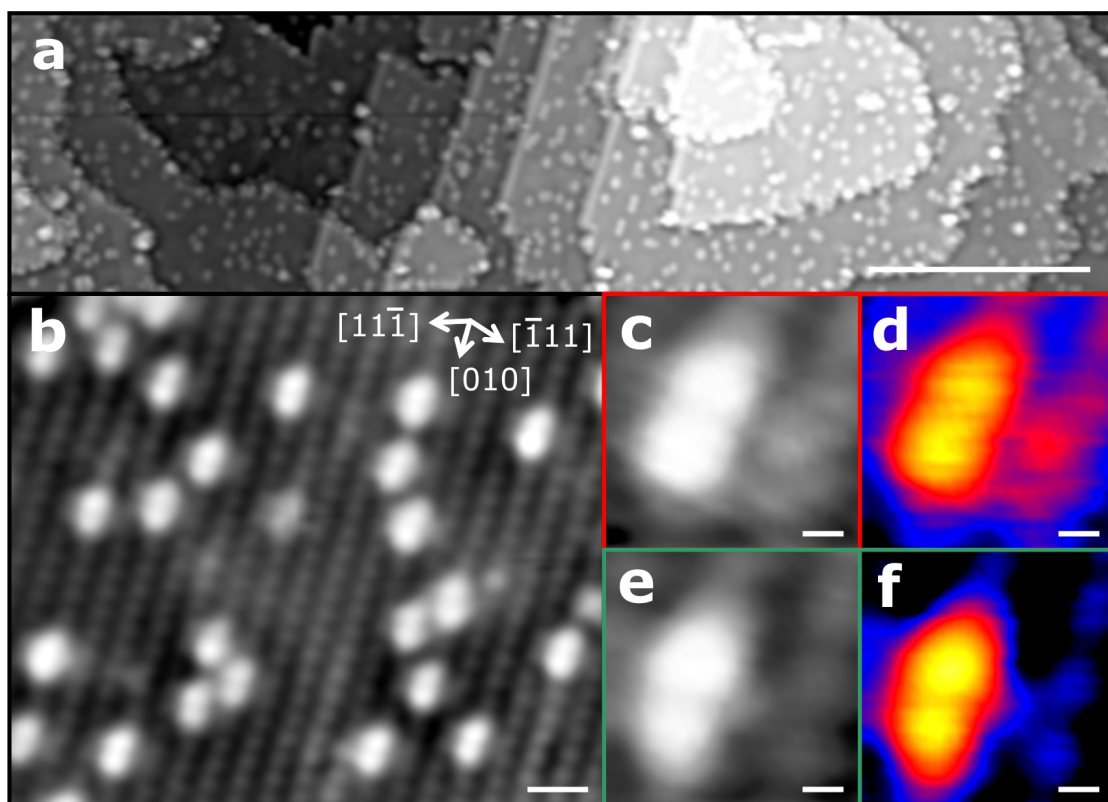


Figure 5.3: Adsorption of H_2O and $\text{OH} + \text{H}$ on TiO_2 anatase (101). **a**, STM overview image of single random water molecules and hydroxyls adsorbed on the anatase surface ($V_{\text{bias}} = 1\text{V}$, $I = 1\text{ nA}$, $T = 5\text{K}$). **b**, High-resolution STM allows the further distinguishing of two species - a symmetric dumbbell shaped protrusion (**c,d**) and an asymmetric one (**e,f**). (scalebars: **a,b** = 1 nm, **c-f** = 0.2 nm)

molecule featured in the insert, (ii) is the corresponding substrate spectrum of TiO_2 anatase (101), and (iii) is the difference spectrum of (i) and (ii). It is important to also record the substrate tunneling spectrum before and after each individual molecule spectrum to remove spurious background signals that are introduced by different tip conditions that might change during measurement [129]. Due to the normalization of the spectra the baseline of the difference spectra might not be flat. However, to avoid artificial data modification the baseline was not fitted and subtracted. Note that the inelastic tunneling spectra were performed hundreds of times on different molecules, thus proving reproducibility. Figure 5.4a presents the IETS data obtained on the symmetric dumbbell protrusion from figure 5.3c and d. We find a clear peak in the difference spectrum (iii) at $191\text{ mV} \pm 12.3\text{ mV}$ and a broader feature in the region between 300-500 mV with a maximum around 474 mV. The lower frequency peak at 191 mV can be assigned to a molecular bending mode $\delta_{\text{bend}}(\text{H-O-H})$ of water which is illustrated in a scheme in figure 5.4c. This is in good agreement with previ-

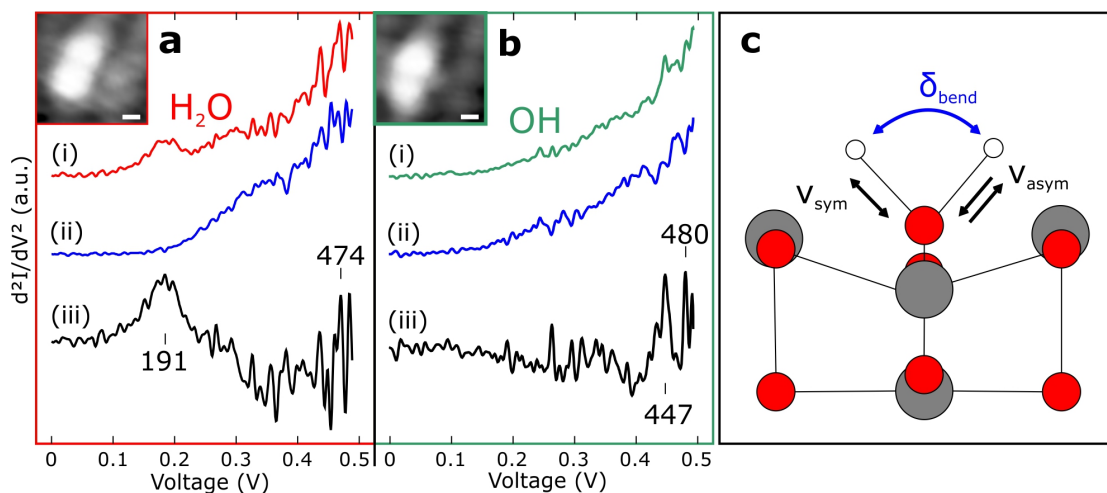


Figure 5.4: STM-IETS of H₂O and OH+H on TiO₂ anatase (101). **a**, STM-IETS obtained on (i) symmetric dumbbell shape protrusion, (ii) the pristine TiO₂ anatase (101) surface, and (iii) the difference spectrum. The difference spectrum reveals a distinct peak around 191 mV and a broader one in the area from 300-500 mV with a maximum at 474 mV. These energies correspond to molecular bending and stretching modes of H₂O allowing us to assign the symmetric protrusions. **b**, The IETS data obtained on the asymmetric protrusions only show a broad peak in the higher energy range with a maximum at 480 mV but no feature around 200 mV. This allows us the assignment of the asymmetric features to be dissociated water molecule (OH+H). **c**, Schematic drawing of the possible molecular vibrations of H₂O on TiO₂ anatase. (scalebars = 0.2 nm)

ous attenuated total reflection Fourier transform infrared spectroscopy (ATR-FTIR) [130] and our DFT-based simulations (Figure 5.5 and Table 5.1). The high standard deviation for this peak comes from the fact that we initially did not distinguish between isolated water molecules and water complexes where a hydrogen bond can be formed as discussed later in this section. On the other hand, the broad feature in the higher frequency regime can be attributed to a superposition of different symmetric and antisymmetric $\nu_{\text{sym,asym}}$ (O-H) stretch modes. Hence, we assign this symmetric dumbbell shaped protrusion to be a single H₂O molecule. The IETS data obtained on the asymmetric feature (figure 5.4b) reveals only a broad feature in the higher energy range with a maximum around 480 mV but no distinct peak around 200 mV. Since, this molecule doesn't have a bending mode, we assign this molecule to be a dissociated water molecule - a hydroxyl with a neighboring hydrogen atom (OH+H).

5.2. Identifying Water Molecules and Hydroxyls via IETS

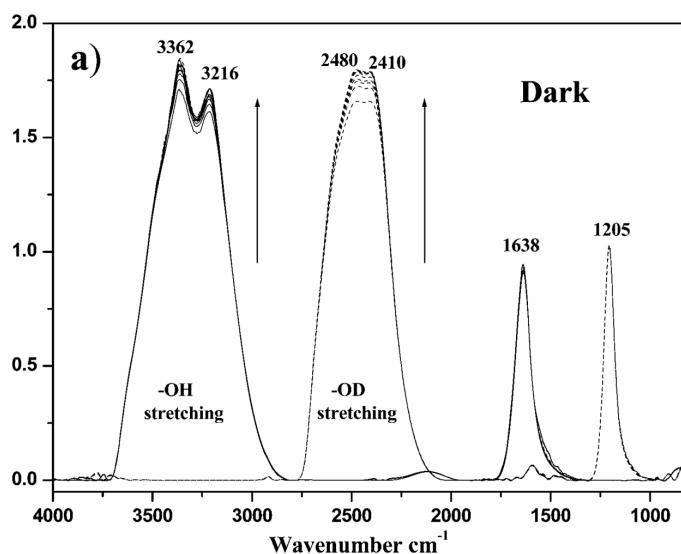


Figure 5.5: ATR-FTIR of H₂O and OH+H on TiO₂ anatase (101) taken from reference [130]. The energies of the vibrations in eV are given in Table 5.1.

5.2.3 D₂O and OD + D

To confirm the origin of the peaks in the IETS data, we investigated the well-known isotope effect. Therefore, the TiO₂ crystal was cleaned using the treatment presented before and we exchanged H₂O with its deuterated form D₂O. Again the heavy water was cleaned by freeze pump cycles and backfilled into the preparation chamber at a pressure of 10⁻⁹ mbar for 10 seconds. The sample was cooled down during the backfilling to 110 K and afterwards introduced into the STM. To obtain single random molecular adsorption, the sample was heated up to room temperature and reintroduced into the STM. This led to similar topographic images as in figure 5.4, since the deuterated water molecules have a similar size as the H₂O molecules and also appear as symmetric and asymmetric dumbbell shaped protrusions. We performed STM-IETS on the different species which is presented in figure 5.6. The symmetric feature in figure 5.6a shows a distinct peak at 146 mV and a broader peak in the higher energy range from 250-450 mV with a maximum around 304 mV. These energies correspond to δ_{bend} (D-O-D) bending and $\nu_{\text{sym,asym}}$ (O-D) stretch modes. As described in the theory section in 2.2 about IETS, the vibration energy should redshift if hydrogen gets replaced by deuterium by approximately 3/4 which is in good agreement with our data ($E_{\text{D}_2\text{O}}(146 \text{ meV}) \approx 3/4 \cdot E_{\text{H}_2\text{O}}(191 \text{ meV})$). This proves the origin of the IETS peaks to indeed stem from molecular vibrations, *i.e.* molecular bending and stretch modes of the water molecule. Using STM-IETS we investigated an asymmetric molecule with a neighboring molecule depicted in the insert of figure 5.6b. We find no distinct

feature around 150 mV but a broader peak with a maximum at 295 mV which allows us the assignment of this molecule to be a dissociated D₂O molecule (OD+D).

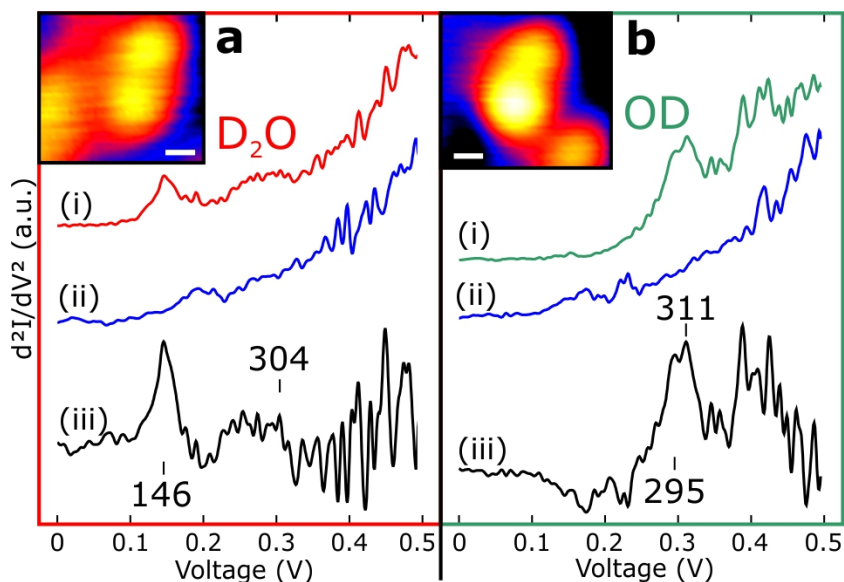


Figure 5.6: STM-IETS of D₂O and OD+D. **a**, The symmetric features in the STM topographic images shows a distinct peak at 146 mV in the inelastic tunneling spectra and a broader peak with a maximum at 304 mV. **b**, On the other hand the asymmetric feature only shows a broad peak around 295 mV with no apparent peak around 150 mV. This leads to the assignment of the symmetric (asymmetric) molecules to be D₂O (OD+D). (scalebars = 0.2 nm)

5.2.4 Energy Shift of the Stretch Modes

When we further investigate the energy range of the stretch mode, we find shifts of the energy depending if the molecule is isolated or has a neighboring molecule. We find that isolated molecules have substantially higher stretch mode energies than water molecules or hydroxyls with a neighboring molecule. This feature is shown in figure 5.7 in which we overlay the energy range of the combined symmetric and antisymmetric stretch mode for each molecule with gray.

While the maximal intensity of stretch mode energy in the case of an isolated H₂O molecule (a) and an isolated dissociated OH+H molecule (b) is around 450-500 mV, it redshifts by around 50 mV if the molecules have a neighbor (c,d). We investigated this matter in conjunction with DFT calculations. The calculations show that this shift is due to the formation of a water complex (cf. figure 5.8). This complex is formed by a hydrogen bond between a water molecule to a surface hydroxyl as indicated by the dashed black line in figure 5.8. This also explains the discrepancy we faced

5.2. Identifying Water Molecules and Hydroxyls via IETS

comparing our stretch mode data of the complexes (with hydrogen bonds) with ATR-FTIR data. Since usually coverages of close to a monolayer or even more are used, the water molecules are very likely to form these complexes redshifting the stretch mode energy. Overall, we find good agreement between our experimental values, the DFT-calculations and previously reported ATR-FTIR data (Table 5.1).

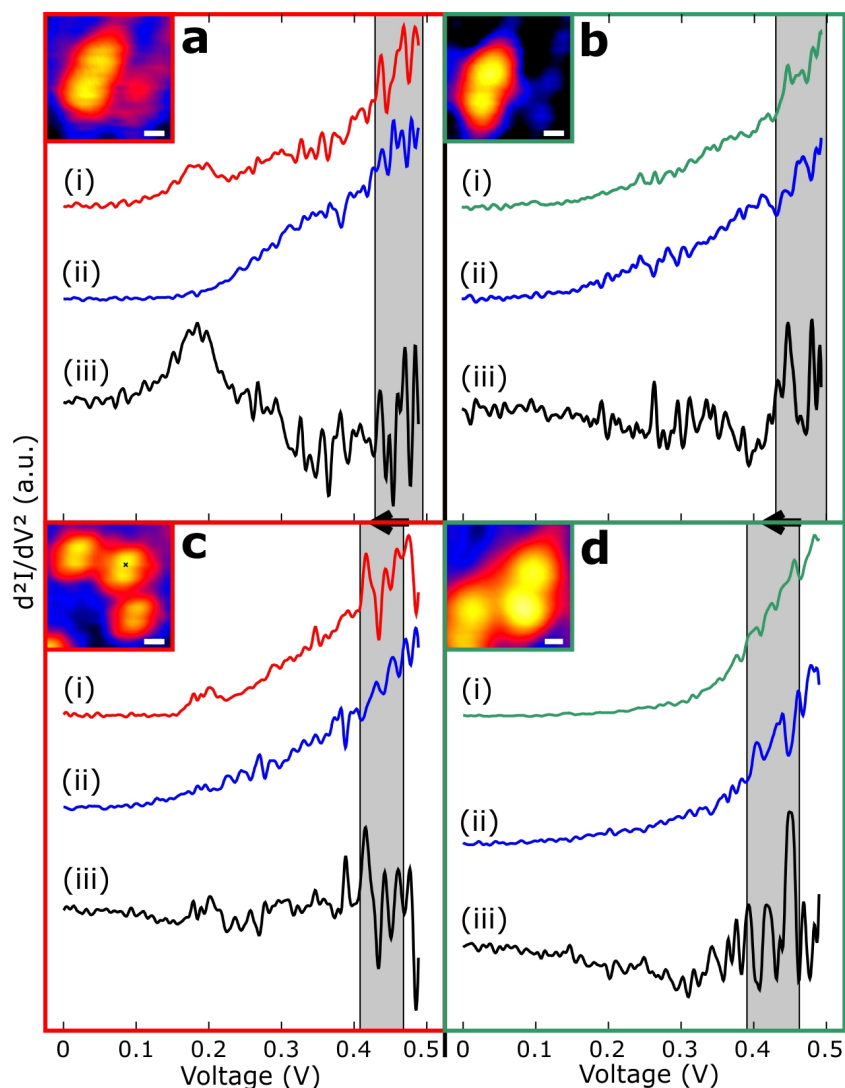


Figure 5.7: Energy shift of the stretch modes of water on TiO₂ anatase (101). **a,b**, The IETS data obtained on the isolated H₂O and OH+H molecule shows a stretch mode peak around 450-500 mV. **c,d** When these molecules are no longer isolated but have a neighboring molecule the stretch mode energy redshifts by 50 mV (indicated by black arrows) due to the formation of hydrogen bonds.

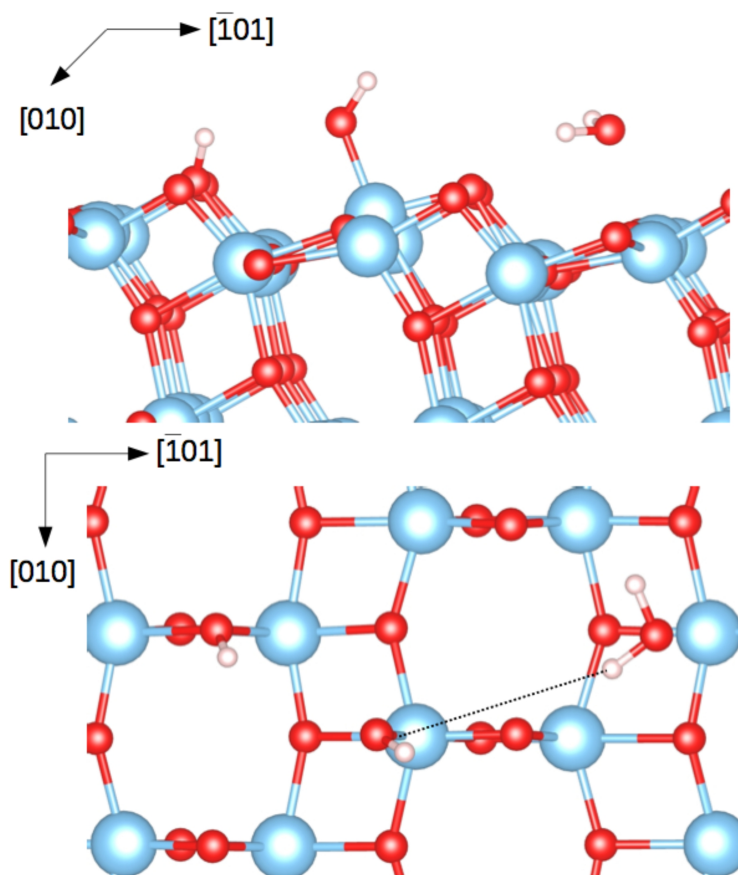


Figure 5.8: DFT atomistic model of one of the water complexes on TiO₂ Anatase(101). The water complex is formed by a hydrogen bond of a water molecule with a neighboring surface hydroxyl (dashed black line). This surface hydroxyl can originate from a dissociated water molecule (OH+H) as depicted here.

5.2.5 STM Simulations and Dissociation Barriers for Water on TiO₂ Anatase (101)

Using DFT together with the presented experimental data we simulated the adsorption model of H₂O and its dissociated form OH+H in the presence of an electric field which is generated by the STM tip. The results are shown in figure 5.9a and c, respectively. The oxygen of the H₂O molecule forms a dative bond to a surface Ti_{5c} and aligns its intrinsic electric dipole perpendicular to the surface, with the H atoms pointing upward due to the presence of the electric field. A similar effect is obtained for the hydroxyl group where the oxygen forms a covalent bond. Using these models, we were able to simulate STM images using Tersoff-Haman which is presented in figure 5.9b and d. The simulated STM image of the H₂O molecule (b) shows two round protrusions with its center on top of the Ti atom in the Ti-O dimer. The simulation

5.2. Identifying Water Molecules and Hydroxyls via IETS

Units: meV	DFT		STM-IETS		ATR-FTIR [130]	
System	bend	stretch	bend	stretch	bend	stretch
single H ₂ O	195	459, 472	191	474		
single H+OH		465, 472		447,480		
H ₂ O - (OH+H) complex						
H ₂ O	199		201		203	
H ₂ O with H bonding		404		420		399, 417
single D ₂ O	143	331, 346	146	338		
single D+OD		338, 343		327		
D ₂ O - (OD+D) complex						
D ₂ O	146		146		149	
D ₂ O with D bonding		293		304		298, 307

Table 5.1: Comparison of theoretical and experimental vibration energies of water and its dissociated form on TiO₂ anatase (101).

shows that the measured DOS features in the STM stem from the hydrogen atoms. Due to the symmetry of the water molecule also the STM topographic features are symmetric. In the case of the dissociated water molecule (OH+H) a hydrogen is split from the water molecule and binds to a surface O_{2c} atom in the vicinity. Since now the symmetry of the molecule is broken, the simulated STM image shows an asymmetric dumbbell shaped protrusion. Given the low diffusion barrier of hydrogen we also calculated STM images for hydroxyls with and without hydrogen in the vicinity; the calculated STM images of OH were not affected by the position of adjacent H. These simulations are in good agreement with our experimental results.

In given conditions, around 30 % of protrusions appeared as asymmetric protrusions indicating those molecules were dissociated without light. The occurrence of dissociated water molecules on the anatase (101) surface can be explained by the preparation procedure in which we heat up the sample to room temperature. Hence, we consider the possibility of thermal dissociation by calculating the energy diagram of the water dissociation which is shown in figure 5.10. For the dissociation to occur one hydrogen bond of the water molecule is weakened and an intermediate activated complex (ii) is formed. The activation energy of this complex is $E_a = 0.26$ eV. Following, the free hydrogen binds to a surface O_{2c} in the vicinity. The enthalpy difference ΔH between a H₂O molecule and the dissociative state (OH+H) is 0.16 eV meaning that the reaction is endothermic. However, the hydrogen atom can diffuse further (v) by overcoming a barrier of 0.44 eV blocking the reverse reaction. The diffused proton state is also less favorable by 0.17 eV due to the formation of hydrogen bonds. Overall, owing to the relatively low barrier heights, the thermal dissociation of water at room temperature is highly probable. This is also supported by temperature dependent XPS data which

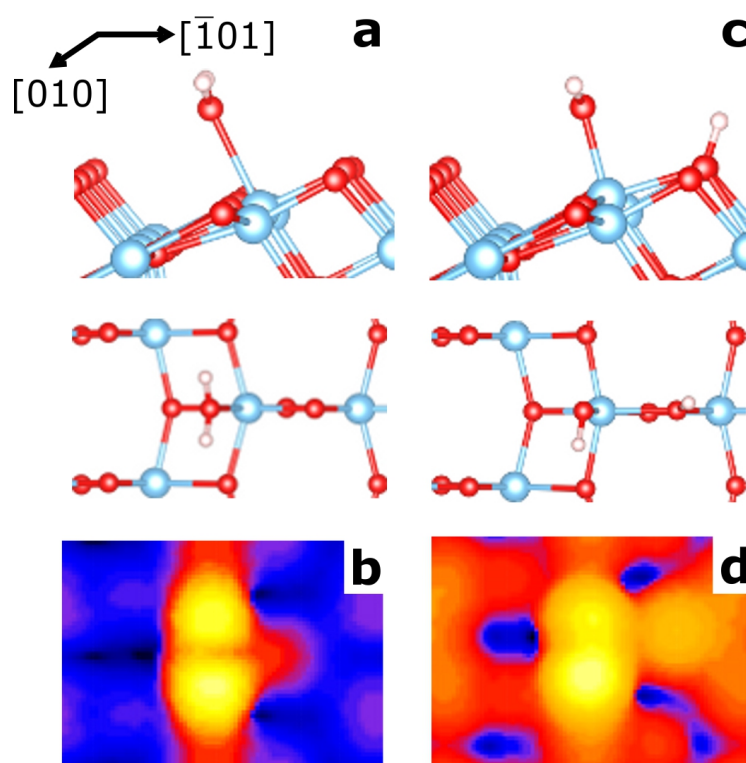


Figure 5.9: Theoretic model and DFT-based STM simulated images of water on TiO₂ anatase(101). **a**, Ball-and-stick model of H₂O adsorbed on top of a the anatase surface. The oxygen of the water molecule binds to a surface Ti_{5c} reaching away from the neighboring outermost oxygen row. **b**, DFT-based STM simulated image using the model in **a** shows a symmetric dumbbell shaped protrusion. The bright features stem from the hydrogens. **c**, For the dissociated water molecule (OH+H) again the oxygen binds to a surface Ti_{5c} reaching away from the neighboring outermost oxygen row. The leftover hydrogen goes to a surface O_{2c} in the vicinity. **d**, DFT-based STM simulated image shows that this arrangement leads to a asymmetric feature.

showed the desorption of both, molecular water and hydroxyls at room temperature [20] (XPS data is displayed in the next section 5.3.1). However, these results should be taken as a qualitative description because, as already pointed out in Ref. [19], we found that the energetics of the molecular and dissociated water is sensitive to parameters used in the calculations.

Taken together, our combined experimental and theoretical analyses allow distinguishing water molecules and hydroxyls on the semiconductor TiO₂ anatase (101) surface using chemical fingerprints, *i.e.* molecular vibrations, obtained by STM-IETS. Having single molecular chemical resolution on semiconductors opens new possibilities for fundamental energy research, especially investigating the PWS on TiO₂ anatase (101).

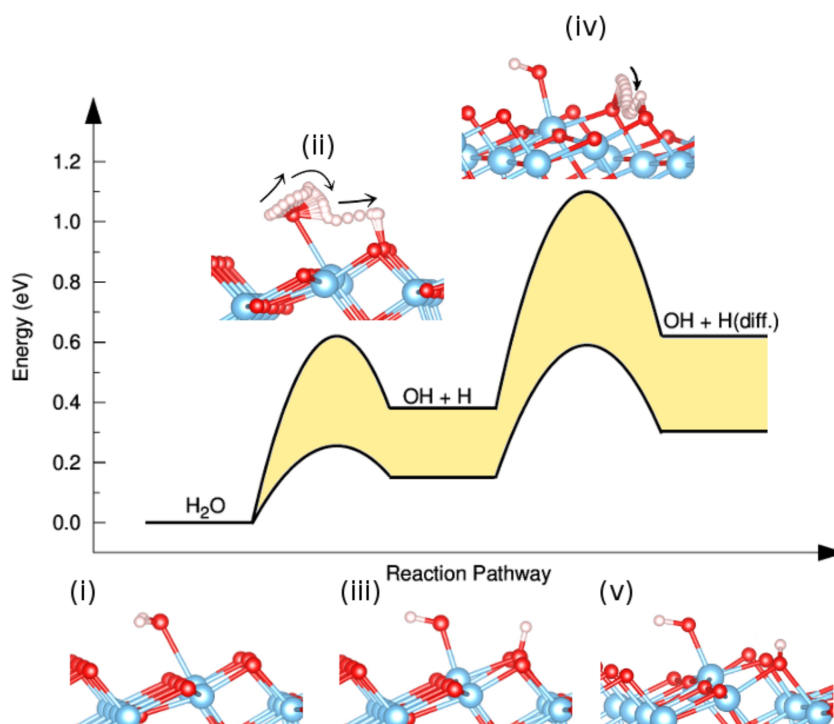


Figure 5.10: Calculated dissociation barrier for water on TiO₂ anatase (101) surface and diffusion barrier for H proton on the surface. Upper curve: reaction pathway calculated with a slab containing 4 TiO₂ layers, and by sampling the first Brillouin zone at the Gamma point. Lower curve: reaction pathway estimated from calculations of the dissociation energies between the configurations (i), (iii), and (v), using a larger slab (8 layers) and a finer (2x2x1) sampling of the Brillouin zone. In the lower curve the reaction barriers were estimated by scaling the barriers calculated in the upper curve via the ratios of the corresponding dissociation energies. The dissociation of (i) the H₂O molecule to (iii) OH + H occurs via (ii) an intermediate activated complex, for which we estimated an activation energy $E_a = 0.26$ eV. This reaction is endothermic with an enthalpy $\Delta H = +0.67$ eV. The subsequent diffusion of the H proton on the surface ((iii) to (v)) can take place by overcoming a potential barrier for which we estimate an activation energy $E_a = 0.44$ eV. The diffusion reaction is also endothermic with an enthalpy $\Delta H = +0.75$ eV.

5.3 Globally Ordered Water Monolayer on TiO₂ Anatase (101)

Water is ubiquitous in ambient atmosphere and thus, water molecules do not only adsorb isolated but rather form monolayers at higher coverages due to intermolecular interactions. Since the interaction of these water layers with the TiO₂ surface has far reaching consequences in photoelectrochemical cells [25] and PWS, a lot of research

has been dedicated to understand the adsorption state. On defect-free rutile (110) it was highly debated for a long time experimentally and theoretically if water adsorbs molecularly or dissociated [131, 132, 133, 134, 135, 136, 137, 138, 139, 140, 141]. Following, Walle *et al.* could present new experimentally decisive data showing that the first water monolayer exhibits a significant fraction of dissociated water molecules without the presence of surface defects by using highly surface sensitive photoelectron spectroscopy [142]. On the technologically more relevant anatase (101) surface this debate is still ongoing. While previous work suggested the adsorption of molecular water on the anatase surface [26, 21, 143, 126, 144], more recent work from Walle show a mixed dissociative and molecular water adsorption at 120 K on the anatase surface [20] in conjunction with recent theoretical work from C. Patrick and F. Giustino [19]. This contradiction was explained by a difference in sensitivity for the OH detection in contrast to previous XPS studies. In their paper, Walle *et al.* also related their work to previous STM studies that showed a molecular water adsorption and stated: *STM does not provide the chemical identity of adsorbates* [20].

In this section, we will discuss our investigation of the formation of water monolayers on the TiO₂ anatase (101) surface. By using different preparation techniques we are able to control the amount of water on our surface. This ultimately leads to an ordered monolayer consisting purely of H₂O molecules which is also chemically identified using STM-IETS. The findings presented here will bring new input into the discussion of water monolayer adsorption on the anatase (101) surface.

5.3.1 Preparation of Different Water Monolayers on TiO₂ Anatase (101)

A lot of work has been done to understand the temperature dependence of water adsorbed on TiO₂ anatase. TPD experiments show 3 desorption peaks at 160, 190, and 250 K which were attributed to molecular multilayer desorption, desorption of molecular water which is hydrogen bonded to surface O_{2c} and desorption of molecular water bonded to surface Ti_{5c}, respectively [21]. In rutile, an additional desorption peak was found around 500 K [145, 146], which is attributed to desorption of dissociated water molecules at VO sites. Since this additional peak is missing for water desorption on TiO₂ anatase (101), new theoretical and experimental studies suggest that the broad peak around 250 K in the TPD spectrum could be assigned to a mixed desorption of molecular and dissociated water, due to similar adsorption energies [19, 20].

Hence, in order to form water monolayers which are chemically bonded to the surface Ti_{5c} atoms, we should deposit water at a sample temperature between 190 and 250 K. However, due to the limitations of our cooling system, our samples are cooled down to 110 K using liquid nitrogen. To be still able to have a monolayer formation instead

5.3. Globally Ordered Water Monolayer on TiO₂ Anatase (101)

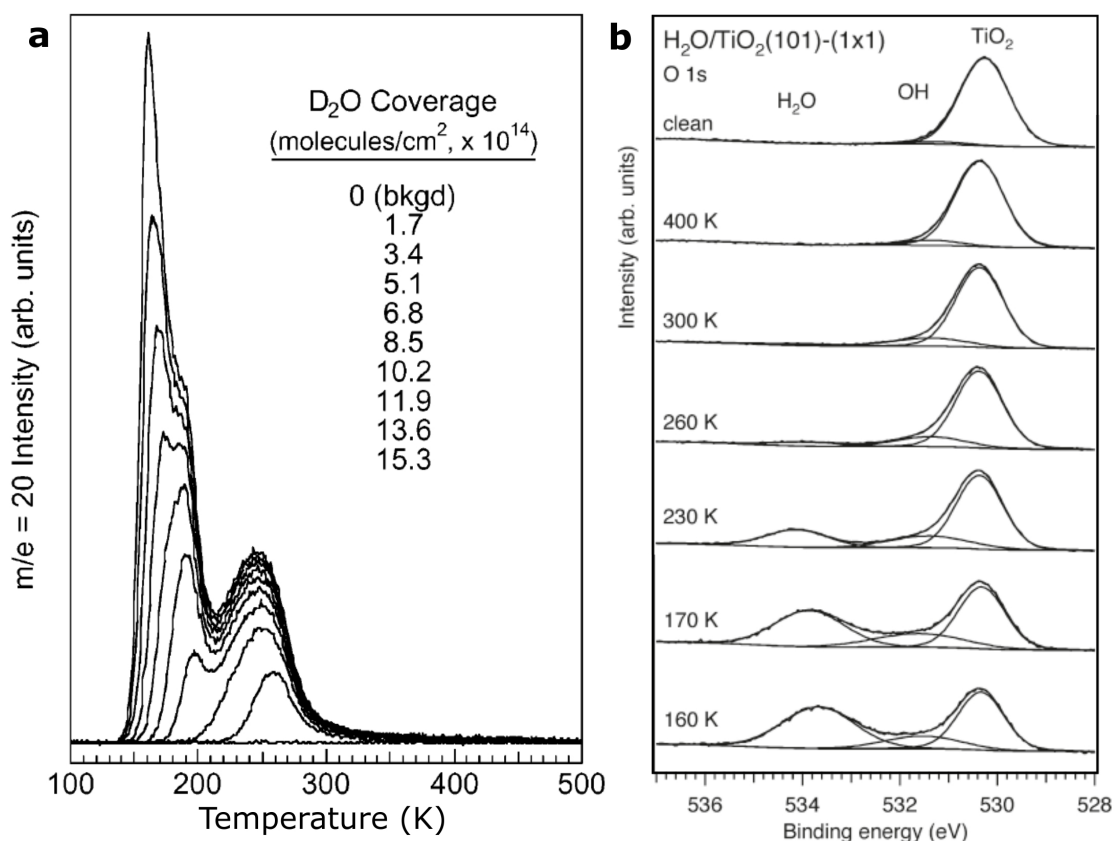


Figure 5.11: TPD and temperature dependent XPS spectra of water on TiO₂ anatase (101). **a**, TPD spectrum of D₂O on TiO₂ anatase (101) reveals 3 desorption peaks at 160, 190, and 250 K (taken from ref. [21]). **b**, Temperature dependent XPS spectra of H₂O show that even at room temperature small amounts of hydroxyls and water molecules are present on the TiO₂ anatase surface (taken from ref [20]).

of the water molecules only forming clusters, we can control a second parameter, namely the deposition flux. Although we use state of the art needle valves, the control of the flux remains challenging and has a lower limit, which we will discuss in the next sections.

Ice Formation

We prepared our TiO₂ anatase (101) crystal using the oxygen terminated treatment described earlier in section 3.1. We subsequently cooled down the sample to $T_s = 120$ K and backfilled the chamber at a pressure of 10^{-8} for 10 seconds. A STM overview image of the ice covered anatase surface is presented in figure 5.12a. Depending on the amount of ice multilayers the conductivity of the sample changes from conductive to insulating. Using a low ice coverage we can observe the typical trapezoidal shaped

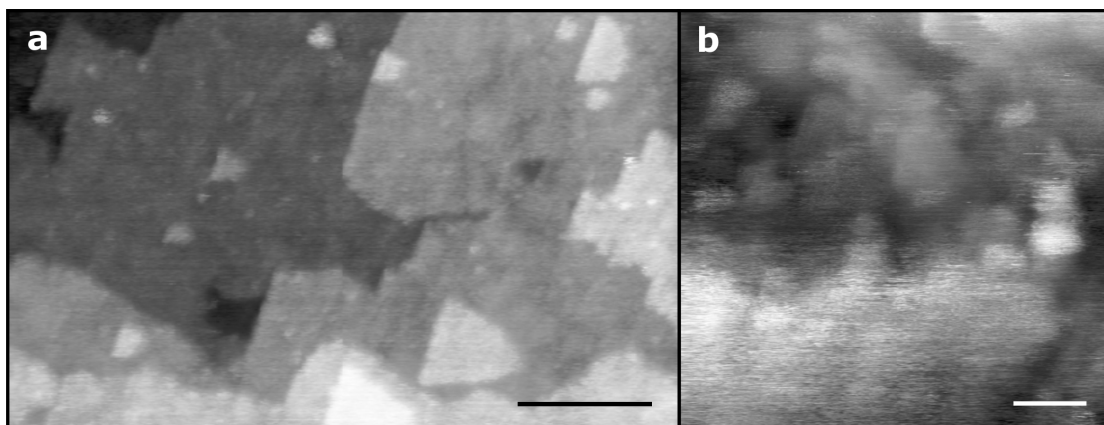


Figure 5.12: Ice formation on TiO₂ anatase (101). **a**, STM overview image of ice adsorbed on the anatase (101) surface. Although the adsorption is amorphous the trapezoidal shape islands of the anatase (101) surface can still be seen hinting towards a low coverage. **b**, Zoom-in STM topograph reveals physisorbed ice. (scalebars: **a** = 20 nm, **b** = 5 nm)

islands with step edges along the crystallographic [010], [-111], and [11-1] directions. Taking a closer look at the surface (cf. zoom-in in figure 5.12b) more and more tip instabilities show as fuzzy lines in the image due to physisorbed ice which is only bound by van der Waals interactions to the ice monolayer. Since this interaction is weak the electric field of the tip is enough to move these molecule over the surface resulting in horizontal lines. We tried performing STS and IETS on these ice layers investigating the electronic structure which was challenging due to tip instabilities.

5.3.2 Water Monolayer

As described before, to achieve water monolayers on the surface we reduce the flux so that the molecules have more time to rearrange on surfaces and to form ordered structures. When we reduced the flux in our water deposition by reducing the pressure of the backfilled chamber to $7.5 \cdot 10^{-10}$ mbar for 5 minutes, we were able to create a submonolayer coverage of water on the TiO₂ anatase (101) surface as presented in figure 5.13a. Although there are still physisorbed water molecules and ice clusters present, we were able to image clearly an ordered water layer which can be seen in figure 5.13b. The structure of this layer will be discussed later in this section.

Since there were still physisorbed water molecules present that influenced the tip stability, we tried to improve the quality of our monolayer by further reducing the flux. This was challenging, since the needle valve, as stated before, has a lower flux limit. Hence, we pursued a different approach to deposit low amounts of water on the TiO₂ anatase (101) surface. Due to all of our water depositions and subsequent transfers

5.3. Globally Ordered Water Monolayer on TiO₂ Anatase (101)

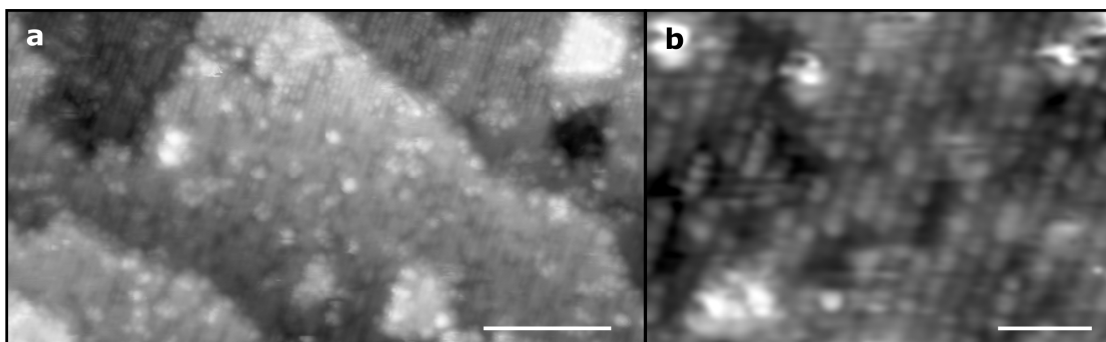


Figure 5.13: Formation of a water monolayer on TiO₂ anatase (101) using water deposition. **a**, STM image shows a submonolayer coverage of water adsorbed on TiO₂ anatase (101) using backfilling the preparation chamber with a pressure of $7.5 \cdot 10^{-10}$ mbar for 5 minutes. This results also in the adsorption of physisorbed water (**b**). (scalebars: **a** = 10 nm, **b** = 2 nm)

into our STM, water molecules were trapped on the walls of our cryogenic STM chamber which is cooled to 5 K. We let the STM cryostat warm up to the temperature of our outer liquid nitrogen shield (77 K) for 24 hours. Following, we cooled down the system again to 5 K by refilling our inner cryostat with liquid helium. This procedure lead to a nearly perfect monolayer coverage of water molecules on the anatase (101) surface as shown in figure 5.14a. Additional to the monolayer adsorption, ice cluster are formed (blue circle) with a size between 1-2 nm. These ice clusters form preferentially on the different high- and low-reactive step edges but also can be found on top of the water monolayer.

High-resolution STM images combined with linescans in different crystallographic directions (cf. figure 5.14b and c) reveal that the monolayer adsorbs along the [010] direction since the amplitude of the oscillations in the linescans is the lowest along this direction. If we compare the lattice parameter of the water monolayer with the one of the underlying TiO₂ anatase (101) substrate, we find that the parameters are the same meaning that one round protrusion in the water monolayer corresponds exactly to one Ti-O pair along the [010] and the [11-1] crystallographic direction (3.8 and 5.5Å, respectively). The monolayer also inhabits defects, which we attribute to either missing or wrongly incorporated H₂O molecules. Figure 5.14d depicts a [010] step edge. Since this step edge presents a low-reactive surface defect, the water monolayer formation is hindered at the edge. It is interesting to note that the clusters and water molecules adsorbed in the vicinity of the low-reactive step edge are not stable when the tip is scanning resulting in fuzzy images. On the high-reactive step edges which are decorated by VOs, this effect is not present. Hence, the vacancies stabilize the binding of the water molecules or clusters while the stoichiometric step edge presents a surrounding in which the energy barrier between at least two binding states is low

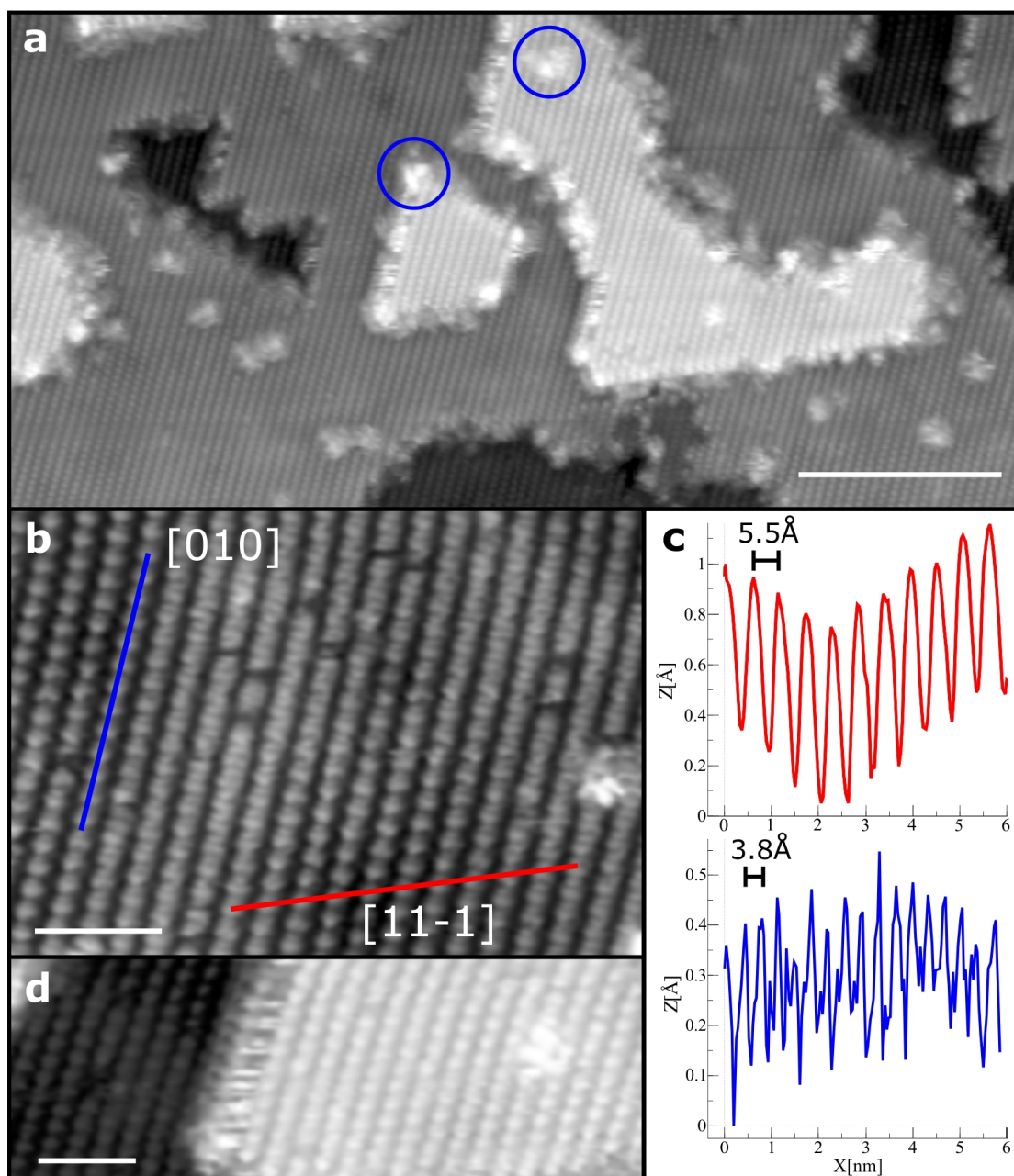


Figure 5.14: Formation of a water monolayer on TiO₂ anatase (101) using the STM chamber. **a**, STM image after using desorption of water from our STM cryostat by heating up to liquid nitrogen temperature (77 K). This leads to formation of a nearly perfect **(b)** monolayer of water on the anatase surface. **c**, Performing linescans in different crystallographic directions ([010] and [11-1]) reveal that the monolayer is adsorbed along the [010] direction. **d**, The instability of the [010] step edge can be explained by not incorporated water molecules that change the adsorption due to the electric field of the scanning tip. (scalebars: **a** = 10 nm, **b,d** = 2 nm)

5.3. Globally Ordered Water Monolayer on TiO₂ Anatase (101)

enough to be overcome by the tip-induced electric field.

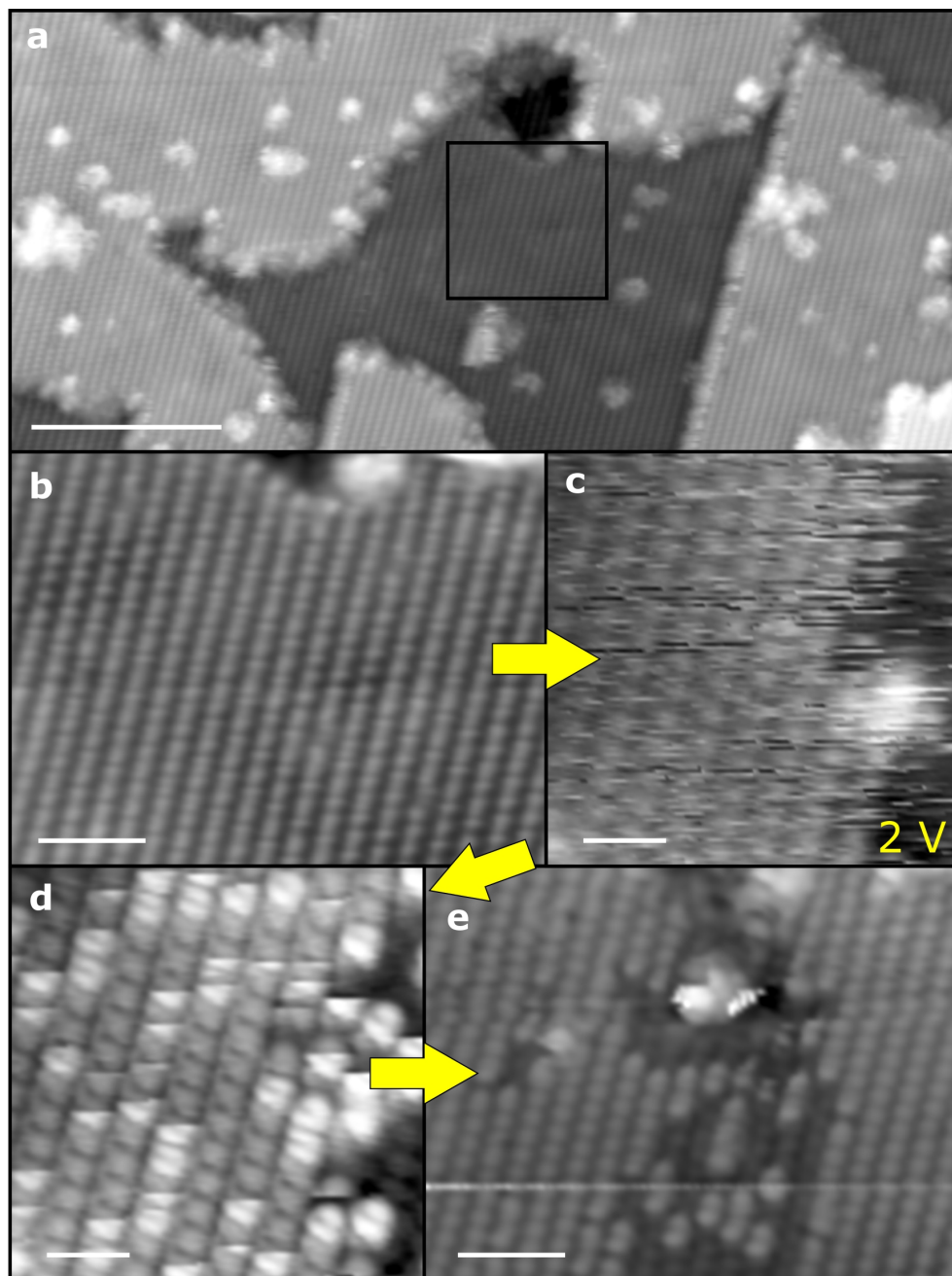


Figure 5.15: Influence of high electric fields to the water monolayer. **a,b**, STM topograph of the water monolayer before scanning with high bias voltages in the black squared area. **c**, Scanning at increased bias voltages (2 V, $I_{\text{set}} = 0.1\text{-}1$ nA) lead to an instable STM image. After transforming molecules into an intermediate activated stage (**d**), water molecules are removed from the surface (**e**). (scalebars: **a** = 10 nm, **b,e** = 2 nm, **c,d** = 1 nm)

The study of desorption of molecules from surfaces using tip-induced electrons in STM is an active research area. Having a better fundamental understanding of the desorption allows the tailoring of surface reactions. This technique has been used to characterize hydrogen desorption from Si (100) [42] but also from TiO₂ rutile (110) [147]. In general, electron-induced effects can lead to desorption of a chemisorbed molecule if the energy of the tunneling electron is high enough to fill the antibonding state and thus, break the bond between the molecule and the surface. This can be enhanced if the electron tunnels inelastically and thereby vibrationally heats the molecule. We were also able to desorb some of the water molecules using high electric fields either by tip pulsing (3 V, 20 ms, $I_{\text{set}} = 0.1-1$ nA) or scanning at high voltage biases (2 V, $I_{\text{set}} = 0.1-1$ nA) which can be seen in figure 5.15. The black square in figure 5.15a marks the area before we scanned with high bias voltage showing a monolayer coverage of water (cf. figure 5.15b). After scanning this area with increased bias voltage (figure 5.15c) the water molecules transform into an intermediate activated state (d) until water molecules are removed (e). This activation and removal only occurred at bias voltages above 1.5 V and we assume that already this energy is enough to transfer electrons into the H₂O-surface Ti_{5c} antibonding state to break the bond and remove the water molecules most likely to adsorb on the tip. The success rate for the desorption in the scanned area was around 50%. Due to the removal of some water we were now able to characterize isolated and in the monolayer incorporated water molecules.

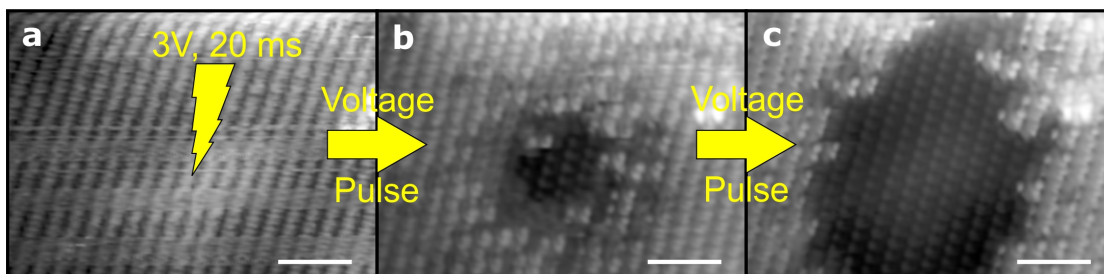


Figure 5.16: Influence of tip pulses to the water monolayer. **a**, STM topograph showing the water monolayer. **b**, After applying a high energy pulse (3 V, 20 ms) the substrate is subsequently cleaned. **c**, Applying multiple pulses increases the clean substrate area. (scalebars: **a-c** = 2 nm)

As described earlier, we were also able to clean the substrate and remove water molecules from the monolayer by using tip pulses of 3 V, which can be seen in figure 5.16. To control the amount of clean substrate area, we can apply multiple pulses in the same position (cf. 5.16b and c). This artificial area cleaning was important throughout this experiment to be able to characterize and prepare our tip using STS and voltage pulses on the substrate.

The Water Monolayer Structure

Taking a closer look at the water molecules we find three different appearances which are shown in figure 5.17. The blue encircled water molecule is isolated and appears as a symmetric dumbbell shape protrusion as presented earlier in this chapter (cf. figure 5.17b and c). The height of the molecule obtained using a linescan over the molecule is 1.5 nm and the size around 0.8 nm. The black encircled molecules (figure 5.17d and e) present a dimer formation of water molecules. Due to steric hindrance between the two molecules when adsorbed next to each other the appearance changes showing a lower DOS in the center part and a higher DOS at the edges of the dimer. Interestingly, we also see this behaviour in a molecule which is not completely incorporated into the monolayer (green circle). While the molecule adsorbed fully in the monolayer structure has two nearest neighbors along the [010] direction, the lower molecule (green) misses one beneath. Hence, the molecule appears asymmetric with a higher DOS at its lower part. Furthermore, the extension of the DOS of this molecule (green) is significantly decreased compared to the isolated water molecule (blue) which can be seen in the linescan in figure 5.17e. Taken together, this allows us the assignment of a single round feature with 0.3 nm in size (figure 5.17f and g, red) in the monolayer to be a water molecule.

We functionalized our tip by picking up an individual water molecule, which is shown in figure 5.18a, to investigate our proposed idea further. Due to the functionalization, the extension of the isolated water molecules (blue) is reduced to 0.5 nm which can be seen in figure 5.18b and c. Interestingly, it enables the detection of a substructure for the molecules forming dimers (black, figure 5.18d and e) as well as for the molecules in the monolayer (red, figure 5.18f and g). For the water dimer the substructure looks as follows: round feature at its ends and a contracted oval shape in the center. Furthermore, instead of appearing in a single round protrusion, the water molecules in the monolayer appear now in a contracted dumbbell shape consisting of two oval shaped protrusions. The size of this protrusion is with 0.35 nm similar to the size when measured without a functionalized tip.

Using the findings above, we try to determine the lattice positions of the water monolayer by overlaying the lattice of the TiO₂ anatase (101) surface which is shown in figure 5.19a. Again the single isolated water molecule binds with its oxygen on top of a surface Ti_{5c} atom resulting in a symmetric dumbbell shaped protrusion as shown in figure 5.19b. For the dimer (figure 5.19c) and monolayer formation (figure 5.19d) along the [010] direction the oxygen of one water molecule still binds to a surface Ti_{5c} atom, however, due to the steric hindrance induced by an additional water molecule the water molecule rearranges leading to a change in the imaged DOS. For this we turn to DFT calculations which will be discussed later in this section.

To investigate the suggestion of a mixed molecular and dissociated water monolayer

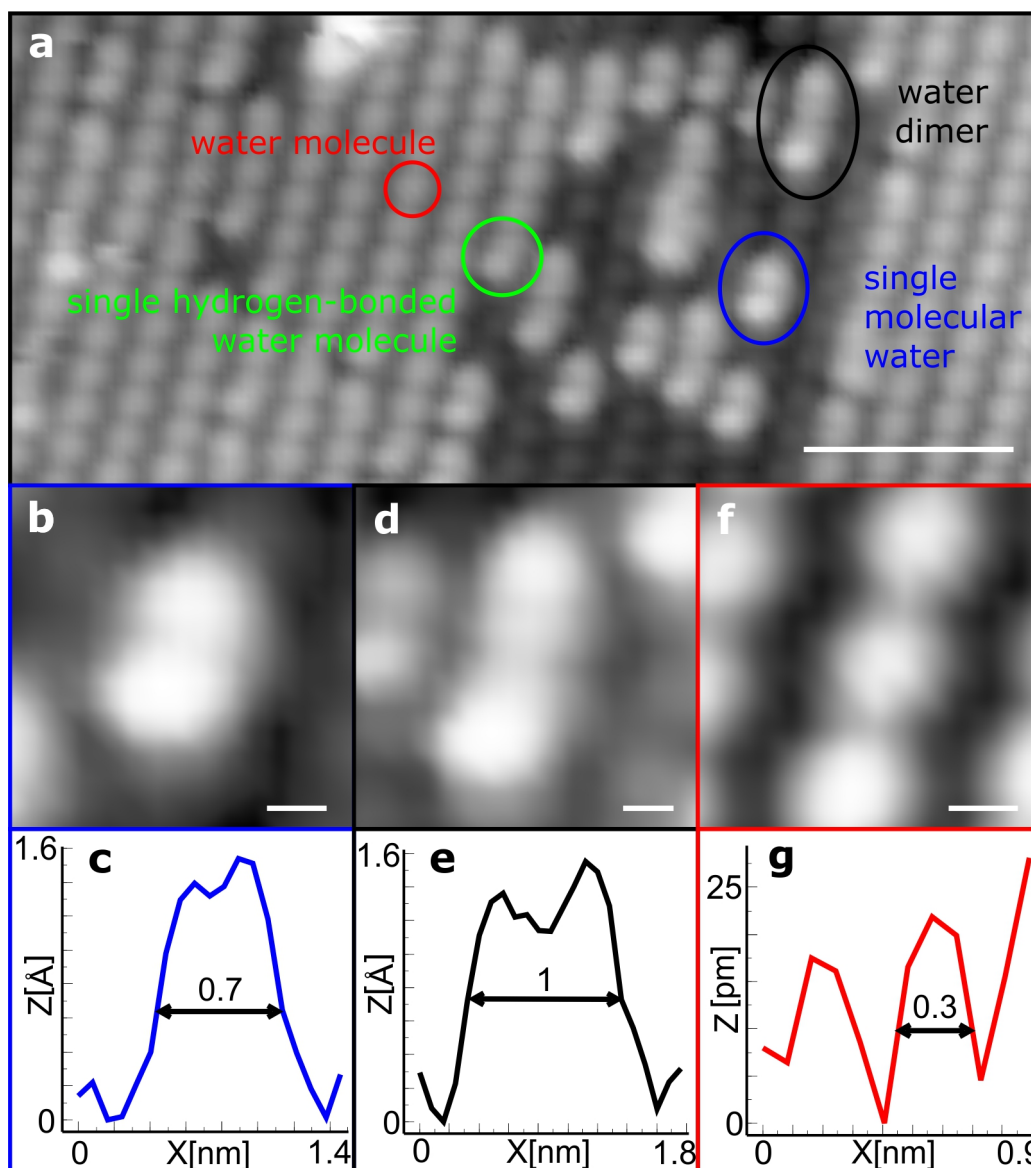


Figure 5.17: Different molecular water adsorptions on TiO₂ anatase (101). **a**, High-resolution STM image of the water monolayer with a small clean substrate patch. Water molecules can adsorb isolated (blue), with a single neighbor along the [010] direction (water dimer, black; water molecule in the monolayer, green) or with two neighbors (red). **b,c**, The isolated dumbbell shaped protrusions are symmetric with a size of 0.8 nm similar to the previous chapter (blue circle). If a water dimer is formed ((**d,e**), black circle) the individual molecular dumbbell features transform into singly asymmetric features which can also be seen at the not yet fully in the monolayer incorporated molecule in the green circle. Hence, we conclude that when fully incorporated into the monolayer each water molecule correspond to exactly one round feature ((**f,g**), red circle). (scalebars: **a** = 2 nm, **b,d,f** = 2 Å)

5.3. Globally Ordered Water Monolayer on TiO₂ Anatase (101)

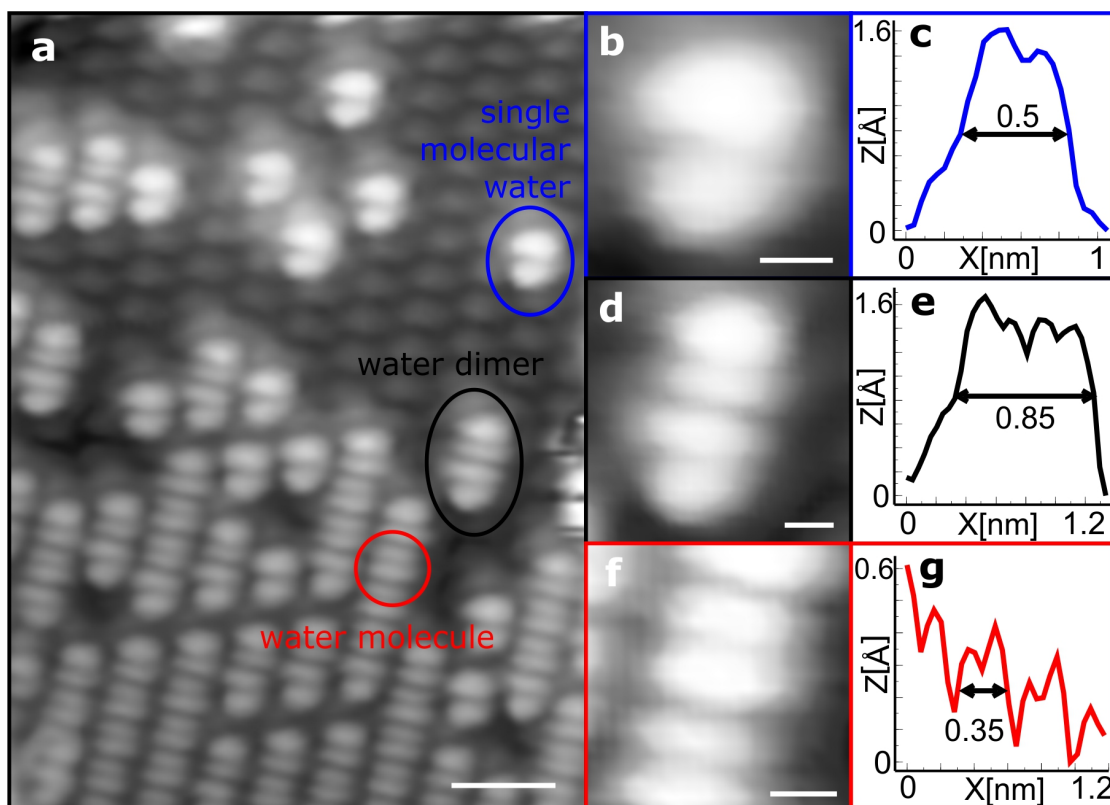


Figure 5.18: Different molecular water adsorptions on TiO₂ anatase (101) using a functionalized tip. **a**, High-resolution STM image of the water monolayer with a small clean substrate patch using a functionalized tip. **b,c**, Due to the functionalization, the isolated dumbbell shaped protrusions is slightly asymmetric and reduced in size to 0.5 nm. **d,e**, Also the water dimer shows a substructure with a round feature at its ends and a contracted oval shape in the center. **f,g**, When the water molecules have two neighbors in the water monolayer the dumbbell shape transforms into two oval shape protrusions supporting the assignment of the monolayer to consist purely out of H₂O. (scalebars: **a** = 2 nm, **b,d,f** = 2 Å)

adsorption on TiO₂ anatase (101), we performed STM-IETS. We find clear indications of water being present using the IETS features already described in the previous section. In figure 5.20 we performed STM-IETS on a water molecule incorporated in the monolayer (i) and on a clean substrate patch (ii). The difference spectrum (iii) between the water molecule and the substrate shows a strong feature around 215 mV and a broader one in the area around 435 mV which is in good agreement with the bending and stretching modes for water molecules with a neighboring one as presented in the previous section. In general, performing STM-IETS on the monolayer was more challenging due to tip instabilities. This lead in some cases to an appearance of an additional peak around 300 mV, which we cannot clearly assign. However, we find the

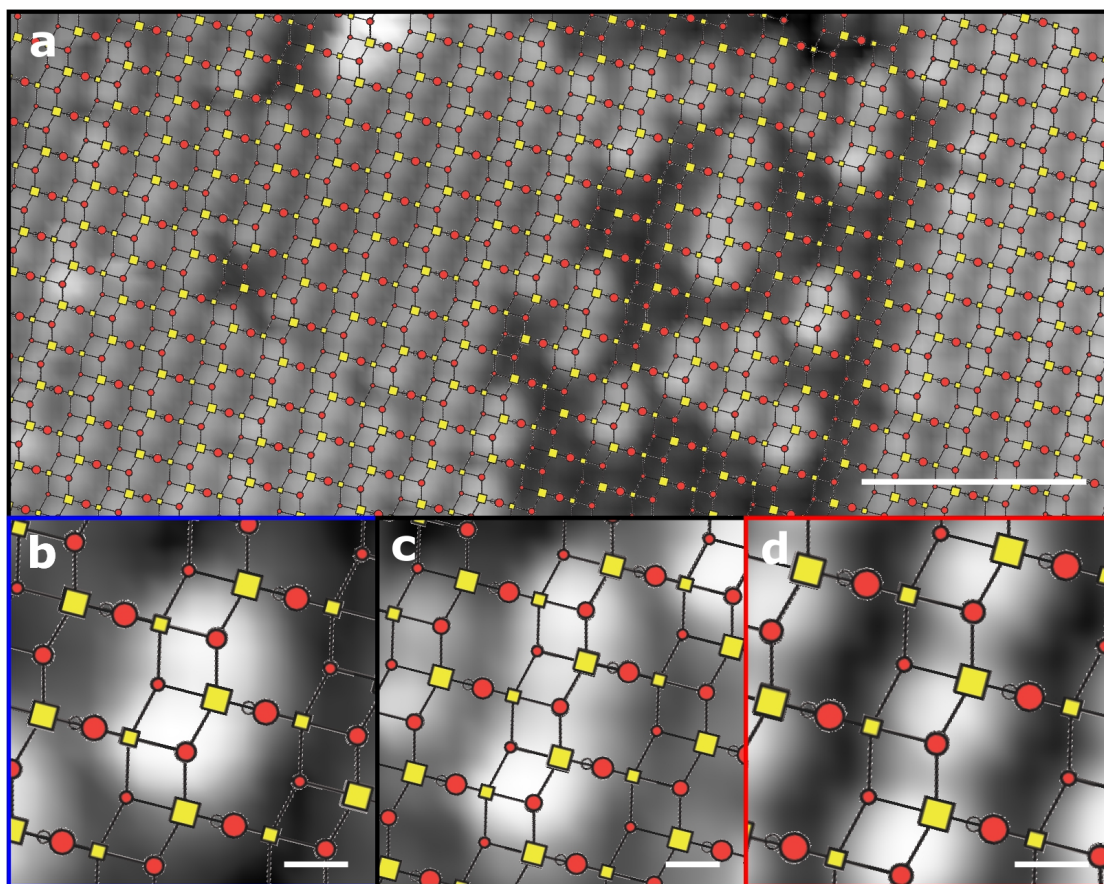


Figure 5.19: Determining the structure of water monolayer on TiO₂ anatase (101). **a**, High-resolution STM image of the water monolayer overlaid with the anatase (101) surface lattice (yellow = Ti, red = O). **b**, The isolated dumbbell shaped protrusion binds with its center (oxygen) on top of a surface Ti_{5c} atom. **c,d**, Lattice positions of a water dimer and water molecules in the monolayer. (scalebars: **a** = 2 nm, **b-d** = 2 Å)

bending mode independent of the position of the water molecules in the monolayer. Whenever we removed molecules from the substrate by tip pulsing or scanning at high bias voltages as described before, we ended up with single isolated molecules that showed the same features as the isolated water molecules in the previous section when investigated by STM-IETS. These results allow us to identify the molecules as H₂O and to conclude that the monolayer only consists of pure water.

As described in the introduction to this section, the adsorption structure of the first water monolayer on TiO₂ anatase (101) has been also subject in a recent theoretical study by Patrick and Giustino [19]. In their study two possible monolayer structures were proposed: (i) By reverse engineering XPS data obtained by Walle *et al.* [20], a mix of molecular and dissociated water which ball-and-stick model was proposed and is shown in figure 5.21b. (ii) A 1 × 1 periodic water layer only consisting of molecular

5.3. Globally Ordered Water Monolayer on TiO₂ Anatase (101)

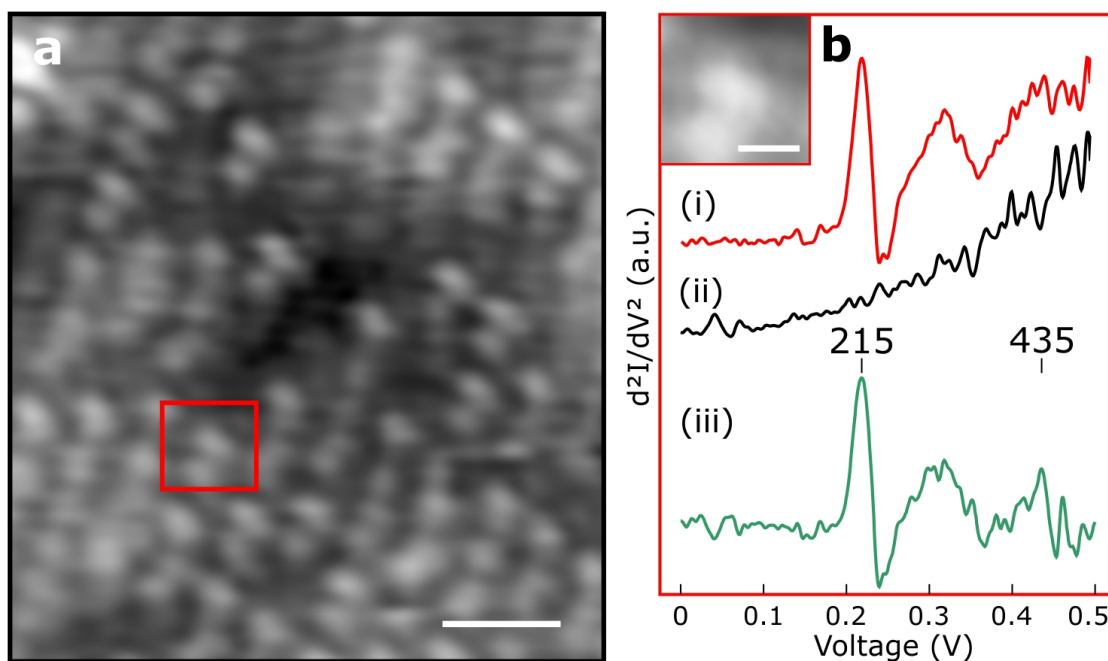


Figure 5.20: STM-IETS on the water monolayer on TiO₂ anatase (101). STM-IETS performed on water molecules incorporated into the monolayer with hydrogen bonds **a** show strong evidence of water vibrational modes ($\delta(\text{H-O-H})$ bending = 215 mV, hydrogen bonded $\nu(\text{O-H})$ stretch = 435 mV) in agreement with the values we presented in the previous section.

water which is presented in figure 5.21c. For both structures also DFT-based simulated STM images were shown. By comparing the simulated STM images with our experimental findings, we find that the mix molecular and dissociated water structure seems not to agree, since in our case the molecules do not seem to have an interrow connection or asymmetries. Additionally, the position of the highest LDOS do not seem to follow the same substructure as the one experimentally observed. Note that in this experiment the sample was always kept at low temperatures (< 110 K) so that the molecules might not receive enough thermal energy to dissociate in contrast to the work of Walle *et al.*, where the deposition was done at 120 K and subsequently heated to 160 K [20]. The pure molecular water structure (5.21c) seems to fit better with our experimental data, since the DOS seems to be in rows following the [010] crystallographic direction of the anatase (101) lattice. Furthermore, the features are single round protrusions which correspond to exactly one water molecule which is similar to our findings. Still, the row of round protrusions in the simulated STM images are positioned in between the surface Ti_{5c} atoms in contrast to our finding of these features to appear closer to the surface Ti_{5c} atoms. Based on our STM and IETS results, we propose the structure presented in 5.21d which is similar to the one proposed in c but shifted.

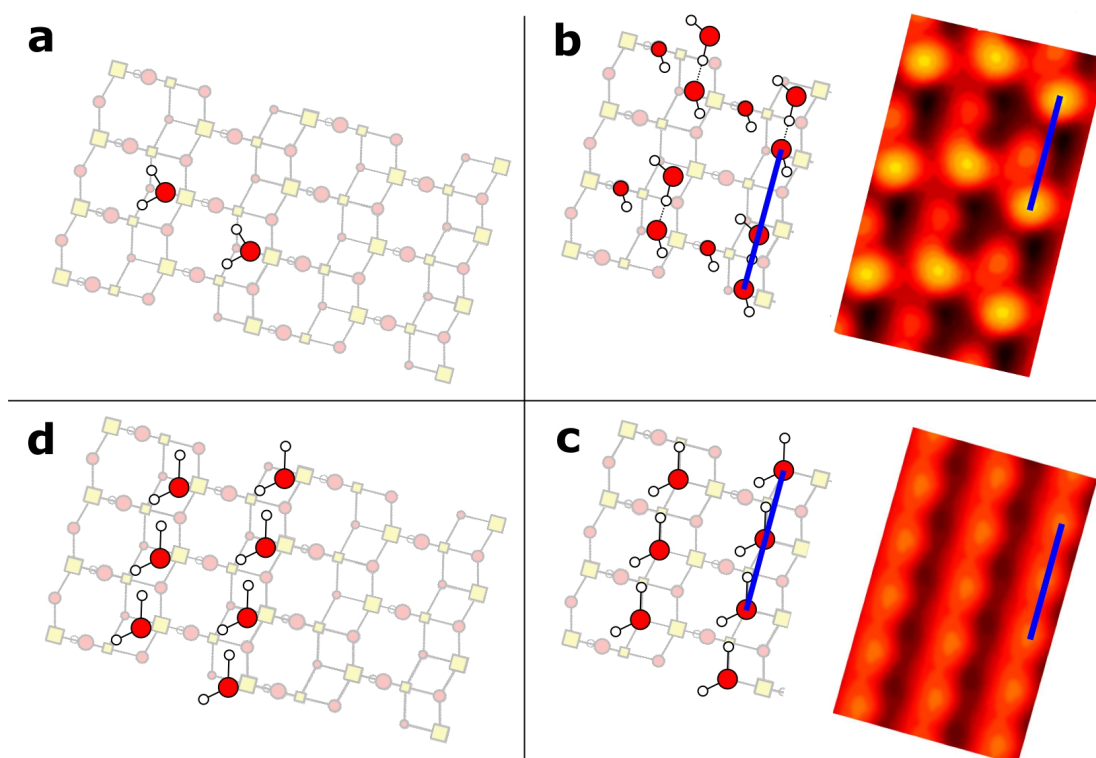


Figure 5.21: Proposed models of the water monolayer on TiO₂ anatase (101). **a**, Theoretical model of isolated water molecules adsorbed on the TiO₂ anatase (101) surface. **b**, Proposed model of a mixed molecular and dissociated water monolayer. The DFT-based simulated STM image reveals a substructure different to our experimental findings. **c**, Proposed model of a pure molecular water monolayer. The simulated STM image shows a more uniform contrast similar to our results but the adsorption sites of the rows are shifted. Hence, we propose the model presented in **d**. (**b,c**, taken from Ref. [19]).

In summary, we found an unprecedented ordered monolayer of only H₂O molecules on TiO₂ anatase (101) using STM in combination with DFT and tunneling spectra techniques. This monolayer adsorbs uniformly in a 1 × 1 structure, although still more calculations and experiments have to be done. The further study of this ordered monolayer will be of importance to shed light into water adsorption on TiO₂ anatase (101).

5.4 Conclusion

We have shown in this chapter that STM in combination with IETS can be used to obtain vibrational fingerprints of molecular and dissociated water molecules on

the semiconductor TiO₂ anatase (101). These vibrational fingerprints were used to determine and distinguish the individual species on the anatase surface. This is of critical importance to be able to study on the atomic scale the photocatalytic water splitting reaction of individual molecules to enhance future TiO₂-based devices. For the first time, it is possible to undoubtedly distinguish the individual components of a water splitting reaction on the anatase (101) surface. Hence, the reaction dynamic and pathway that have been controversially discussed in the past can now be studied in a direct method, which we will further discuss in chapter 6. Furthermore, the benefits of STM-IETS can be shared in various studies of chemical reactions at semiconducting interfaces, which aim to understand heterogeneous catalysis (CO₂ and NO₂ reduction), semiconductor device fabrication, fuel cells, and self-assembled monolayers.

Also we used STM in combination with IETS to study behavior of water monolayers on TiO₂ anatase (101) which could be created using two different approaches. The finding of a globally ordered water monolayer consisting purely of H₂O molecules is of paramount importance to understand the fundamental water adsorption on TiO₂ anatase (101). Since dissociation occurs at slightly higher temperatures than used here during preparation, this work is also important to understand water splitting.

6 Conclusions and Perspectives

In the following chapter we will discuss the conclusions that can be drawn from this work and follow-up with possible future projects in this area of research.

6.1 Conclusions

In conclusion, this work presented a clearer understanding on the fundamental level using STM about surface engineering of TiO₂ anatase (101) and the interaction of water with this substrate. The conceptual ideas and findings about creating a surface with increased or reduced reactivity in the first part of this work are very interesting for various fields in which TiO₂-based devices are already commercially available. Throughout the first part of this thesis, we presented the importance of VOs and how these vacancies are the origin of the high reactivity of the step edges. Due to the tendency of VOs to migrate into the subsurface layers of TiO₂ anatase crystals, step edges represent one of the few possible strategies to trap those vacancies at the surface where the catalytic reactions take place but not modifying the bulk properties. The VOs also result in the filling up of the Ti 3d bands creating gap states and thus, significantly reducing the bandgap to the visible. Not only is this the first time to understand the origin but also it allows to improve devices using different simple surface preparation methods creating highly stepped surfaces.

Another way to trap the high reactive VOs on the surface is the formation of the oxygen deficient titanium-terminated surface phase. This surface phase can cover up to 70% of a monolayer substantially increasing the area and amount of VOs on the surface. Hence, a larger surface area benefits of the VOs but the bulk properties remain the same.

On the other side the reduction of the surface reactivity, the so-called passivation,

is of high interest to sensing applications for devices that need to remain stable on longer timescales. Thus, simple preparation methods that can passivate the substrate in a cheap and easy manner are wanted. In section 4.1 we presented a surface passivation creating a novel oxygen network on top of the TiO₂ anatase (101) crystal. This oxygen network was created using excessive oxygen at elevated temperatures during the preparation procedure which ultimately lead to the network formation. These networks grow by incorporating adsorbed molecular oxygen species on the surface. The low amount of molecules adsorbed on top of the network compared to the amount of adsorbates on the clean anatase substrate hinted already to a reduced surface reactivity. Furthermore, the excess oxygen attaches to the VOs at the high reactive step edges reducing the reactivity of the surface even further.

Summarizing this first part of the work, we can increase the reactivity by reducing the overall oxygen content creating VOs or reduce the reactivity doing the reverse. This opens a large playground, which we will introduce in the next section. Moreover, these results are not limited to the metal oxide TiO₂ but could potentially also be applied to other metal oxides such as WO₃ or SrTiO₃ for which the role of VOs is not yet well understood [148, 149, 150].

The second part of this thesis presented the results about the interaction of water on the TiO₂ anatase (101) surface. The study of single water molecules on the TiO₂ anatase (101) surface is generally obstructed by a lack of a clear chemical identification technique on the atomic scale. Without a clear identification of the individual species on the anatase surface, studies of PWS cannot be done on the single molecular level. To circumvent this, we presented the use of STM-IETS to label individual molecular and dissociated water molecules on the anatase (101) surface. With this information reliable and consistent future studies about single molecular PWS, as partly presented in the next section 6.2, will be possible for the first time. Since this technique is not restricted to water alone but can also be used for various molecules on different semiconductors, fundamental studies on individual reaction mechanisms such as CO₂ reduction, which is an important industrial and environmental gas, will have a bright future.

Since water in ambient atmosphere also adsorbs in multilayers, the finding of a well-ordered monolayer purely consisting of H₂O molecules on the TiO₂ anatase surface is an important step towards understanding water adsorption on TiO₂ anatase (101). So far, the adsorption is strongly debated as we highlighted in section 5.3.2. With our findings, there is the chance to finally reach a conclusive picture, which is of critical importance to all TiO₂-based devices.

6.2 Perspectives

6.2.1 Further Understanding of the Water Interaction on TiO_2

A further investigation of the ice layers is interesting also in context of environmental science. Environmental scientists have recently suggested to inject aerosol particles into the stratosphere (10-50 km height) to manage solar-radiation (SRM) onto the earth [151]. The idea behind SRM is to reduce the amount of incoming sunlight onto earth thus reducing global warming. This can be achieved by injecting particles either to increase absorption in the stratosphere or to reflect the incoming sun light. TiO_2 has been recently mentioned to be a promising candidate to enhance sun light reflection due to its high refractive index [152]. However, the interaction and impact of TiO_2 nanoparticles within the stratosphere are not yet fully understood [153]. Since the temperatures in the stratosphere range from 220-270 K, the ubiquitous water typically adsorbs as ice on the surface of these nanoparticles. Hence, the understanding of the interaction of ice layers on TiO_2 anatase (101) is of critical importance to realize the idea of SRM. We also found ice clusters (blue circles) of sizes between 1-2 nm when we prepared the ice overlayers as shown in figure 6.1. The study of these ice overlayers will be important to understand the formation of ice on the TiO_2 particles in the stratosphere and hence, estimate the absorption or reflection properties to predict the amount of blocked sun light onto the earth surface.

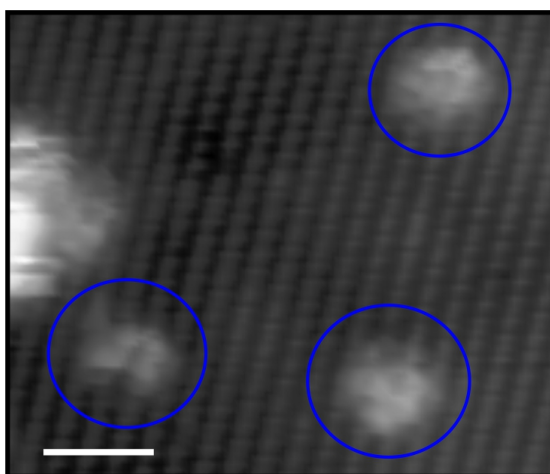


Figure 6.1: STM image of ice clusters on the TiO_2 anatase (101) surface. (scalebar = 2 nm).

As described before, the discovery of surface modifications enhancing or reducing

the overall reactivity of the surface invite to a lot of future studies. In the case of PWS on TiO_2 the single molecular adsorption on the different phases is of strong interest. Using the titanium-terminated surface phase, which has a high VO concentration, the adsorption of water molecules is especially interesting. On rutile (110) it has been shown using STM that VOs can act as defect-mediated dissociation sites for water molecules healing out defect sites [154]. It would be interesting to study how the titanium-terminated surface phase would be influenced by individual water adsorption using STM-IETS. Since the reactivity is increased on this surface termination, it is likely that we could find more thermally dissociated water molecules on this phase compared to the oxygen terminated one. This could be one prove that forming the titanium-terminated surface phase increases the water splitting efficiency.

Another interesting experiment would be recreating the parameters we used to create the pure H_2O monolayer on the different reactive surfaces. These studies could show the influence of VOs on the surface and/or in subsurface layers to the formation of a single or multiple water monolayers. Additionally, the passivation of the surface by oxygen networks could be shown. Since the oxygen network and the titanium-terminated surface phase can coexist with the pristin oxygen-terminated surface, reference measurements could be easily taken. Also, the STM can be gradually warmed to liquid nitrogen temperature (77 K) or even to room temperature, which allows a temperature dependent measurement on the order of the monolayer. In summary, the finding of a pure H_2O monolayer on TiO_2 anatase (101) presents an interesting start point for a lot of future temperature-, energy- and light-dependent studies to further understand the water interaction with the anatase surface.

6.2.2 Investigating Photoinduced Effects using the Lasersystem

Our work presented in section 5.3.2 marks an important step towards understanding the water adsorption on TiO_2 anatase (101). Due to the introduction of a laser to our system as described in section 2.3.4, we can investigate the behavior of water monolayers on the different reactive surface phases of TiO_2 anatase (101) when irradiated by UV-light. Since our laser system is equipped with different wavelengths, these measurements can also be performed varying the photon energy giving rise to additional information.

Another interesting effect is the superhydrophilicity of TiO_2 thin films which was found in 1997 by Watanabe and co-workers [155] and initiated the development of a new research field using TiO_2 thin film coatings at room temperature. The effect allows water adsorbed on TiO_2 thin films to spread out under UV-illumination. Although the amphilic behaviour of TiO_2 films has been studied extensively, the origin of this

effect remains elusive [156, 157, 158, 159, 160, 161, 162]. An interesting experiment would be the simultaneous deposition of water at room temperature while shining in UV light using the laser system. Since we can operate our STM at different temperatures, it would be possible to do the deposition inside the chamber while scanning the anatase (101) surface. Due to the difference in hydrophilicity, also the molecular adsorption depends on the light irradiation increasing or reducing the amount of adsorbed water. Moreover, using our identification techniques, we could identify the adsorbed species on the anatase surface. This would be an important step towards explaining superhydrophilicity.

Following up on the investigation of the single water molecule adsorption of the different reactive surface phases would be the first time investigation of PWS on TiO₂ anatase (101) using STM-IETS in combination with our laser setup. We have already started first experiments on shining in high energy photons in our tip-sample junction but we did not see any changes for the exposed water molecules. However since we gained more knowledge about the characterization of individual water and hydrogen molecules during this PhD work, we are able to distinguish the different species in a clear and fast manner. Furthermore, we still have room to improve the laser alignment and stability, since the laser deposits a large amount of energy heating up the junction. In the next experiments we will try to enhance stability by warming up the STM beforehand to a temperature where the cooling of the cryostat can compensate the energy deposited by the laser. Another idea to circumvent the challenge of stability in *in situ* experiments is to scan an area labeling the individual molecules by IETS. The next step would be to retract the tip, while shining in the UV-light for a certain time. Subsequently, the tip is approached in the same area and the molecules are characterized once more using STM and IETS.

Using these measurement ideas and individual water molecules, we could study how important photons are for the initial water splitting step, H₂O to OH+H. As we have shown in section 5.2 the dissociation barriers for water are very low allowing the initial splitting to occur due to the substrate at room temperature. Since we operate in the dark, no UV photons can be adsorbed by the anatase substrate to create charge-carriers. The interesting question is, in which way the photon contributes to the overall water splitting. Mainly following two concepts will need to be addressed and studied:

1. The first initial water dissociation step is solely due to the TiO₂ anatase (101) surface and only the following steps (OH+H to O+2H and the desorption of O₂/H₂ from the surface) need excited charge carriers which are created when the sample is illuminated by high energy photons.
2. The first initial water dissociation can be performed via the surface but also

through excited charge carriers. Hence, the substrate mediated dissociation is not rate-limiting.

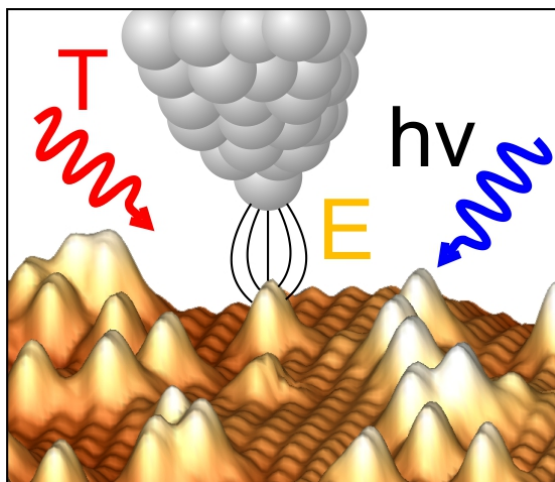


Figure 6.2: Different water splitting reactions which can be investigated by STM: Thermally-, electric field-, and photon-induced water splitting on TiO₂ anatase (101).

Both findings would have far reaching consequences. If the first hypothesis is valid, strategies modifying the surface activity, which would be the first rate-limiting step, become more important. The titanium-terminated surface phase might be a good candidate for this. In case of the second hypothesis for the initial step, water has the opportunity to dissociate via two channels. This could give more information where the actual rate-limitation in the H₂ production using TiO₂ anatase lies. For this also the study of tip-induced electric field dissociation would be interesting which has already been reported [67]. However, also in this study no chemical identification was given and when we were not yet able to repeat the experiments with the same settings. Nevertheless, these experiments also together with thermal-induced dissociation are interesting to further understand the dissociation process. In summary, further insight regarding the light-induced water splitting on TiO₂ anatase (101) could lead to a better understanding where the rate-limitations are creating possibilities to enhance device efficiencies.

6.2.3 Different Metal Oxides, Different Reactions

As already presented, the STM-IETS technique is not limited to investigate water splitting on TiO₂ anatase (101). The strategies presented here also hold true on different semiconductors and molecules. First, we look on the semiconductor side. In order to record an IETS signal having enough states around E_F is important. We achieve this by using a highly n-doped TiO₂ anatase (101) crystal. Hence, the following two criteria

have to be met to be able to detect the IETS signal:

- The semiconductor has to be sufficiently conductive to perform STM.
- Enough states have to be at the Fermi level. The doping should not be too high to prevent the transition of the semiconductor to a metal.

With this guideline a large range of semiconductors can be addressed especially metal oxides such as WO_3 or SrTiO_3 .

On the other hand, STM-IETS can be obtained from a large variety of molecules. A prominent example would be the reduction of CO_2 to CO . As ice, CO_2 exhibits a $\nu(\text{C}=\text{O})$ stretch mode around 291 meV and a $\delta(\text{O}=\text{C}=\text{O})$ bending mode around 82 meV. For CO the $\nu(\text{C}\equiv\text{O})$ stretch mode energy shifts to 265 meV and the bending mode disappears [163]. Depending on the surface the values shift slightly and additional vibrational modes might appear (*e.g.* rotational hindering in the case for CO on Cu as presented in section 5.1). The differences in the IETS data should be significant enough to label the individual molecules and perform a study similar to water splitting on TiO_2 anatase (101). Again the same questions about reaction mechanism and rate limitations can be asked for this case previewing the strong potential of this tool. In summary, using STM-IETS for different molecules on different semiconductors has the chance to increase fundamental understanding of reaction mechanisms potentially enhancing future catalytic device efficiencies.

Bibliography

- [1] Kamat, P. V. Meeting the Clean Energy Demand: Nanostructure Architectures for Solar Energy Conversion. *J. Phys. Chem. C* **111**, 2834–2860 (2007).
- [2] Stocker, T. *et al.* Climate Change 2013: The Physical Science Basis. Contribution of Working Group I to the Fifth Assessment Report of the Intergovernmental Panel on Climate Change, p.5. *Cambridge University Press, Cambridge, United Kingdom and New York, NY, USA, 1535 pp.* (2013).
- [3] Chapin, D. M., Fuller, C. S. & Pearson, G. L. A New Silicon p-n Junction Photocell for Converting Solar Radiation into Electrical Power. *J. Appl. Phys.* **25**, 676–677 (1954).
- [4] O'Regan, B. & Gratzel, M. A low-cost, high-efficiency solar cell based on dye-sensitized colloidal TiO₂ films. *Nature* **353**, 737–740 (1991).
- [5] Fujishima, A. & Honda, K. Electrochemical Photolysis of Water at a Semiconductor Electrode. *Nature* **238**, 37–38 (1972).
- [6] Burschka, J. *et al.* Sequential deposition as a route to high-performance perovskite-sensitized solar cells. *Nature* **499**, 316–319 (2013).
- [7] Im, J.-H., Lee, C.-R., Lee, J.-W., Park, S.-W. & Park, N.-G. 6.5% efficient perovskite quantum-dot-sensitized solar cell. *Nanoscale* **3**, 4088–4093 (2011).
- [8] Kojima, A., Teshima, K., Shirai, Y. & Miyasaka, T. Organometal Halide Perovskites as Visible-Light Sensitizers for Photovoltaic Cells. *J. Am. Chem. Soc.* **131**, 6050–6051 (2009).
- [9] Green, M. A., Emery, K., Hishikawa, Y., Warta, W. & Dunlop, E. D. Solar cell efficiency tables (Version 45). *Prog Photovoltaics* **23**, 1–9 (2015).
- [10] Fye, D. Oxford Photovoltaic, LOPEC Event 2015 (06.11.2015). URL <https://www.plusplasticelectronics.com/energy/>

Bibliography

- perovskite-solar-cells-coming-to-market-in-2017,-s.
- [11] Sivula, K. Toward Economically Feasible Direct Solar-to-Fuel Energy Conversion. *J. Phys. Chem. Lett.* **6**, 975–976 (2015).
- [12] Fujishima, A., Zhang, X. & Tryk, D. A. TiO₂ photocatalysis and related surface phenomena. *Surf. Sci. Rep.* **63**, 515 – 582 (2008).
- [13] Diebold, U. The surface science of titanium dioxide. *Surf. Sci. Rep.* **48**, 53 – 229 (2003).
- [14] Binnig, G., Rohrer, H., Gerber, C. & Weibel, E. 7 x 7 Reconstruction on Si(111) Resolved in Real Space. *Phys. Rev. Lett.* **50**, 120–123 (1983).
- [15] Binnig, G., Rohrer, H., Gerber, C. & Weibel, E. Tunneling through a controllable vacuum gap. *Appl. Phys. Lett.* **40**, 178–180 (1982).
- [16] Binnig, G., Rohrer, H., Gerber, C. & Weibel, E. Surface Studies by Scanning Tunneling Microscopy. *Phys. Rev. Lett.* **49**, 57–61 (1982).
- [17] Gong, X.-Q., Selloni, A., Batzill, M. & Diebold, U. Steps on anatase TiO₂(101). *Nat. Mater.* **5**, 665–670 (2006).
- [18] Oviedo, J., Sánchez-de Armas, R., San Miguel, M. A. & Sanz, J. F. Methanol and Water Dissociation on TiO₂ (110): The Role of Surface Oxygen. *J. Phys. Chem. C* **112**, 17737–17740 (2008).
- [19] Patrick, C. E. & Giustino, F. Structure of a Water Monolayer on the Anatase TiO₂(101) Surface. *Phys. Rev. Applied* **2**, 014001– (2014).
- [20] Walle, L. E. *et al.* Mixed Dissociative and Molecular Water Adsorption on Anatase TiO₂(101). *J. Phys. Chem. C* **115**, 9545–9550 (2011).
- [21] Herman, G. S., Dohnálek, Z., Ruzycki, N. & Diebold, U. Experimental Investigation of the Interaction of Water and Methanol with Anatase TiO₂(101). *J. Phys. Chem. B* **107**, 2788–2795 (2003).
- [22] Ho, W. Single-molecule chemistry. *J. Chem. Phys.* **117**, 11033–11061 (2002).
- [23] Lee, H. & Ho, W. Single-bond formation and characterization with a scanning tunneling microscope. *Science* **286**, 1719–1722 (1999).
- [24] Stipe, B. C., Rezaei, M. A. & Ho, W. Single-Molecule Vibrational Spectroscopy and Microscopy. *Science* **280**, 1732–1735 (1998).

-
- [25] Gratzel, M. Photoelectrochemical cells. *Nature* **414**, 338–344 (2001).
- [26] Hebenstreit, W., Ruzycski, N., Herman, G. S., Gao, Y. & Diebold, U. Scanning tunneling microscopy investigation of the TiO₂ anatase (101) surface. *Phys. Rev. B* **62**, R16334–R16336 (2000).
- [27] Chen, C. J. *Introduction to scanning tunneling microscopy* (Oxford University Press, 2008).
- [28] Wood, R. W. A New Form of Cathode Discharge and the Production of X-Rays, together with Some Notes on Diffraction. Preliminary Communication. *Phys. Rev. (Series I)* **5**, 1–10 (1897).
- [29] Wentzel, G. Eine Verallgemeinerung der Quantenbedingungen für die Zwecke der Wellenmechanik. *Z. Phys.* **38**, 518–529 (1926).
- [30] Kramers, H. Wellenmechanik und halbzahlige Quantisierung. *Z. Phys.* **39**, 828–840 (1926).
- [31] Brillouin, L. La Mécanique Ondulatoire de Schrödinger une Method Générale de Resolution par Approximations Successives. *Comptes Rendus des Seances de l'Académie des Sciences* 24–26 (1926).
- [32] Bardeen, J. Tunnelling from a Many-Particle Point of View. *Phys. Rev. Lett.* **6**, 57–59 (1961).
- [33] Tersoff, J. & Hamann, D. R. Theory of the scanning tunneling microscope. *Phys. Rev. B* **31**, 805–813 (1985).
- [34] Lambe, J. & Jaklevic, R. C. Molecular Vibration Spectra by Inelastic Electron Tunneling. *Phys. Rev.* **165**, 821–832 (1968).
- [35] Nakamoto, K. *Infrared and Raman spectra of inorganic and coordination compounds* (Wiley Online Library, 2008).
- [36] Kroeger, R. M. & Hansma, P. K. A measurement of the sensitivity of inelastic electron tunneling spectroscopy. *Surf. Sci.* **67**, 362–366 (1977).
- [37] Hipps, K. W. & Mazur, U. *Handbook of vibrational spectroscopy*, vol. 1-5 (John Wiley & Sons, Chichester, 2002).
- [38] Binnig, G., Garcia, N. & Rohrer, H. Conductivity sensitivity of inelastic scanning tunneling microscopy. *Phys. Rev. B* **32**, 1336–1338 (1985).

Bibliography

- [39] Persson, B. & Demuth, J. Inelastic electron tunnelling from a metal tip. *Solid State Commun.* **57**, 769–772 (1986).
- [40] Persson, B. N. J. & Baratoff, A. Inelastic electron tunneling from a metal tip: The contribution from resonant processes. *Phys. Rev. Lett.* **59**, 339–342 (1987).
- [41] Chiang, C.-l., Xu, C., Han, Z. & Ho, W. Real-space imaging of molecular structure and chemical bonding by single-molecule inelastic tunneling probe. *Science* **344**, 885–888 (2014).
- [42] Shen, T.-C. *et al.* Atomic-scale desorption through electronic and vibrational excitation mechanisms. *Science* **268**, 1590–1592 (1995).
- [43] Persson, B. Inelastic vacuum tunneling. *Phys. Scr.* **38**, 282 (1988).
- [44] Lorente, N., Persson, M., Lauhon, L. J. & Ho, W. Symmetry Selection Rules for Vibrationally Inelastic Tunneling. *Phys. Rev. Lett.* **86**, 2593–2596 (2001).
- [45] Kley, C. S. *Atomic-Scale Characterization and Control of Metal-Organic Templates and Photosensitizers on Surfaces*. Ph.D. thesis, SB, Lausanne (2013).
- [46] Chen, W., Madhavan, V., Jamneala, T. & Crommie, M. F. Scanning Tunneling Microscopy Observation of an Electronic Superlattice at the Surface of Clean Gold. *Phys. Rev. Lett.* **80**, 1469–1472 (1998).
- [47] Wahl, P., Schneider, M. A., Diekhöner, L., Vogelgesang, R. & Kern, K. Quantum Coherence of Image-Potential States. *Phys. Rev. Lett.* **91**, 106802 (2003).
- [48] Dette, C. *et al.* TiO₂ Anatase with a Bandgap in the Visible Region. *Nano Lett.* **14**, 6533–6538 (2014).
- [49] Titanium Mineral Concentrates. *U.S. Geological Survey, Mineral Commodity Summaries* (2012).
- [50] Ceresana. Market Study: Titanium Dioxide (2012).
- [51] Haruta, M., Yamada, N., Kobayashi, T. & Iijima, S. Gold catalysts prepared by coprecipitation for low-temperature oxidation of hydrogen and of carbon monoxide. *J. Catal.* **115**, 301 – 309 (1989).
- [52] Haruta, M., Kobayashi, T., Sano, H. & Yamada, N. Novel Gold Catalysts for the Oxidation of Carbon Monoxide at a Temperature far Below 0 °C. *Chem. Lett.* **16**, 405–408 (1987).

- [53] Iizuka, Y. *et al.* Adsorption of CO on gold supported on TiO₂. *Catal. Today* **36**, 115 – 123 (1997).
- [54] Valden, M., Pak, S., Lai, X. & Goodman, D. Structure sensitivity of CO oxidation over model Au/TiO₂ catalysts. *Catal. Lett.* **56**, 7–10 (1998).
- [55] Valden, M., Lai, X. & Goodman, D. W. Onset of Catalytic Activity of Gold Clusters on Titania with the Appearance of Nonmetallic Properties. *Science* **281**, 1647–1650 (1998).
- [56] Kim, T. S. *et al.* Cryogenic CO Oxidation on TiO₂-Supported Gold Nanoclusters Precovered with Atomic Oxygen. *J. Am. Chem. Soc.* **125**, 2018–2019 (2003).
- [57] Lee, S., Fan, C., Wu, T., & Anderson, S. L. CO Oxidation on Au_n/TiO₂ Catalysts Produced by Size-Selected Cluster Deposition. *J. Am. Chem. Soc.* **126**, 5682–5683 (2004).
- [58] Subramanian, V., Wolf, E. E., & Kamat, P. V. Catalysis with TiO₂/Gold Nanocomposites. Effect of Metal Particle Size on the Fermi Level Equilibration. *J. Am. Chem. Soc.* **126**, 4943–4950 (2004).
- [59] Green, I. X., Tang, W., Neurock, M. & Yates, J. T. Spectroscopic Observation of Dual Catalytic Sites During Oxidation of CO on a Au/TiO₂ Catalyst. *Science* **333**, 736–739 (2011).
- [60] Wang, Y.-G., Yoon, Y., Glezakou, V.-A., Li, J. & Rousseau, R. The Role of Reducible Oxide-Metal Cluster Charge Transfer in Catalytic Processes: New Insights on the Catalytic Mechanism of CO Oxidation on Au/TiO₂ from ab Initio Molecular Dynamics. *J. Am. Chem. Soc.* **135**, 10673–10683 (2013).
- [61] Mills, A., Davies, R. H. & Worsley, D. Water purification by semiconductor photocatalysis. *Chem. Soc. Rev.* **22**, 417–425 (1993).
- [62] Fu, G., Vary, P. S. & Lin, C.-T. Anatase TiO₂ nanocomposites for antimicrobial coatings. *J. Phys. Chem. B* **109**, 8889–8898 (2005).
- [63] Maness, P.-C. *et al.* Bactericidal Activity of Photocatalytic TiO₂ Reaction: Toward an Understanding of Its Killing Mechanism. *Appl. Environ. Microbiol.* **65**, 4094–4098 (1999).
- [64] Paz, Y., Luo, Z., Rabenberg, L. & Heller, A. Photooxidative self-cleaning transparent titanium dioxide films on glass. *J. Mater. Res.* **10**, 2842–2848 (1995).

Bibliography

- [65] Yaghoubi, H., Taghavinia, N. & Alamdari, E. K. Self cleaning TiO₂ coating on polycarbonate: Surface treatment, photocatalytic and nanomechanical properties. *Surf. Coat. Technol.* **204**, 1562 – 1568 (2010).
- [66] Setvin, M. *et al.* Reaction of O₂ with Subsurface Oxygen Vacancies on TiO₂ Anatase (101). *Science* **341**, 988–991 (2013).
- [67] Setvin, M. *et al.* Charge Trapping at the Step Edges of TiO₂ Anatase (101). *Angew. Chem. Int. Ed.* **53**, 4714–4716 (2014).
- [68] Li, G., Li, L., Boerio-Goates, J. & Woodfield, B. F. High Purity Anatase TiO₂ Nanocrystals: Near Room-Temperature Synthesis, Grain Growth Kinetics, and Surface Hydration Chemistry. *J. Am. Chem. Soc.* **127**, 8659–8666 (2005).
- [69] Hanaor, D. A. & Sorrell, C. C. Review of the anatase to rutile phase transformation. *J. Mater. Sci.* **46**, 855–874 (2011).
- [70] Zhang, J., Xu, Q., Feng, Z., Li, M. & Li, C. Importance of the Relationship between Surface Phases and Photocatalytic Activity of TiO₂. *Angew. Chem. Int. Ed.* **47**, 1766–1769 (2008).
- [71] Luttrell, T. *et al.* Why is anatase a better photocatalyst than rutile? - Model studies on epitaxial TiO₂ films. *Sci. Rep.* **4**, 4043 (2014).
- [72] Xu, M. *et al.* Photocatalytic Activity of Bulk TiO₂ Anatase and Rutile Single Crystals Using Infrared Absorption Spectroscopy. *Phys. Rev. Lett.* **106**, 138302 (2011).
- [73] Scanlon, D. O. *et al.* Band alignment of rutile and anatase TiO₂. *Nat. Mater.* **12**, 798–801 (2013).
- [74] He, Y., Dulub, O., Cheng, H., Selloni, A. & Diebold, U. Evidence for the Predominance of Subsurface Defects on Reduced Anatase TiO₂(101). *Phys. Rev. Lett.* **102**, 106105 (2009).
- [75] Kley, C. S. *et al.* Atomic-Scale Observation of Multiconformational Binding and Energy Level Alignment of Ruthenium-Based Photosensitizers on TiO₂ Anatase. *Nano Lett.* **14**, 563–569 (2014).
- [76] Feenstra, R. M. & Stroscio, J. A. Tunneling spectroscopy of the GaAs(110) surface. *J. Vac. Sci. Technol. B* **5**, 923–929 (1987).
- [77] Feenstra, R. M. Electrostatic potential for a hyperbolic probe tip near a semi-

- conductor. *J. Vac. Sci. Technol. B* **21**, 2080–2088 (2003).
- [78] Feenstra, R. M., Dong, Y., Semtsiv, M. P. & Masselink, W. T. Influence of tip-induced band bending on tunnelling spectra of semiconductor surfaces. *Nanotechnology* **18**, 044015 (2007).
- [79] Nowotny, J., Bak, T., Nowotny, M. & Sheppard, L. Titanium dioxide for solar-hydrogen II. Defect chemistry. *Int. J. Hydrogen Energy* **32**, 2630 – 2643 (2007).
- [80] Nowotny, J., Bak, T., Nowotny, M. & Sheppard, L. Titanium dioxide for solar-hydrogen IV. Collective and local factors in photoreactivity. *Int. J. Hydrogen Energy* **32**, 2651 – 2659 (2007).
- [81] Khan, M. M. *et al.* Band gap engineered TiO₂ nanoparticles for visible light induced photoelectrochemical and photocatalytic studies. *J. Mater. Chem. A* **2**, 637–644 (2014).
- [82] Jing, L. *et al.* Effects of Surface Oxygen Vacancies on Photophysical and Photochemical Processes of Zn-Doped TiO₂ Nanoparticles and Their Relationships. *J. Phys. Chem. B* **110**, 17860–17865 (2006).
- [83] Pan, X., Yang, M.-Q., Fu, X., Zhang, N. & Xu, Y.-J. Defective TiO₂ with oxygen vacancies: synthesis, properties and photocatalytic applications. *Nanoscale* **5**, 3601–3614 (2013).
- [84] Cheng, H. & Selloni, A. Surface and subsurface oxygen vacancies in anatase TiO₂ and differences with rutile. *Phys. Rev. B* **79**, 092101 (2009).
- [85] Scheiber, P. *et al.* (Sub)Surface Mobility of Oxygen Vacancies at the TiO₂ Anatase (101) Surface. *Phys. Rev. Lett.* **109**, 136103 (2012).
- [86] Setvin, M., Schmid, M. & Diebold, U. Aggregation and electronically induced migration of oxygen vacancies in TiO₂ anatase. *Phys. Rev. B* **91**, 195403 (2015).
- [87] Wendt, S. *et al.* The Role of Interstitial Sites in the Ti3d Defect State in the Band Gap of Titania. *Science* **320**, 1755–1759 (2008).
- [88] Papageorgiou, A. C. *et al.* Electron traps and their effect on the surface chemistry of TiO₂(110). *Proc. Natl. Acad. Sci. USA* **107**, 2391–2396 (2010).
- [89] Ganduglia-Pirovano, M. V., Hofmann, A. & Sauer, J. Oxygen vacancies in transition metal and rare earth oxides: Current state of understanding and remaining challenges. *Surf. Sci. Rep.* **62**, 219 – 270 (2007).

Bibliography

- [90] Di Valentin, C., Pacchioni, G. & Selloni, A. Electronic Structure of Defect States in Hydroxylated and Reduced Rutile TiO₂(110) Surfaces. *Phys. Rev. Lett.* **97**, 166803 (2006).
- [91] Krischok, S., Günster, J., Goodman, D., Höfft, O. & Kempster, V. MIES and UPS(HeI) studies on reduced TiO₂(110). *Surf. Interface Anal.* **37**, 77–82 (2005).
- [92] Mattioli, G., Filippone, F., Alippi, P. & Amore Bonapasta, A. *Ab initio* study of the electronic states induced by oxygen vacancies in rutile and anatase TiO₂. *Phys. Rev. B* **78**, 241201 (2008).
- [93] Morgan, B. J. & Watson, G. W. A DFT + U description of oxygen vacancies at the TiO₂ rutile (110) surface. *Surf. Sci.* **601**, 5034 – 5041 (2007).
- [94] Cheng, H. & Selloni, A. Energetics and diffusion of intrinsic surface and subsurface defects on anatase TiO₂(101). *J. Chem. Phys.* **131** (2009).
- [95] van Schilfhaarde, M., Kotani, T. & Faleev, S. Quasiparticle Self-Consistent GW Theory. *Phys. Rev. Lett.* **96**, 226402 (2006).
- [96] Valentin, C. D., Pacchioni, G. & Selloni, A. Reduced and n-Type Doped TiO₂: Nature of Ti³⁺ Species. *J. Phys. Chem. Lett.* **113**, 20543–20552 (2009).
- [97] Dette, C. *et al.* Reducing the Reactivity of the TiO₂ Anatase (101) Surface via Formation of an Oxygen Network. *in Preparation* (2016).
- [98] Setvin, M. *et al.* Identification of adsorbed molecules via STM tip manipulation: CO, H₂O, and O₂ on TiO₂ anatase (101). *Phys. Chem. Chem. Phys.* **16**, 21524–21530 (2014).
- [99] Asahi, R., Morikawa, T., Ohwaki, T., Aoki, K. & Taga, Y. Visible-Light Photocatalysis in Nitrogen-Doped Titanium Oxides. *Science* **293**, 269–271 (2001).
- [100] Choi, W., Termin, A. & Hoffmann, M. R. The Role of Metal Ion Dopants in Quantum-Sized TiO₂: Correlation between Photoreactivity and Charge Carrier Recombination Dynamics. *J. Phys. Chem.* **98**, 13669–13679 (1994).
- [101] Ohsawa, T. *et al.* Crystallographic dependence of visible-light photoactivity in epitaxial TiO_{2-x}N_x anatase and rutile. *Phys. Rev. B* **79**, 085401 (2009).
- [102] Valentin, C. D., Diebold, U. & Selloni, A. Doping and functionalization of photoactive semiconducting metal oxides. *Chem. Phys.* **339**, vii – viii (2007).
- [103] Diwald, O., Thompson, T. L., Goralski, E. G., Walck, S. D. & Yates Jr., J. T. The

- Effect of Nitrogen Ion Implantation on the Photoactivity of TiO₂ Rutile Single Crystals. *J. Phys. Chem. B* **108**, 52–57 (2004).
- [104] Robel, I., Subramanian, V., Kuno, M. & Kamat, P. V. Quantum Dot Solar Cells. Harvesting Light Energy with CdSe Nanocrystals Molecularly Linked to Mesoscopic TiO₂ Films. *J. Am. Chem. Soc.* **128**, 2385–2393 (2006).
- [105] Ariga, H. *et al.* Surface-Mediated Visible-Light Photo-oxidation on Pure TiO₂(001). *J. Am. Chem. Soc.* **131**, 14670–14672 (2009).
- [106] Tao, J., Luttrell, T. & Batzill, M. A two-dimensional phase of TiO₂ with a reduced bandgap. *Nat Chem* **3**, 296–300 (2011).
- [107] Patrick, C. E. & Giustino, F. GW quasiparticle bandgaps of anatase TiO₂ starting from DFT+U. *J. Phys.: Condens. Matter* **24**, 202201 (2012).
- [108] Liang, Z., Kim, H., Kim, Y. & Trenary, M. Molecular Oxygen Network as a Template for Adsorption of Ammonia on Pt(111). *J. Phys. Chem. Lett.* **4**, 2900–2905 (2013).
- [109] Dette, C. *et al.* Atomic Scale Investigation of a Pure H₂O Monolayer on TiO₂ Anatase (101). *in Preparation* (2016).
- [110] Dette, C. *et al.* Tracing H₂O splitting on Anatase TiO₂ (101) by Single-Molecule Vibrational Spectroscopy. *submitted* (2016).
- [111] Lauhon, L. J. & Ho, W. Single-molecule vibrational spectroscopy and microscopy: CO on Cu(001) and Cu(110). *Phys. Rev. B* **60**, R8525–R8528 (1999).
- [112] Blyholder, G. Molecular Orbital View of Chemisorbed Carbon Monoxide. *The Journal of Physical Chemistry* **68**, 2772–2777 (1964).
- [113] Dewar, M. J. S. A review of π -complex theory. *Bull. Soc. Chim. Fr.* **18** (1951).
- [114] Chatt, J. & Duncanson, L. A. Olefin co-ordination compounds. Part III. Infra-red spectra and structure: attempted preparation of acetylene complexes. *J. Chem. Soc.* 2939–2947 (1953).
- [115] Hofmann, P. *et al.* A photoelectron diffraction study of the structure of the Cu(110)(2 \times 1)-CO system. *Surf. Sci.* **337**, 169 – 176 (1995).
- [116] McConville, C. *et al.* An X-ray absorption and photoelectron diffraction study of the Cu(100) c(2 \times 2) CO structure. *Surf. Sci.* **166**, 221 – 233 (1986).

Bibliography

- [117] Tracy, J. C. Structural Influences on Adsorption Energy III. CO on Cu(100). *J. Chem. Phys.* **56**, 2748–2754 (1972).
- [118] Andersson, S. Vibrational excitations and structure of CO chemisorbed on Cu(100). *Surf. Sci.* **89**, 477 – 485 (1979).
- [119] Andersson, S. & Pendry, J. B. Structure of CO Adsorbed on Cu(100) and Ni(100). *Phys. Rev. Lett.* **43**, 363–366 (1979).
- [120] Uvdal, P., Karlsson, P.-A., Nyberg, C., Andersson, S. & Richardson, N. On the structure of dense CO overlayers. *Surf. Sci.* **202**, 167 – 182 (1988).
- [121] Pritchard, J. On the structure of CO adlayers on Cu(100) and Cu(111). *Surf. Sci.* **79**, 231–244 (1979).
- [122] Ryberg, R. Carbon monoxide adsorbed on Cu(100) Studied by infrared spectroscopy. *Surf. Sci.* **114**, 627–641 (1982).
- [123] Biberian, J. & Van Hove, M. A new model for CO ordering at high coverages on low index metal surfaces: A correlation between LEED, HREELS and IRS: I. CO adsorbed on fcc (100) surfaces. *Surf. Sci.* **118**, 443–464 (1982).
- [124] Thamankar, R. *et al.* Tilting, Bending, and Nonterminal Sites in CO/Cu(001). *Phys. Rev. Lett.* **106**, 106101 (2011).
- [125] Hirschmugl, C. J., Williams, G. P., Hoffmann, F. M. & Chabal, Y. J. Adsorbate-substrate resonant interactions observed for CO on Cu(100) in the far infrared. *Phys. Rev. Lett.* **65**, 480–483 (1990).
- [126] He, Y., Tilocca, A., Dulub, O., Selloni, A. & Diebold, U. Local ordering and electronic signatures of submonolayer water on anatase TiO₂(101). *Nat. Mater.* **8**, 585–589 (2009).
- [127] Stetsovych, O. *et al.* Atomic species identification at the (101) anatase surface by simultaneous scanning tunnelling and atomic force microscopy. *Nat Commun* **6**, 7265 (2015).
- [128] Setvín, M. *et al.* Erratum for the Report “Reaction of O₂ with subsurface oxygen vacancies on TiO₂ anatase (101)”. *Science* **349**, aac9659 (2015).
- [129] Wahl, P., Diekhöner, L., Schneider, M. A. & Kern, K. Background removal in scanning tunneling spectroscopy of single atoms and molecules on metal surfaces. *Rev. Sci. Instrum.* **79** (2008).

- [130] Belhadj, H., Hakki, A., Robertson, P. K. J. & Bahnemann, D. W. In situ ATR-FTIR study of H₂O and D₂O adsorption on TiO₂ under UV irradiation. *Phys. Chem. Chem. Phys.* **17**, 22940–22946 (2015).
- [131] Lindan, P., Harrison, N., Holender, J. & Gillan, M. First-principles molecular dynamics simulation of water dissociation on TiO₂ (110). *Chem. Phys. Lett.* **261**, 246 – 252 (1996).
- [132] Lindan, P. J. D., Harrison, N. M. & Gillan, M. J. Mixed Dissociative and Molecular Adsorption of Water on the Rutile (110) Surface. *Phys. Rev. Lett.* **80**, 762–765 (1998).
- [133] Stefanovich, E. V. & Truong, T. N. Ab initio study of water adsorption on TiO₂(110): molecular adsorption versus dissociative chemisorption. *Chem. Phys. Lett.* **299**, 623–629 (1999).
- [134] Zhang, C. & Lindan, P. J. Multilayer water adsorption on rutile TiO₂ (110): A first-principles study. *J. Chem. Phys.* **118**, 4620–4630 (2003).
- [135] Lindan, P. J. D. & Zhang, C. Exothermic water dissociation on the rutile TiO₂(110) surface. *Phys. Rev. B* **72**, 075439 (2005).
- [136] Harris, L. A. & Quong, A. A. Molecular Chemisorption as the Theoretically Preferred Pathway for Water Adsorption on Ideal Rutile TiO₂(110). *Phys. Rev. Lett.* **93**, 086105 (2004).
- [137] Lindan, P. J. D. & Zhang, C. Comment on “Molecular Chemisorption as the Theoretically Preferred Pathway for Water Adsorption on Ideal Rutile TiO₂(110)”. *Phys. Rev. Lett.* **95**, 029601 (2005).
- [138] Harris, L. A. & Quong, A. A. Reply to Lindan and Zhang:. *Phys. Rev. Lett.* **95**, 029602 (2005).
- [139] Perron, H. *et al.* Combined investigation of water sorption on TiO₂ rutile (110) single crystal face: XPS vs. periodic DFT. *Surf. Sci.* **601**, 518 – 527 (2007).
- [140] Zhang, W., Yang, J., Luo, Y., Monti, S. & Carravetta, V. Quantum molecular dynamics study of water on TiO₂(110) surface. *J. Chem. Phys.* **129**, 064703 (2008).
- [141] Kowalski, P. M., Meyer, B. & Marx, D. Composition, structure, and stability of the rutile TiO₂(110) surface: Oxygen depletion, hydroxylation, hydrogen migration, and water adsorption. *Phys. Rev. B* **79**, 115410 (2009).

Bibliography

- [142] Walle, L. E., Borg, A., Uvdal, P. & Sandell, A. Experimental evidence for mixed dissociative and molecular adsorption of water on a rutile TiO₂(110) surface without oxygen vacancies. *Phys. Rev. B* **80**, 235436 (2009).
- [143] Vittadini, A., Selloni, A., Rotzinger, F. P. & Grätzel, M. Structure and Energetics of Water Adsorbed at TiO₂ Anatase (101) and (001) Surfaces. *Phys. Rev. Lett.* **81**, 2954–2957 (1998).
- [144] Tilocca, A., & Selloni, A. Vertical and Lateral Order in Adsorbed Water Layers on Anatase TiO₂(101). *Langmuir* **20**, 8379–8384 (2004).
- [145] Beck, D. D., White, J. M. & Ratcliffe, C. T. Catalytic reduction of carbon monoxide with hydrogen sulfide. 2. Adsorption of water and hydrogen sulfide on anatase and rutile. *J. Phys. Chem.* **90**, 3123–3131 (1986).
- [146] Hugenschmidt, M. B., Gamble, L. & Campbell, C. T. The interaction of H₂O with a TiO₂(110) surface. *Surf. Sci.* **302**, 329–340 (1994).
- [147] Acharya, D., Ciobanu, C., Camillone III, N. & Sutter, P. Mechanism of electron-induced hydrogen desorption from hydroxylated rutile TiO₂ (110). *J. Phys. Chem. Lett.* **114**, 21510–21515 (2010).
- [148] Chatten, R., Chadwick, A. V., Rougier, A. & Lindan, P. J. D. The Oxygen Vacancy in Crystal Phases of WO₃. *J. Phys. Chem. B* **109**, 3146–3156 (2005).
- [149] Gillet, M., Lemire, C., Gillet, E. & Aguir, K. The role of surface oxygen vacancies upon WO₃ conductivity. *Surf. Sci.* **532–535**, 519–525 (2003).
- [150] Choi, M., Oba, F., Kumagai, Y. & Tanaka, I. Anti-ferrodistortive-Like Oxygen-Octahedron Rotation Induced by the Oxygen Vacancy in Cubic SrTiO₃. *Adv. Mater.* **25**, 86–90 (2013).
- [151] Shepherd, J. *Geoengineering the Climate: Science, Governance and Uncertainty*. *The Royal Society* (2009).
- [152] Pope, F. D. *et al.* Stratospheric aerosol particles and solar-radiation management. *Nature Clim. Change* **2**, 713–719 (2012).
- [153] Tang, M. J. *et al.* Heterogeneous reaction of N₂O₅ with airborne TiO₂ particles and its implication for stratospheric particle injection. *Atmos. Chem. Phys.* **14**, 6035–6048 (2014).
- [154] Bikondoa, O. *et al.* Direct visualization of defect-mediated dissociation of water

- on TiO₂(110). *Nat. Mater.* **5**, 189–192 (2006).
- [155] Wang, R. *et al.* Light-induced amphiphilic surfaces. *Nature* **388**, 431–432 (1997).
- [156] Emeline, A. V., Rudakova, A. V., Sakai, M., Murakami, T. & Fujishima, A. Factors Affecting UV-Induced Superhydrophilic Conversion of a TiO₂ Surface. *J. Phys. Chem. C* **117**, 12086–12092 (2013).
- [157] White, J. M., Szanyi, J. & Henderson, M. A. The Photon-Driven Hydrophilicity of Titania: A Model Study Using TiO₂(110) and Adsorbed Trimethyl Acetate. *J. Phys. Chem. B* **107**, 9029–9033 (2003).
- [158] Mezhenny, S. *et al.* STM studies of defect production on the TiO₂(110)-(1×1) and TiO₂(110)-(1×2) surfaces induced by UV irradiation. *Chem. Phys. Lett.* **369**, 152–158 (2003).
- [159] Miyauchi, M., Nakajima, A., Fujishima, A., Hashimoto, K. & Watanabe, T. Photoinduced Surface Reactions on TiO₂ and SrTiO₃ Films: Photocatalytic Oxidation and Photoinduced Hydrophilicity. *Chem. Mater.* **12**, 3–5 (2000).
- [160] Miyauchi, M., Nakajima, A., Watanabe, T. & Hashimoto, K. Photocatalysis and Photoinduced Hydrophilicity of Various Metal Oxide Thin Films. *Chem. Mater.* **14**, 2812–2816 (2002).
- [161] Takeuchi, M., Sakamoto, K., Martra, G., Coluccia, S. & Anpo, M. Mechanism of Photoinduced Superhydrophilicity on the TiO₂ Photocatalyst Surface. *J. Phys. Chem. B* **109**, 15422–15428 (2005).
- [162] Sakai, N., Fujishima, A., Watanabe, T. & Hashimoto, K. Enhancement of the Photoinduced Hydrophilic Conversion Rate of TiO₂ Film Electrode Surfaces by Anodic Polarization. *J. Phys. Chem. B* **105**, 3023–3026 (2001).
- [163] Gerakines, P., Schutte, W., Greenberg, J. & van Dishoeck, E. F. The infrared band strengths of H₂O, CO and CO₂ in laboratory simulations of astrophysical ice mixtures. *arXiv* (1994).

Personal Information

Name Christian Dette
Date of Birth January 11, 1989
Place of Birth Reutlingen, Germany
Nationality German

Education

Apr. 2012 – present
Doctoral Studies in Physics
Ecole Polytechnique Fédérale de Lausanne, Switzerland
Thesis: *Atomic Scale Observation of Chemical and Electronic Properties of Metal-Oxide Surfaces*
Anticipated degree date: Summer 2016
Group: Prof. Klaus Kern at Max Planck Institute Stuttgart, Germany.

Sep. 2010 – Apr. 2012
Master Studies in Physics
Ecole Polytechnique Fédérale de Lausanne, Switzerland
External thesis project: *Scanning Tunneling Microscope induced Luminescence on fac-Ir(ppy)₃ on C₆₀/Ag(111)*
Group: Prof. Klaus Kern at Max Planck Institute Stuttgart, Germany.

Oct. 2007 – Sep. 2010
Bachelor Studies in Physics
University of Konstanz, Germany
External thesis project: *Spin Dependent Transport in Graphene using EuS as a Spin Filter*
Group: Dr. Jagadeesh Moodera at Massachusetts Institute of Technology, USA.

Sep. 1998 – June 2007
High School
Friedrich-List-Gymnasium Reutlingen, Germany.

Publications

- #1 **C. Dette**, M.A. Perez-Osorio, S. Mangel, F. Giustino, S.J. Jung, and K. Kern, *Reducing the Reactivity of the TiO₂ Anatase (101) Surface via Formation of an Oxygen Network*, in preparation (2016).
- #2 **C. Dette**, M.A. Perez-Osorio, S. Mangel, F. Giustino, S.J. Jung, and K. Kern, *Atomic Scale Investigation of a Pure H₂O Monolayer on TiO₂ Anatase (101)*, in preparation (2016).
- #3 **C. Dette**, M.A. Perez-Osorio, S. Mangel, F. Giustino, S.J. Jung, and K. Kern, *Tracing H₂O splitting on Anatase TiO₂ (101) by Single-Molecule Vibrational Spectroscopy*, submitted (2016).
- #4 **C. Dette**, M.A. Perez-Osorio, C.S. Kley, P. Punke, C.E. Patrick, P. Jacobson et al. *TiO₂ Anatase with a Bandgap in the Visible Region*, Nano Letters 14 (11), 6533-6538 (2014).
- #5 C.S. Kley, **C. Dette**, G. Rinke, C.E. Patrick, J. Cechal, S.J. Jung et al. *Atomic-Scale Observation of Multiconformational Binding and Energy Level Alignment of Ruthenium-Based Photosensitizers on TiO₂ Anatase*, Nano Letters 14 (2), 563-569 (2014).
- #6 T. Lutz, C. Große, **C. Dette**, A. Kabakchiev, F. Schramm, M. Ruben et al. *Molecular Orbital Gates for Plasmon Excitation*, Nano Letters 13 (6), 2846-2850 (2013).
- #7 L. Heyne, J. Rhensius, Y.J. Cho, D. Bedau, S. Krzyk, **C. Dette** et al. *Geometry-Dependent Scaling of Critical Current Densities for Current-Induced Domain Wall Motion and Transformations*, Physical Review B 80 (18), 184405 (2009).